MAGNETOSPHERIC WAVE INJECTION BY MODULATED HF HEATING OF THE AURORAL ELECTROJET

A DISSERTATION
SUBMITTED TO THE DEPARTMENT OF ELECTRICAL ENGINEERING
AND THE COMMITTEE ON GRADUATE STUDIES
OF STANFORD UNIVERSITY
IN PARTIAL FULFILLMENT OF THE REQUIREMENTS
FOR THE DEGREE OF
DOCTOR OF PHILOSOPHY

Marek Gołkowski
March 2009

I certify that I have read this dissertation and that, in my opinion, it is fully adequate in scope and quality as a dissertation for the degree of Doctor of Philosophy.

(Umran S. Inan) Principal Adviser

I certify that I have read this dissertation and that, in my opinion, it is fully adequate in scope and quality as a dissertation for the degree of Doctor of Philosophy.

(Donald L. Carpenter)

I certify that I have read this dissertation and that, in my opinion, it is fully adequate in scope and quality as a dissertation for the degree of Doctor of Philosophy.

(Mark A. Kasevich)

Approved for the University Committee on Graduate Studies.

This thesis is dedicated to my grandparents.

Abstract

Modulated High Frequency (HF, 3−30 MHz) heating of the auroral electrojet to generate electromagnetic waves in the Extremely Low Frequency (ELF, 3−3000 Hz) and Very Low Frequency (VLF, 3−30 kHz) bands is investigated in the context of magnetospheric wave injection experiments. The ionospheric heating facility of the High Frequency Active Auroral Research Program (HAARP) is used to excite non-linear amplification of whistler mode waves in the Earth's magnetosphere. Experimental evidence is presented of the first HF heater generated signals experiencing 'ducted' inter-hemispheric propagation and wave-particle interactions resulting in amplification and triggering of free running emissions. The roles of transmitter parameters as well as natural background conditions of the observations are characterized. Dispersion of observed signals is used to determine the magnetospheric propagation paths and associated cold plasma densities. It is found that HAARP induced triggered emissions occur primarily inside the plasmapause and the availability and coupling into magnetospheric 'ducts' is likely one of the limiting factors for observations. Phase and amplitude changes in the observed signals are used to resolve the temporal behavior of the non-linear resonant current vector that drives amplification. The observed resonant current behavior is discussed in the context of numerical models and used to make inferences about the magnetospheric hot plasma distribution. Ground based capabilities of detection of energetic particle precipitation from the Earth's radiation belts induced by HAARP generated ELF/VLF waves are assessed experimentally and theoretically. A phenomenon of cross-modulation between whistler-mode signals and HF ionospheric heating is observed and investigated as a new method to generate ELF/VLF radiation using an HF ionospheric heater.

Acknowledgements

There are many individuals who have made this work possible and have aided me through my graduate student career. First and foremost, I would like to thank my adviser, Professor Umran Inan for his support, guidance, and scientific vision. I am honored to have been a member of Umran's research group and appreciate the many opportunities for scholarship, teaching, and adventure that this has involved. Second, I am grateful for my opportunities to interact with Professor Don Carpenter who has been a great source of advice on analyzing and interpreting data as well providing valuable perspective and historical context for my work.

Several students in the VLF group have been instrumental in my research efforts and intellectual development. I thank Morris Cohen for many years of successful collaboration in deployment of hardware, design of experiments, analysis of data, and publishing of results. My discussions with Andrew Gibby on triggered emission theory solidified key concepts and helped me make significant progress in my last year. Prajwal Kulkarni has served as a mentor, co-instructor, tennis partner, mutual soccer enthusiast, and above all a friend always willing to lend an ear in matters of science and life. I am grateful to Ryan Said for many fruitful discussions particularly on the nuances of signal processing. Ben Cotts has always been a trusted source of solidarity and support. Robb Moore introduced me to the world of HAARP wave injection experiments; Joe Payne will always be an example of dedication and persistence in engineering and field work. I commend Noah Reddell, Max Klein, and Jeffrey Chang for their efforts in the realization of the Buoy receivers which provided me with valuable observations. I thank Denys Piddyachiy, George Jin and others for many hours of monitoring the HAARP experiments and helping me obtain important

results.

Shaolan Min and Helen Niu are responsible for the VLF group being not only an efficient research enterprise but also an organization founded on camaraderie and friendship. Data collection from the HAARP experiment has been greatly aided by the work and organizational skills of Dan Musetescu. My research also would not have been possible without the cooperation and commitment of the receiver hosts in Alaska and the operators of the HAARP facility. Special thanks to Norma and Doyle Traw, Mike McCarrick, Helio Zwi, and David Seafolk-Kopp.

Finally, I would like to thank my family and my wife Patrycja for the love and support that has guided me to this accomplishment.

Marek Andrzej Gołkowski

Stanford, California
December 2008

Contents

Abstract **v**

Acknowledgements **vi**

1 Introduction **1**

1.1 The Ionosphere 2

1.2 The Magnetosphere 4

1.3 Whistler Mode Wave Injection Experiments 9

1.3.1 Early Experiments and Observations 10

1.3.2 Siple Station 11

1.3.3 HF Ionospheric Heating 12

1.3.4 The HAARP Facility 16

1.4 Thesis Organization 17

1.5 Scientific Contributions 18

2 Experiment Setup and Observations **20**

2.1 Experiment Setup 20

2.1.1 Northern Hemisphere 20

2.1.2 Southern Hemisphere 21

2.1.3 Spacecraft Observations 24

2.1.4 Transmission Formats and Operation 24

2.2 Observations 25

2.2.1 First Observations: 20 April 2004 26

2.2.2 Full Power HAARP 26

2.3 Summary of Observations 37

3 Occurrence Statistics and Dependencies 39

3.1 HAARP ELF/VLF Generation Strength 40

3.2 Determination of Magnetospheric Path 44

3.3 Modulation Technique and Beam Geometry 51

3.4 Comparison with Siple Station Results 55

3.5 Summary 59

4 Theory and Observations 61

4.1 Theoretical Background 62

4.1.1 Cyclotron Resonance 62

4.1.2 Single Particle Dynamics 64

4.1.3 Resonant Currents 67

4.1.4 Non-linear Amplification Mechanism 69

4.2 Observations in Theoretical Context 72

4.2.1 Resonance and Trapping Conditions 73

4.2.2 Characterization of Non-linear Resonant Current 74

5 Cross Modulation 82

5.1 Observation 82

5.2 Theoretical Modeling 83

5.3 Cross Modulation for Generation 86

6 HAARP Induced Electron Precipitation 91

6.1 Experiment Setup 92

6.2 Theoretical Predictions 95

6.3 Effect of HF Heating 98

6.4 Mitigation of HF Heating 100

6.5 Ionospheric Effect of ELF/VLF Modulation Frequency 102

6.6 Summary and Future Work 103

7 Summary and Suggestions for Future Work **105**

7.1 Summary of Contributions 105

7.2 Suggestions for Future Work 107

A Derivation of the Wave Update **108**

List of Tables

2.1 Summary of Observation Occurrence 38

3.1 Parameters of Diffusive Equilibrium Models 47

List of Figures

1.1 Typical Ionospheric Profiles 3
1.2 The Outer Magnetosphere 5
1.3 The Inner Magnetosphere 6
1.4 Whistler Mode Propagation in the Magnetosphere 9
1.5 Magnetospheric Echoes from Siple Station Experiment 13
1.6 HAARP Wave Injection Experiment 18

2.1 Experiment Hardware and Locations 22
2.2 First Observations 25
2.3 27 February 2007 Observations 27
2.4 4 March 2007 Observations 28
2.5 Non-linear Amplification 29
2.6 Active Frequency Range 30
2.7 Strong 2-Hop Echoes 31
2.8 One-hop Echoes on DEMETER 32
2.9 One-hop Echoes on Buoy 2.0 34
2.10 Two-hop Echoes from Ramps Only 35
2.11 One-hop Echoes on Tangaroa 36

3.1 HAARP Signal Amplitudes Yielding Echoes 42
3.2 Echo Amplitude vs. Time I 43
3.3 Echo Amplitude vs. Time II 44
3.4 Magnetospheric Path Determination 48
3.5 Equatorial Density Profiles 50

3.6 Echoes Excited by Geometric Modulation 52
3.7 Scatter Plot for Different Modulation Techniques 53
3.8 Investigation of HF Beam Position 55
3.9 Spatial Effects of HF Beam Position 56
3.10 Siple Station Statistics 57

4.1 Cyclotron Resonance 63
4.2 Coordinate System for Single Particle Dynamics 64
4.3 Resonant Current Formation 65
4.4 Resonant Current Configuration 67
4.5 Non-linear Amplification Dynamics 70
4.6 Trapping Amplitude and Resonant Energies 74
4.7 Tracking of Non-linear Current Vector 76
4.8 Different Input Amplitudes 77
4.9 Different Input Amplitudes 78
4.10 Same Input Amplitudes 79

5.1 Echo Heating Cross Modulation 83
5.2 Effect of Modulated HF Heating on Ionospheric Medium 85
5.3 Spectral Analysis of Cross Modulation 87
5.4 Cross Modulation Generation Concept 88
5.5 Generation Using Cross Modulation 89
5.6 Frequency Response of Cross Modulation Based Generation 90

6.1 VLF Remote Sensing 94
6.2 VLF Transmitter Paths 95
6.3 Predicted Non-ducted Precipitation 97
6.4 Scale of HF Heated Region 99
6.5 Effect of HF Heating on VLF Remote Sensing 101
6.6 Mitigation of HF Heating Effect 102
6.7 Effect of ELF/VLF Frequency 104

Chapter 1

Introduction

It is only within the last 75 years that a comprehensive description of the immediate environment surrounding our planet has been achieved. For hundreds of years scientists were more versed in the orbits of distant planets and stars than in the nature of matter a few hundred kilometers above the Earth's surface. It was arguably the discovery of electromagnetic waves and the dawn of the Space Age that finally provided the tools to explore the surroundings of our planet. Most generally, the near-Earth space environment can be divided into two over-arching regions known as the magnetosphere and the ionosphere. Although at the time of this writing the basic structures and boundaries of the magnetosphere and ionosphere have been successfully mapped, the spatial and temporal variations, dynamics, and coupling of the physical processes in these regions continue to be the subjects of active experimental and theoretical research. The topic of this dissertation is the assessment and analysis of results of a pioneering experiment involving probing the Earth's magnetosphere with Extremely Low Frequency (ELF) and Very Low Frequency (VLF) electromagnetic waves generated via High Frequency (HF) heating of the auroral ionosphere. In this chapter we present a brief background and motivation for the topic and describe the specific contributions of the present work.

1.1 The Ionosphere

Although the dominant states of matter on the Earth's surface are the familiar solid, liquid, or gas, the surrounding space environment is distinguished by the presence of varying densities of ionized gases, also known as plasma or the fourth state of matter. Plasma densities become appreciable at altitudes of about 50 km, where photoionization caused by solar radiation generates significant densities of free electrons and ions to affect the propagation of radio waves. This altitude marks the approximate lower boundary of the ionosphere, the region of the atmosphere that is electrically charged [*Ratcliffe*, 1959; *Tascione*, 1994, Sec. 7.0]. The vertical structure of the ionosphere shows considerable variation as a function of the time of day, latitude, season, and solar activity. However, the essential features of the ionosphere can usually be identified and manifest themselves as horizontal layers organized by altitude and electron density. Distinct ionospheric layers develop because the deposition of solar energy and physics of recombination depend on the atmospheric density and composition, which both vary predictably with altitude. Figure 1.1 shows the typical ionospheric nighttime and daytime profiles with identified layers D, E, F1, F2 [*Tascione*, 1994, Sec. 7.1]. At nighttime the overall electron density decreases since photoionization ceases, but drainage form the overlying region and cosmic rays ensure that the ionospheric plasma persists through the night. In addition to the identifiable ionospheric layers, the ionosphere is known to regularly host transient and laterally inhomogeneous structures. These variations include dense slabs of ionization on scales of tens to hundreds of kilometers known as sporadic E or spread F depending on the altitude [*Calvert and Warnock*, 1969] and also much smaller, even meter scale, density irregularities [*Dyson*, 1969; *Clark and Raitt*, 1976; *Gross and Muldrew*, 1984; *Sonwalkar and Harikumar*, 2000].

The ionosphere is generally characterized as a collisional plasma. For altitudes below 200 km, in the D and E regions, collisions between electrons and neutral molecules are dominant with collision frequencies reaching $10^6 - 10^7$ Hz in the D-region. Above 200 km, in the F region, the collision frequency is typically 2 to 3 orders of magnitude lower and collisions are predominantly coulomb collisions between charged

species [*Helliwell*, 1965, Sec. 3.8]. Particles in the ionosphere have significant thermal motions, with temperatures about 200 K in the D region and 1000 K−2000 K in the F region. Nevertheless, in the context of electromagnetic wave propagation, the thermal motions can be neglected and the propagation of waves within and through the ionosphere can be accurately modeled assuming a 'cold' (0 K) plasma [*Budden*, 1988, p. 4-5].

Since the ionosphere contains free charges, it can support electrical currents and in fact many kilo-Amperes of current regularly flow around the Earth at ionospheric altitudes. Certain ionospheric currents are purely local or global but devoid of identifiable structure, such as those associated with the global electric circuit [*Rycroft et al.*, 2000]. However, two distinct global current structures exist, the auroral electrojet and the equatorial electrojet. The equatorial electrojet is driven by neutral winds and partly results from the unique geometry of a horizontal magnetic field found in the equatorial region [*Forbes*, 1981]. The so-called auroral electrojet, on the other hand, is driven by the electrodynamic coupling of magnetospheric plasma dynamics to the ionosphere via geomagnetic field lines [*Baumjohann*, 1983].

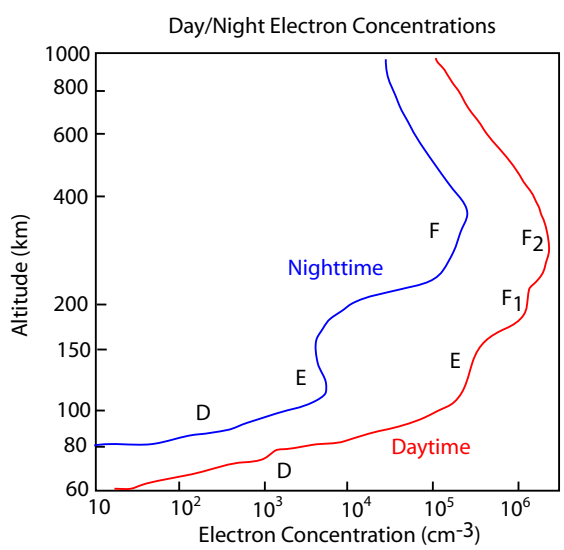

Figure 1.1: Typical daytime and nighttime electron density profiles in the ionosphere with identified layers. Adapted from [*Tascione*, 1994, p. 90].

1.2 The Magnetosphere

At altitudes of ∼2000 km the ionosphere gives way to what is known as the magnetosphere. Although the boundary between the neutral atmosphere and the ionosphere is abrupt, the higher altitude transition from the ionosphere to the magnetosphere does not have easily identifiable features and the definition of this boundary is largely a matter of convention. The magnetosphere is so named because the Earth's static magnetic field dominates the particle and wave dynamics. To first order, the geomagnetic field is that of a simple magnetic dipole, tilted and off-center relative to the rotation axis of the Earth. At distances greater than 5 Earth radii from the center of the Earth (1 Earth radius $R_{\mathrm{E}} \simeq$6370 km), the geomagnetic dipole geometry is significantly distorted by the solar wind, a hot plasma (10^5 K) composed mainly of protons and electrons traveling outward from the sun at speeds of ∼500 km/s. A bow shock is formed at $\sim 11R_{\mathrm{E}}$ with the solar wind dragging the geomagnetic field lines away from the sun, forming a large magnetotail. Thus, as is shown in Figure 1.2, the magnetosphere extends to about $10-12R_{\mathrm{E}}$ toward the sun and about $100R_{\mathrm{E}}$ away from the sun. In this research we are primarily concerned with regions of the magnetosphere with 'closed' magnetic field lines, meaning lines of force that begin and end at the Earth's surface and are not grossly distorted from the dipole geometry. This region extends to about $6-7R_{\mathrm{E}}$ and is known as the inner magnetosphere, shown schematically in Figure 1.3.

The magnetosphere is entirely filled with plasma that is fully ionized and can be regarded as collisionless. The magnetospheric plasma is usually divided into two distinct populations. The background 'cold' plasma has low energies typically ∼0.5 eV (∼5000 K), and densities in the range of $10-1000$ cm^{-3}. One characteristic of this cold plasma distribution is a sharp drop in density from 1 to 2 orders of magnitude at a boundary known as the plasmapause [*Carpenter*, 1963]. The region of the inner magnetosphere within the plasmapause is known as the plasmasphere. The location of the plasmapause varies from $\sim 2R_{\mathrm{E}}$ to $7R_{\mathrm{E}}$ and is believed to be determined by the balance of the electric field arising from the Earth's rotation in its own magnetic field (co-rotation field) and the cross-tail electric field in the outer magnetosphere which

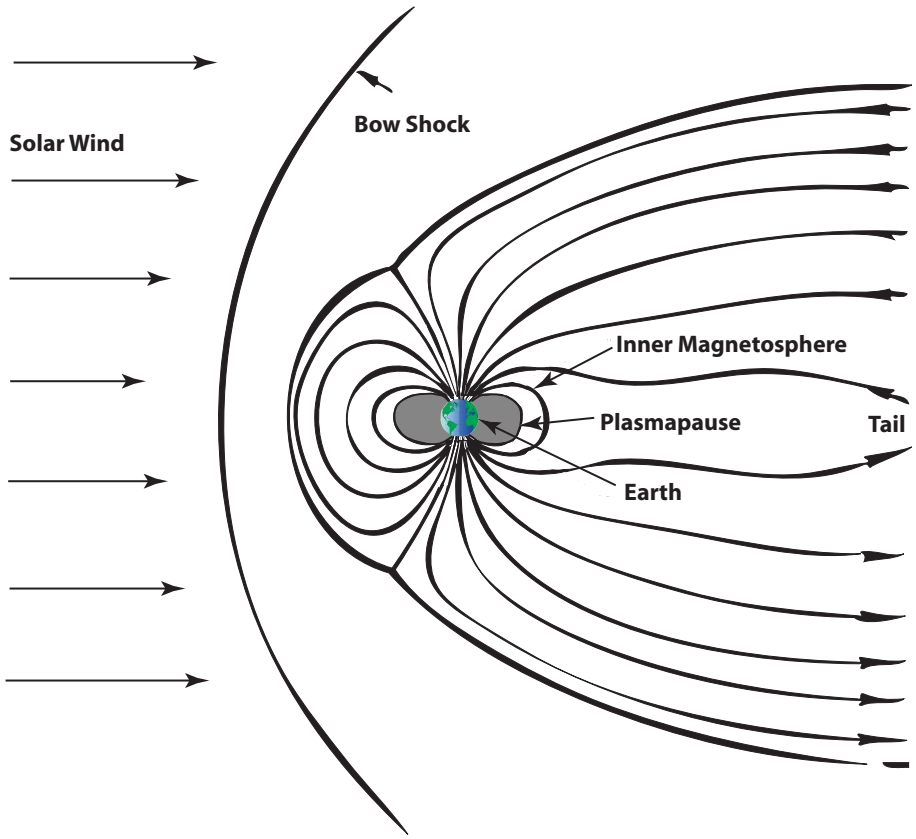

Figure 1.2: The general outline of the magnetosphere. Adapted from [*Inan*, 1977].

is driven by the solar wind [*Tascione*, 1994, Sec. 5.6]. The effects of these fields and their associated currents, as well as other magnetospheric processes, are observable in ground measurements of variations of the geomagnetic field. The level of activity in these measurements is often generally referred to as the geomagnetic conditions. Disturbed conditions correspond to an erosion of the plasmasphere, while under quiet conditions the plasmasphere expands radially outward as depleted regions are refilled from the dense underlying ionosphere.

In addition to the background cold plasma, the magnetosphere contains small

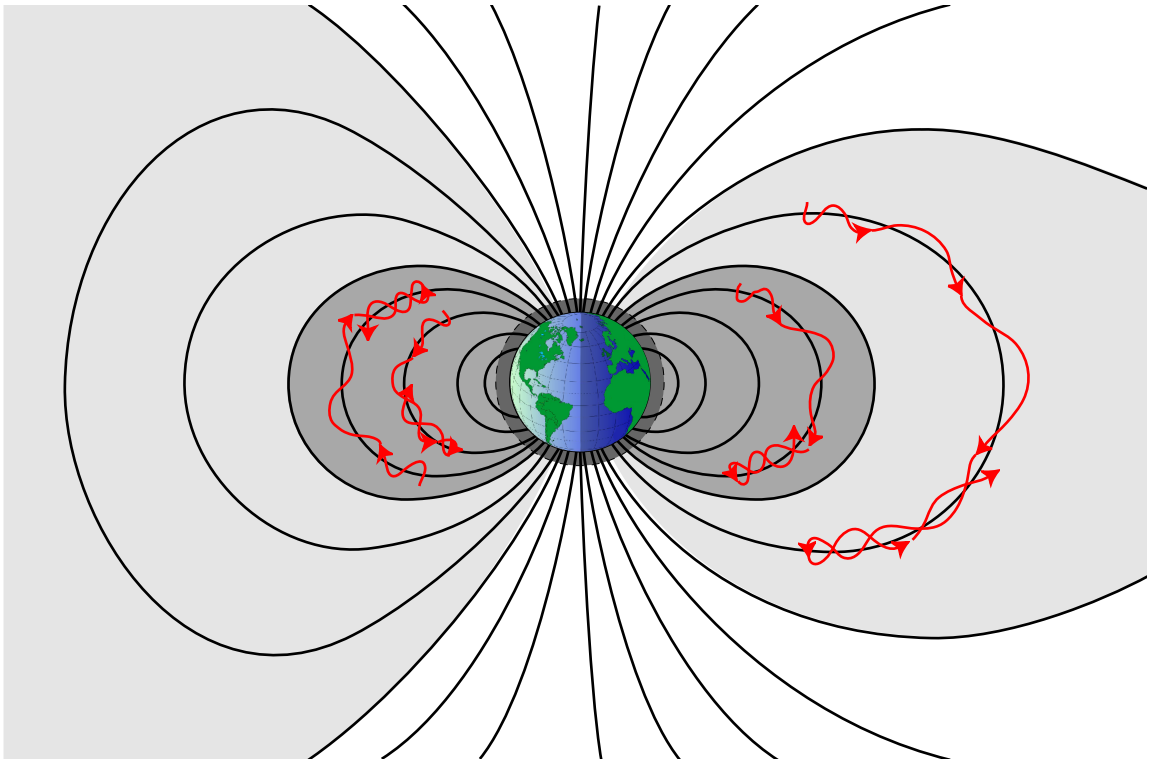

Figure 1.3: Representation of the inner magnetosphere. The black lines represent the geomagnetic field lines. The gray scale colors represent cold plasma density inside and beyond the plasmapause. The red lines represent trajectories of trapped energetic electrons that make up the hot plasma of the radiation belts. Adapted from [*Gibby*, 2008].

but significant populations of 'hot' plasma characterized by densities below 1 cm^{-3} but with high energies ranging from 1 keV to several MeV. The energetic particles that constitute the hot plasma are trapped in the mirror geometry of the magnetic field where they execute a helical gyro-motion around the magnetic field lines and 'bounce' between the opposite hemispheres as shown in Figure 1.3. Collectively, the hot plasma populations in the magnetosphere are referred to as the 'Van Allen belts' or simply the radiation belts [*Tascione*, 1994, Sec. 4.8].

While the cold plasma governs the propagation characteristics of electromagnetic waves in the magnetosphere, it is the hot plasma that drives instabilities and supports wave-particle interactions that can lead to wave amplification, particle acceleration,

and particle loss through pitch angle scattering. Interactions of waves with hot plasma populations in the magnetosphere constitute a rich field of study and continue to be the subject of both experimental and theoretical work over a broad range of frequencies and interaction modes [*Platino et al.*, 2004; *Omura and Summers*, 2006; *Omura et al.*, 1991; *O'Brien et al.*, 2003; *Hui and Seyler*, 1992]. The specific wave-particle interaction considered here is the whistler mode instability, also variously referred to as the coherent wave instability, non-linear magnetospheric amplification, or the VLF triggered emission phenomenon. The whistler mode instability occurs for waves propagating in the whistler mode, which describes electromagnetic waves propagating in a magnetized plasma with frequencies below the electron cyclotron frequency and electron plasma frequency but above the proton cyclotron frequency. In the Earth's magnetosphere such waves can undergo resonant interactions with energetic electrons in the keV energy range.

Even without the inclusion of hot plasma interactions, the propagation of whistler mode waves in the magnetosphere is complicated by the anisotropic and inhomogeneous nature of the medium. Generally, whistler mode waves in the magnetosphere propagate along complex trajectories that are governed by the evolution of the angle between the wave normal vector ($\mathbf{k}$) and the geomagnetic field ($\mathbf{B}_0$). This angle changes dynamically during propagation through the magnetosphere, which is inhomogeneous in terms of both the cold plasma distribution and geomagnetic field geometry. [*Helliwell*, 1965, Sec. 3.4]. Furthermore, the direction of propagation of wave energy is not along the $\mathbf{k}$-vector direction, due to the anisotropy of the medium. An example of a whistler mode ray trajectory originating from a terrestrial source is shown in Figure 1.4 by the blue ray path. Typical of such a ray path is the abrupt reversal of direction known as a magnetospheric reflection (MR) [*Lyons and Thorne*, 1970]. The MR effect prevents many whistler mode waves, whether terrestrial or magnetospheric in origin, from reaching the lower ionosphere, thus rendering them not observable on the Earth. Furthermore, even for the subset of trajectories that do reach the lower ionosphere, the sharp plasma gradients therein lead to total internal reflection of most wave energy. Only waves with $\mathbf{k}$-vectors oriented near normal to the lower ionospheric surface can penetrate into the Earth-ionosphere waveguide and

be observed on the ground [*Sonwalkar and Harikumar*, 2000].

However, the magnetosphere regularly contains field-aligned density enhancements which can efficiently guide waves and thus greatly simplify their trajectories [*Angerami*, 1970]. These density enhancements are commonly referred to as 'ducts' and guide whistler mode waves in the same manner as optical fibers guide waves in the visible band, namely via confinement through an index of refraction gradient transverse to the direction of propagation [*Helliwell*, 1965, Sec. 3.6]. The effect of a duct on whistler mode propagation can be qualitatively depicted as in the red ray path in Figure 1.4, which shows a trajectory confined to propagation along the geomagnetic field line and therefore intersecting the lower ionospheric boundary. A ducted ray path intrinsically implies a **k**-vector parallel, or close to parallel, to the geomagnetic field line. Consequently, waves along such a path impinge onto the ionospheric boundary near normal to the density gradients and penetrate to the ground. In contrast to non-ducted waves, waves in ducts can readily be observed on the ground at predictable locations, namely near points where a magnetic field line associated with a duct intersects the Earth's surface.

A convenient coordinate for describing positions in the magnetosphere with reference to the geomagnetic field is the McIlwain L-parameter. The L-parameter is used to specify the surfaces along which particles trapped in the geomagnetic field move. The L-value of a given drift shell in the real geomagnetic field corresponds to the equatorial crossing in Earth radii, of the equivalent drift shell (i.e., the particles that have the same adiabatic invariants) in a titled, off-centered dipole model of the Earth's magnetic field. Thus if a magnetic field line or position in the magnetosphere is specified using its L-value, it corresponds roughly to a position on a dipole field line that crosses the magnetic equator at L Earth radii [*Walt*, 1994, Chap. 4]. Two locations on the Earth's surface in opposite hemispheres but along the same geomagnetic field line, or L-shell, are referred to as magnetic conjugate points.

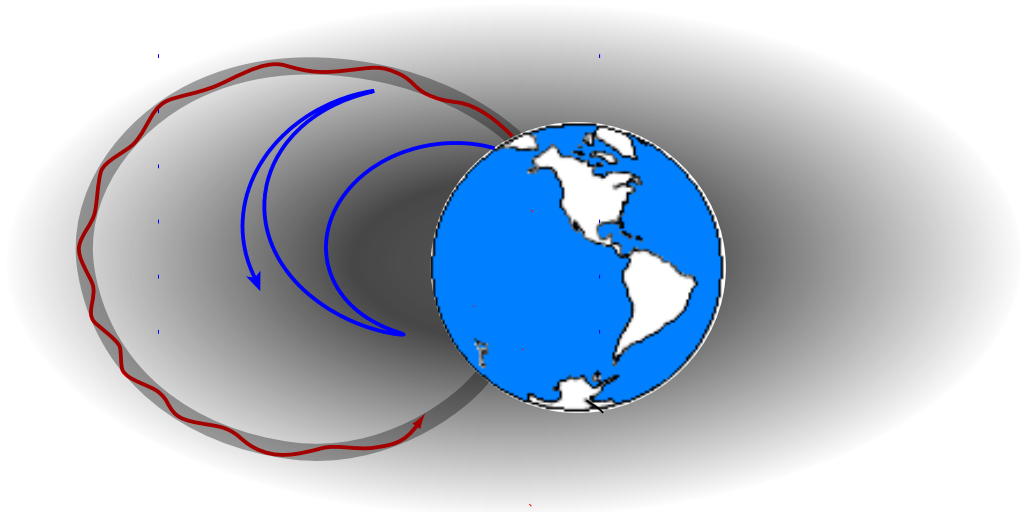

Figure 1.4: A representation of propagation trajectories of whistler mode waves in the magnetosphere. Both the blue ray path and the red ray path are for signals initially launched at the Earth's surface. The blue ray path is not ducted and undergoes magnetospheric reflections (MR). The red ray path represents ducted propagation along the geomagnetic field line. The ducted path returns to the ionosphere in the southern hemisphere and because it arrives with near-vertical incidence it will penetrate the ionosphere and be observed on the ground.

1.3 Whistler Mode Wave Injection Experiments

Ducted propagation of whistler mode waves in the magnetosphere facilitates the realization of an experimental concept in which signals of known terrestrial origin can be observed on the ground after propagation through the magnetospheric plasma along a known path. In the simplest case, such a propagation path involves a single traverse between conjugate points by way of the magnetosphere. In fact the first knowledge of the plasma content of the magnetosphere came from the correct interpretation of the origin of naturally occurring radio signals known as 'atmospheric whistlers,' so named because of their characteristic whistling sound when played through a speaker.

These signals were shown by *Storey* [1953] to originate from impulsive lightning induced radiation that had been dispersed by propagation along a ducted path through the magnetospheric plasma.[1] *Carpenter* [1963] used observations of whistlers to map the cold plasma distribution in the magnetosphere and discover the plasmapause. The successful usage of whistler data led to the use of signals injected by man-made sources for magnetospheric probing and observation of hot plasma effects in addition to the dispersion which is governed predominantly by the cold plasma population.

1.3.1 Early Experiments and Observations

The VLF triggered emission phenomenon induced by a man-made source was first identified in 1964 in data originally recorded in 1959 [*Helliwell et al.*, 1964]. The signal from the 18.6 kHz US Navy NPG communication transmitter in Jim Creek, Washington was observed, after ducted magnetospheric propagation, in Wellington, New Zealand. The main features of the instability were identified to be temporal amplification as observed at a stationary receiver and the triggering of free running emissions such that additional frequency components are generated. Further examples of the phenomenon were found in VLF recordings made on board the USNS *Eltanin* in 1961, showing that amplified signals and triggered emissions were induced by the 14.7 kHz NAA transmitter in Cutler, Maine [*Helliwell*, 1965, Sec. 7.2].

Upon identification of this unique and dynamic but yet highly repeatable phenomenon, efforts were undertaken to investigate it with a controlled experiment employing dedicated hardware. In 1966−1969 a VLF transmitter was established near Byrd Station, Antarctica (80.02° S, 119.53° W). In a setup that came to be known as Byrd Longwire, a long antenna was laid out on the Antarctic ice for generating VLF waves for magnetospheric wave injection. The Byrd configuration was unfortunately far from ideal as the proximity of the snow, made worse by immediate snow accumulation over the antenna, led to substantial near field losses and reduction of radiation efficiency. Furthermore, movement of the ice created frequent breaks in the wire. Despite successful ionospheric sounding and reception of signals on the OGO 4

[1] This is the origin of the name *whistler* mode.

spacecraft, signals from the Byrd transmitter were never observed at the conjugate point [*Helliwell and Katsufrakis*, 1974, 1978].

Another experiment worthy of mention is the transportable VLF transmitter with a 1200 m balloon suspended antenna that transmitted 6.6 kHz signals from Port Heiden, Alaska in 1973. Several cases of the VLF triggered emission instability were successfully observed at the conjugate point in Dunedin, New Zealand even though the vertically oriented antenna was not optimal for launching waves into space [*Dowden et al.*, 1978]. Nevertheless, observations and transmissions were limited as the experiment was intrinsically temporary in nature.

1.3.2 Siple Station

The first long term, and to this day most referenced, magnetospheric wave injection experiment was that operated by Stanford University at Siple Station, Antarctica from 1973 to 1988. The site of the Siple Station facility (75.93° S, 84.25° W) was chosen because of the accessibility of its conjugate point (located near the city Roberval, Québec), its magnetic latitude offering access to the plasmapause, and because the site was known to be an excellent location for observations of naturally occurring magnetospheric emissions and whistlers [*Helliwell*, 1970]. Perhaps most important in the selection criteria was that the site was atop a 2 km thick ice sheet that elevated the horizontal antenna above the conducting ground plane a significant fraction of a wavelength. This elevation combined with the many kilometer length of the antenna allowed the transmitter to have a reasonable radiation efficiency of $1-3$ % [*Raghuram et al.*, 1974].

The original installation was a 80 kW transmitter and 21.2 km antenna with resonant frequency of approximately 5 kHz [*Helliwell and Katsufrakis*, 1974]. This facility was later upgraded to a 150 kW transmitter and two 42 km long antennas arranged in a crossed dipole geometry leading to a resonant frequency of 2.5 kHz and an estimated radiated power of 1.5 kW [*Carpenter and Bao*, 1983; *Helliwell*, 1988; *Gibby*, 2008]. The Siple transmitter excited magnetospheric wave amplification and triggering in the $1.5-6$ kHz frequency range and on magnetospheric paths ranging from $L \simeq 3$ to

$L \simeq 5$. The facility itself was located at $L \simeq 4.3$. An example of the observations from the Siple experiment can be seen in Figure 1.5, showing spectrogram records from a receiver at Siple Station in Antarctica and also from the conjugate point in Roberval, Québec. A 2 second long pulse at 1.4 kHz is initially transmitted at 0.5 seconds in the record. Approximately 1.5 seconds later the signal arrives at the northern hemisphere after propagation through the magnetosphere in the whistler mode, as shown in the lower right inset. Such a signal that has completed a single inter-hemispheric traverse through the magnetosphere is referred to as a '1-hop echo.' Subsequent to the 1-hop echo observation in the north, the signal is seen to return to the southern hemisphere at which time it is termed to be a '2-hop echo.' Typical of the magnetospheric wave-particle interaction, each traverse through the magnetosphere causes the signal to be not only amplified but also results in the creation of free running emissions at frequencies extending well away from that of the original transmission.

The Siple Station experiment produced many years of excellent observations of whistler mode wave amplification and triggering of emissions which continue to form a foundation for current experimental and theoretical efforts in the field. Unfortunately, the cost of the logistics support of the facility was very high. The station was closed in 1988 and the site was abandoned. Given that snow accumulation on the Antarctic peninsula in that region is $\sim$1.8 meters a year, the remnants of the Siple Station facility are now buried under tens of meters of snow and any resurrection of the station is unlikely.[2]

1.3.3 HF Ionospheric Heating

As was indicated in Section 1.3.2, one of the challenges in operating a whistler mode wave injection experiment is generating waves in the appropriate frequency band. In the magnetosphere whistler mode waves propagate at frequencies from a few hundred Hz to tens of kHz, with corresponding free space wavelengths of tens to thousands of kilometers. Since efficient generation requires both the antenna dimensions and the separation from the ground plane to be on the order of a wavelength, construction of

[2]For a recently compiled history and assessment of the Siple Station facility see Chapter 2 of *Gibby* [2008].

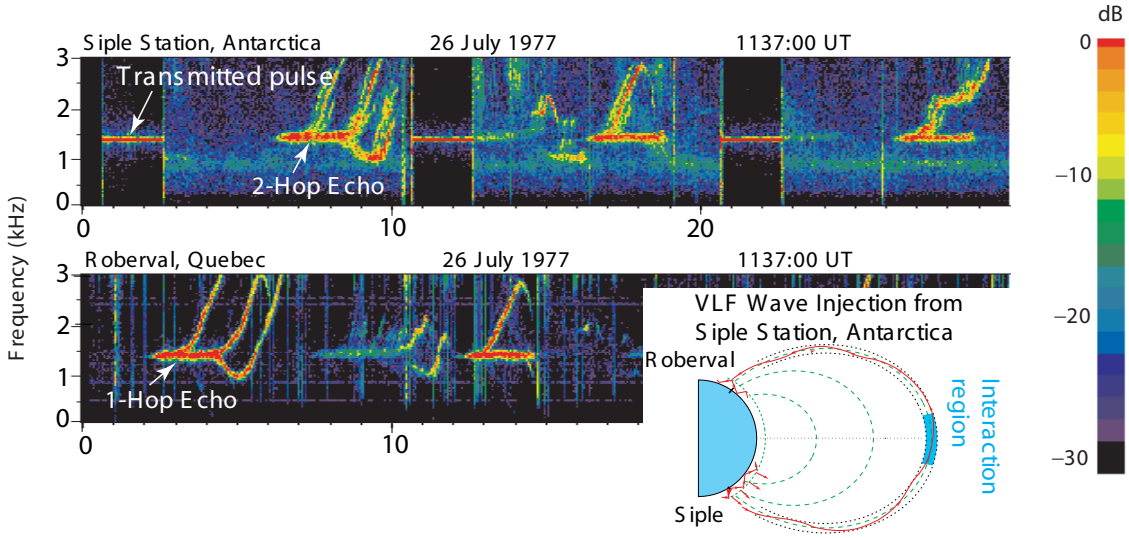

Figure 1.5: Observations from the Siple Station experiment showing a 1.4 kHz transmitted pulse (top panel), a 1-hop echo observed at the conjugate point in northern hemisphere (bottom panel) and a subsequent 2-hop echo observed in hemisphere of origin. The phenomena repeats for the subsequently transmitted pulses. The echoes are amplified and contain free running emissions of changing frequency typical of the whistler mode instability. The inset in the lower right illustrates the Siple experiment setup.

the appropriate hardware poses a considerable engineering challenge. In fact, apart from unique locations like the Antarctic ice sheet used as a platform for the Siple Station facility, achieving the necessary elevation for a man-made horizontal (skyward directed) dipole is nearly impossible.

Due to the challenges of constructing the necessary geometries for ELF/VLF wave generation, an attractive alternative involving taking advantage of naturally occurring ionospheric currents has been pursued since the 1970's [*Getmantsev et al.*, 1974; *Stubbe et al.*, 1977, 1982]. High Frequency (HF) waves in the 1−10 MHz band have wavelengths on the scale of meters and can thus be efficiently generated. With sufficient power, HF radiation can be used to change the temperature of electrons in the ionosphere at altitudes of 60−100 km. Since the conductivity of the ionospheric plasma depends on the electron temperature, HF heating allows for modification of

the natural currents flowing in the ionosphere. Periodic heating at an ELF/VLF frequency can transform the largely DC (or very slowly varying) ionospheric currents into a giant radiating antenna in the sky, suitably elevated and oriented for radiating waves into the magnetosphere as well as into the Earth-ionosphere waveguide. Several facilities have been constructed around the world which are capable of performing such wave generation. Although the present work represents the first instance of the successful use of HF heating for whistler mode wave injection experiments, a brief review of the most important HF heater ELF/VLF wave generation facilities and results provides valuable context and is provided below.

Tromsø, Norway

The European Incoherent Scatter (EISCAT) Association has extensively used the HF heating facility near Tromsø, Norway to generate ELF/VLF signals by modulating the overhead auroral electrojet currents with 1 MW of radiated HF power in the 2.7−8.0 MHz band [*Barr and Stubbe*, 1991]. ELF/VLF signals were typically produced using square wave amplitude modulation in the 200 Hz to 6.5 kHz frequency range with observed amplitudes of ∼1 pT, ∼0.1 pT and ∼0.03 pT at respective ground distances of ∼20 km, ∼200 km and ∼500 km from the heating facility [*Stubbe et al.*, 1982; *Barr et al.*, 1985]. Being the first facility to operate continuously for many years with a high radiated power, the Tromsø experiment brought to light many characteristics of HF heater induced ELF/VLF generation that would later be confirmed with other facilities and are today considered conventional. At distances of less than ∼100 km, the observed ELF/VLF amplitudes exhibited maxima in frequency near multiples of ∼2 kHz. These peaks were shown to be the result of vertical resonances in the Earth-ionosphere waveguide. Heating with X-mode polarization of the HF waves was shown to be more effective in generating ELF/VLF waves than heating with O-mode polarization, with corresponding amplitudes observed on the ground exhibiting a 3 dB difference.[3] The variations in ELF/VLF signal amplitude on time scales of hours and

[3]In the context of HF heating, X-mode and O-mode polarization simply defines the sense of rotation of the wave fields. X-mode polarization is defined as a radio wave entering the ionosphere with right hand elliptical polarization in the northern magnetic hemisphere (or left hand in the southern hemisphere). O-mode polarization involves rotation in the opposite sense. These polarizations

days have shown correlation with geomagnetic activity represented by the K_p index [*Barr et al.*, 1985]. This correlation results from the fact that the auroral electrojet is driven by dynamics in the magnetosphere. Electric fields in the magnetosphere, which can be enhanced during disturbances, are mapped down to the ionosphere via geomagnetic field lines. Additionally, accompanying precipitation of energetic particles causes enhancements of ionospheric conductivity [*Baumjohann*, 1983]. The electric fields drive currents via Ohm's Law, which for the anisotropic ionospheric plasma needs to be expressed as a 3-dimensional tensor equation. Generated ELF/VLF amplitudes were shown to be well correlated with the electrojet electric field (even on short sub-hour timescales). Polarization measurements led to the conclusion that it is modulation of the ionospheric Hall conductivity that is the dominant radiator of ELF/VLF waves observed in ground based measurements [*Rietveld et al.*, 1983, 1987].

Unfortunately, although Tromsø generated signals were observed in space [*James et al.*, 1984, 1990], the facility is not useful for the ducted whistler mode wave injection experiments of the type performed at Siple Station. Located at $L > 6$, Tromsø is on sub-auroral/auroral field lines that are mostly 'open' and on which conditions for hemisphere-to-hemisphere ducting are much less favorable [*Carpenter and Šulić*, 1988].

Arecibo, Puerto Rico

Several ELF/VLF wave generation experiments have been performed by modulating the equatorial electrojet current using a heater located at the Arecibo Observatory in Puerto Rico. During these experiments, ELF/VLF waves were produced over a frequency range of 500 Hz to 5 kHz using a heater frequency of approximately 3 MHz and a total input power of 800 kW [*Ferraro et al.*, 1982]. In addition to confirming characteristics observed in the Tromsø experiments, the dependence of the ELF/VLF amplitude on the duty cycle of the modulation was investigated. *Ferraro et al.* [1984] found that a 48% duty cycle yielded maximum ELF/VLF amplitudes. ELF/VLF wave generation can exhibit sensitivity to duty cycle because of differences

should not be confused with *ordinary* and *extraordinary* modes of propagation in a cold magnetized plasma.

in the heating and cooling rates of ionospheric electrons. This sensitivity intrinsically depends on the ELF/VLF frequency in question and also on the heating/cooling rates themselves which vary with altitude.

HIPAS, Alaska

The High Power Auroral Stimulation (HIPAS) facility, near Fairbanks, Alaska, has been used in a number of experiments to modulate the auroral electrojet to produce ELF/VLF waves. The HIPAS facility radiates 800 kW of power at 2.85 MHz. Most notably, the HF heater was used to create ELF/VLF waves through three different modulation techniques, amplitude modulation, phase modulation, and beat-frequency modulation. It was generally found that amplitude modulation yielded the best results [*Villaseñor et al.*, 1996]. ELF/VLF signals generated by HIPAS were also observed in space aboard the Akebono satellite [*Kimura et al.*, 1991].

1.3.4 The HAARP Facility

The High Frequency Active Auroral Research Program (HAARP) began the construction of an ionospheric heating facility in 1990 near the town of Gakona, Alaska. The HAARP heater was originally a 96 element crossed dipole array capable of radiating 960 kW of power. In 2007 a planned multi-year upgrade of the facility was completed, bringing the number of elements to 180 and the radiated power to 3.6 MW, making HAARP the most powerful ionospheric heating facility in the world. ELF/VLF waves generated by HAARP were first observed by *Milikh et al.* [1999] and in subsequent years observations were reported at distances of up to 4400 km [*Moore et al.*, 2007] and in space [*Platino et al.*, 2004, 2006]. *Cohen et al.* [2008b] showed that in the far field, the effective radiation pattern of the HAARP induced ELF/VLF is that of a dipole. Besides an unprecedented level of radiated power, the HAARP facility also provides for increased flexibility in beam phasing and steering. HAARP's unique capabilities have allowed for new methods of ELF/VLF generation other than the conventional amplitude modulation [*Cohen et al.*, 2008a].

Unlike other heating facilities, HAARP's location at $L \simeq 4.94$ (at 85 km altitude) is

favorable for conducting ducted whistler mode wave injection experiments, a project which has been led by Stanford University. Figure 1.6 shows a schematic of the HAARP wave injection experiment, the results of which are the subject of the present work. ELF/VLF waves generated in the ionosphere above HAARP are injected into the Earth-ionosphere waveguide and also into the magnetosphere. Waves in the magnetosphere travel in ducts to the equatorial region where they undergo a wave-particle interaction with radiation belt electrons. The amplified waves are observed at the HAARP conjugate point as 1-hop echoes and subsequently in the northern hemisphere as 2-hop echoes. In addition to wave amplification and triggering, the wave particle interaction can cause pitch angle scattering and precipitation of energetic particles onto the ionosphere.

1.4 Thesis Organization

The present work is organized into 7 chapters.

Chapter 1, the present chapter, introduces the relevant background and motivation for this work.

Chapter 2 describes the experimental setup and presents observations of magnetospherically amplified signals resulting from several years of experimental investigations.

In Chapter 3 we analyze the sensitivities and occurrence properties of the observations.

In Chapter 4 we present the theoretical treatment of VLF triggered emissions and put our observations in the context of numerical simulations.

Chapter 5 presents observations and analysis of a new phenomenon of cross modulation between whistler mode signals and HF ionospheric heating. The concept is investigated as a new technique for generating signals with HF heating.

In Chapter 6 we address the detection of energetic particle precipitation induced by HAARP ELF/VLF transmissions using both computer modeling and qualifying observations.

Chapter 7 is a summary and includes suggestions for future work.

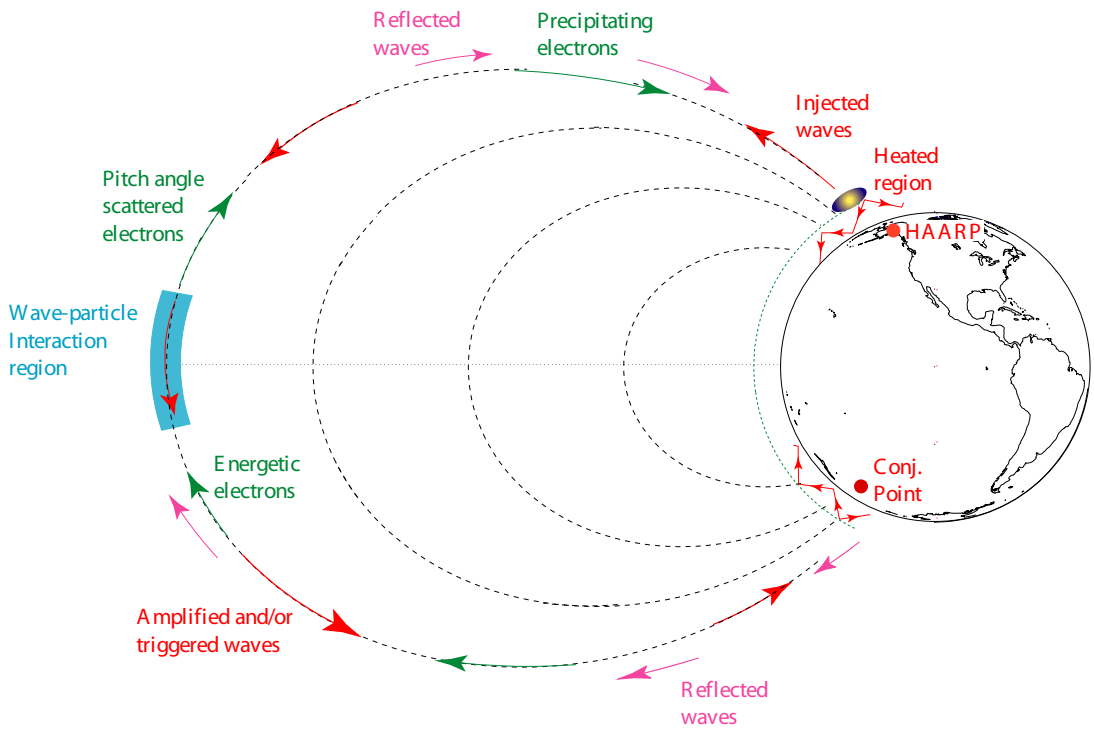

Figure 1.6: A schematic of the HAARP whistler mode wave injection experiment. ELF/VLF waves generated in the ionosphere above HAARP are injected into the Earth-ionosphere waveguide and into the magnetosphere. Waves in the magnetosphere propagate in ducts to the wave-particle interaction region at the equator. Amplified waves can be observed at the conjugate point or, if reflected from the lower ionospheric boundary and coupled back into the duct, also in the northern hemisphere in the vicinity of the HAARP facility. Energetic electrons are scattered in pitch angle and precipitate onto the ionosphere.

1.5 Scientific Contributions

The specific contributions of the present work can be summarized as follows:

1. We present the first observations of magnetospheric amplification and triggering of emissions by signals generated by HF ionospheric heating thereby providing a new platform for controlled wave injection experiments. Repeated observations

of amplified signals, and associated triggered emissions were made in conjugate hemispheres using custom designed receiver equipment for ocean based measurements in the southern hemisphere.

2. We characterize the occurrence of observations of the magnetospherically amplified signals with respect to transmitter parameters and methods of excitation, as well as background geomagnetic conditions. The magnetospheric propagation paths and associated cold plasma densities traversed by the HAARP induced echoes are determined. We identify magnetospheric propagation conditions as a likely limiting factor in HF heater induced echo observations

3. The observations are analyzed in the context of theoretical and numerical models. Phase and amplitude of the observed signals are used to determine the temporal behavior of the non-linear resonant current vector. We use ground based observations to infer hot plasma distribution dynamics.

4. We present the first observations of a new phenomena of cross modulation between whistler mode signals and HF ionospheric heating and use the concept as a new method to generate ELF/VLF radiation using an HF heater.

5. We provide an assessment of capabilities for ground based detection of electron precipitation induced by HAARP generated whistler mode signals. We evaluate the effects of HF heating on the VLF remote sensing technique. We predict of precipitation for non-ducted HAARP ELF/VLF signals using a ray tracing and particle scattering simulation code.

Chapter 2

Experiment Setup and Observations

Magnetospheric wave injection experiments with the HAARP facility were first performed in late 2000 and continue to be actively pursued at the time of this writing. The global scales of the experiment and specifically the location of the conjugate point pose many logistical and operational challenges. Consequently, although the scientific premise of the experiment has not changed significantly, the hardware and operational approach have evolved over a period of several years. In this chapter we outline the experiment setup and present the accumulated observations.

2.1 Experiment Setup

2.1.1 Northern Hemisphere

The HAARP facility is located at 62.4°N and 145.2°W geographic (63.1°N and 92.4°W geomagnetic). Since February 2007, the HAARP array is capable of radiating 3.6 MW of HF power at frequencies in the 2.75−9.8 MHz band. The array can be phased to tilt the beam a maximum of 15° from zenith in any direction. For observation of 2-hop echoes and HAARP generated ELF/VLF signals, an array of radio receiver stations

has been established across the state of Alaska. The site nearest to the HAARP facility is Chistochina, located 36 km to the northeast. Initial receiver site installations began in 2000, and were followed by many upgrades and subsequent deployments. A key requirement for successful observations is lack of local electromagnetic interference. In the ELF/VLF band, the most common source of interference is radiation from power lines whose harmonics can extend up to 6 kHz. Despite best efforts to deploy equipment in remote locations, preferably not connected to the commercial power grid, finding suitable locations is difficult, especially with the expansion of commercial power in Alaska. The map in the top row of Figure 2.1 shows the location of the most important Stanford receiver sites in Alaska. The ELF/VLF receivers use large square (4.8 m by 4.8 m) or triangular (4.2 m high with 8.4 m base) air core antennas, with terminal resistive and inductive impedances respectively of 1-Ω and 1-mH, matched to a low-noise preamplifier with a flat frequency response ∼300 Hz to ∼47-kHz. Recordings are made with 16 bit 100 kHz digital sampling, synchronized to GPS timing signals allowing for 200 nanosecond timing accuracy at all stations. Since 2005 all receivers have been of the AWESOME type design described by *Cohen et al.* [2009].

2.1.2 Southern Hemisphere

The conjugate point of the HAARP array is located in the South Pacific Ocean (56.67°S and 174.48°E) about 1000 km southeast from New Zealand and ∼500 km from the nearest landmass of Campbell Island. Consequently, radio observations at the conjugate point can only be made using ships or floating buoy platforms. Deployment of a buoy based system is made all the more difficult by the fact that the ocean depth of 5400 meters is at the upper limit for tested mooring systems and the area is known to host extreme weather conditions with $10-15$ meter wave heights regularly observed. Nevertheless, Stanford University managed to deploy a total of three autonomous buoy receivers in addition to making numerous observations with ship borne receivers.

The first Stanford buoy receiver, Buoy 1.0, was deployed in April 2004 at the

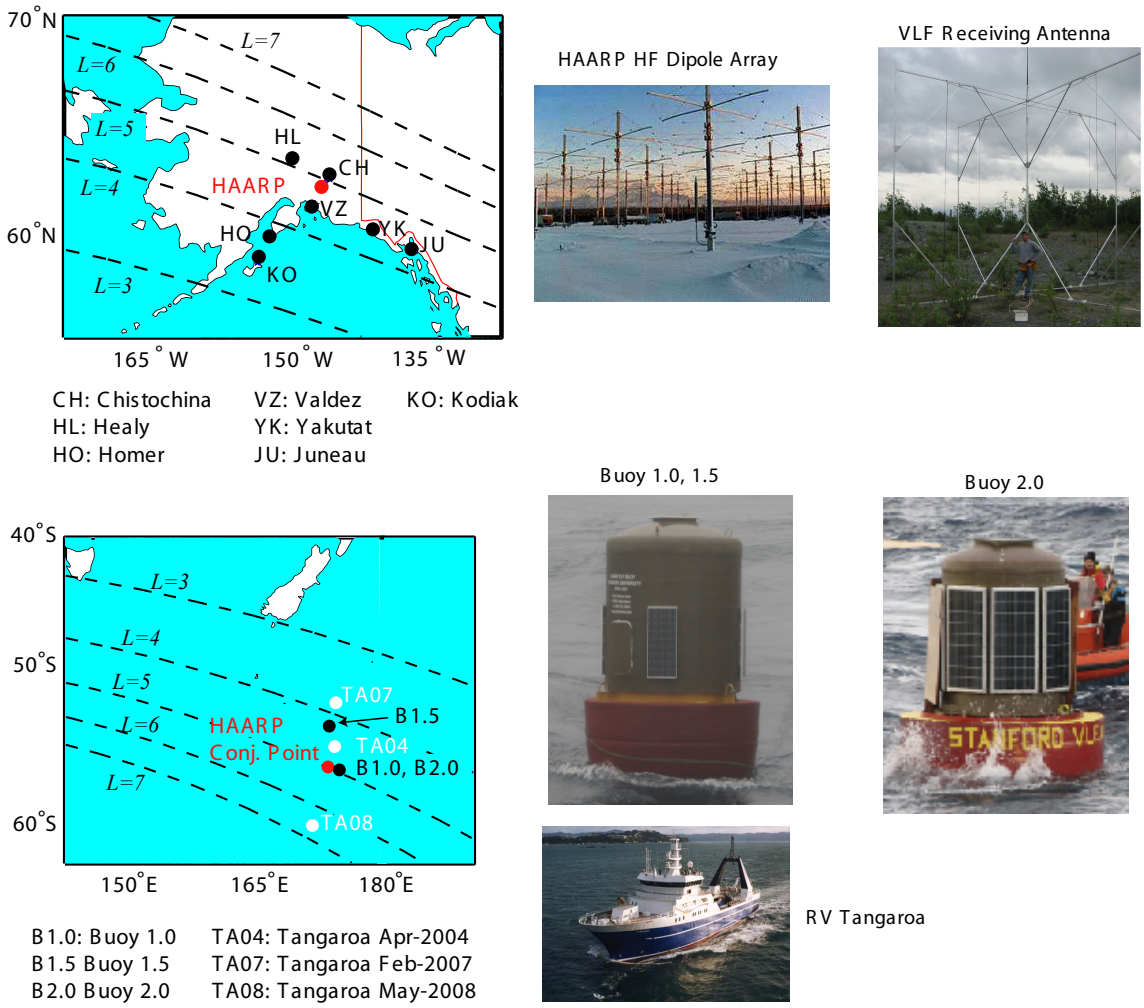

Figure 2.1: Maps showing receiver locations in the northern and southern hemisphere and photographs of selected hardware.

HAARP conjugate point. The ∼3600 kg (∼8000 lb) Buoy 1.0 structure consisted of a 2.5 meter cylindrical fiberglass dome atop an aluminum hull enclosed in floatable foam (see Figure 2.1). The mooring system had a record 7 km length consisting of segments of chain, metal wire, nylon rope, and polypropelene rope. The receiving antennas and ELF/VLF data collection were similar to the hardware used in the northern hemisphere except that the sampling frequency was lowered to 12 kHz since

data storage and transfer were very limited. The air core loop antennas were embedded into the structure of the fiberglass dome. The unique challenge in the buoy receiver was that the system had to be fully autonomous, with scheduling and data transfer controlled remotely with no planned recovery of the system. In an effort that involved considerable custom hardware and software development, a system was implemented with communication via IRIDIUM satellite modem and data storage on Compact Flash cards. Power was supplied through a massive battery bank supplemented with photovoltaic panels. Due to the extremely low telemetry rates of the IRIDIUM system (2.4 kbps), recordings were made synoptically and data were processed into compressed spectrogram records in JPG format for transmission. Raw data could also be transmitted if necessary. The Buoy 1.0 system operated until January 2005 when an unexpected break of the mooring line required the launch of a rescue mission to recover the hardware.

Subsequent to the recovery of Buoy 1.0, two new buoy systems were developed and deployed. Buoy 1.5 utilized the same hull and dome as Buoy 1.0 but had upgraded electronics with considerable improvements to data storage and communication capabilities. The Buoy 2.0 system was housed in a newly acquired dome and hull and included more battery capacity and an expanded photovoltaic array. To achieve greater geographic spread in the conjugate point observations, Buoy 1.5 and Buoy 2.0 were deployed as shown in the map in Figure 2.1 in February and March of 2007. Both systems were operational several months after deployment and made valuable observations of HAARP induced 1-hop echoes. Unfortunately, data from Buoy 2.0 was compromised by impulsive noise, tentatively believed to originate from a cracked battery terminal or intermittent cable connection.

Additional observations in the conjugate region were made on board *RV Tangaroa* operated by New Zealand's National Institute of Water and Atmospheric Research (NIWA) and on *Nathaniel B. Palmer* operated by the National Science Foundation (NSF). *Tangaroa* was the ship used in the deployments of all the buoy receivers and also the recovery of Buoy 1.0. The ship-borne receivers and antennas were the same as those used in Alaska.

2.1.3 Spacecraft Observations

ELF/VLF waves generated by HAARP have been observed on the CLUSTER satellite at ∼26,000 km altitude [*Platino et al.*, 2004] and on the DEMETER satellite at ∼700 km altitude [*Platino et al.*, 2004]. The low altitude DEMETER satellite is particularly useful for observing HAARP induced echoes since it makes daily passes over the heating facility and its conjugate point. A description of the DEMETER satellite and its instruments, which include electric and magnetic field antennas as well as a particle detector, is given by *Parrot* [2006]. Recent observations of HAARP-induced ELF/VLF signals on DEMETER are presented by *Piddyachiy et al.* [2008].

2.1.4 Transmission Formats and Operation

Operational logistics associated with the HAARP facility necessitate that wave injection experiments are performed in campaigns, meaning periods of usually two weeks in duration during which transmissions are carried out daily for several hours. The HAARP facility can be used to modulate the electrojet currents with a wide variety of ELF/VLF frequency time-formats including pulses, frequency-time ramps, and chirps. In the initial experiments, transmission formats were rigidly scheduled in advance of a campaign and ELF/VLF data recordings were only analyzed after full recovery of raw data, usually a few weeks after the transmissions. While such a system was perhaps the most straightforward in implementation, it did not allow for modifications of the transmission format in response to changing ionospheric and magnetospheric conditions. As is shown in Section 2.2, the magnetospheric response is sensitive to both frequency and frequency-time signature of the injected waves. Beginning in 2007, in conjunction with the HAARP facility power upgrade, all of the receiver sites in Alaska were equipped with Internet connectivity and currently send 1-minute spectrograms in real time to a server at Stanford University. The online spectrograms allow for a near-real-time assessment of the ELF/VLF generation conditions and the magnetospheric amplification response. Using an Internet chat-room to communicate with the HAARP operator, transmissions can then be modified to respond to changing conditions. Such an arrangement has proven to be very effective

in exciting magnetospheric echoes by taking full advantage of favorable geomagnetic conditions. Similar near-real-time adjustment of transmitter parameters based on observations of natural signals and echoes was also used with success during the Siple experiments [*Helliwell*, 1988].

2.2 Observations

The current collection of whistler mode echo observations excited by the HAARP heater is quickly expanding with the continuing operation of HAARP wave injection experiments. It is likely that sufficient statistics will be compiled in the future to warrant the identification of typical observations or standard results. However, at the time of this writing, the diversity and variety of the observations make it worthwhile to briefly touch upon the majority of noted cases.

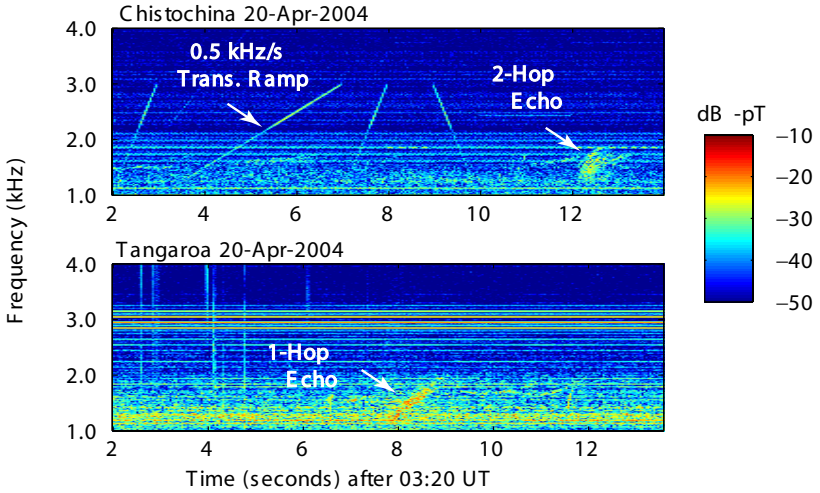

Figure 2.2: Spectrograms showing 1-hop echoes observed at the conjugate point on board *Tangaroa* (bottom panel) triggered by a 500 Hz/sec frequency-time ramp observed at Chistochina (top panel). The 2-hop echo is also visible in the Chistochina record.

2.2.1 First Observations: 20 April 2004

The first observations of HAARP induced whistler mode echoes occurred on 20 April 2004 during transmissions with the original 960 kW facility. One-hop echoes were observed on board *Tangaroa*, which was en route to deploy Buoy 1.0, and 2-hop echoes were observed simultaneously at Chistochina. The location of the ship at the time of the observations can be seen on the map in Figure 2.1. Figure 2.2 shows simultaneous spectrograms from Chistochina and Tangaroa[1]. One-hop and 2-hop echoes are observed to be triggered by the 500 Hz/sec frequency-time ramp. Only the 500 Hz/sec ramp shows amplification even though steeper ramps (1 kHz/sec) and pulses were transmitted in the same frequency range. The echoes continued to be observed for a period of ∼30 minutes during which multiple reflected hops, up to tenth order (i.e., 10-hop) were observed. The 20 April 2004 observations are reported by *Inan et al.* [2004].

2.2.2 Full Power HAARP

27 February and 4 March 2007

The upgrade of the HAARP facility to its full power and the inception of near-real-time monitoring of the experiment, as described in Section 2.1.4, led to an accompanied increase in the number of echo observations. In the first campaign at full power, which coincided with the deployment of Buoy 1.5 and Buoy 2.0, echoes were observed on two separate days. Figure 2.3 shows 1-hop echoes observed on *Tangaroa*, whose position at the time is denoted in Figure 2.1. The observed echoes are triggered primarily by a unique frequency-time format known as a 'snake' ramp which involves a continually increasing, but sinusoidally varying frequency-time slope. As is evident from the lower four panels of Figure 2.3, showing *Tangaroa* data observed at different

[1]The majority of spectrograms in this thesis are scaled by frequency resolution so that the intensity shown corresponds to an equivalent amplitude of a narrowband (purely sinusoidal) signal. The color axis is therefore appropriately labeled in dB-pT. It should be noted that traditionally, spectrograms have been presented as power spectral density using the corresponding units of power per bandwidth. Since locally observed HAARP generated ELF/VLF signals have negligible bandwidth, we find the narrowband approach to be more appropriate as it allows for reading the generated signal amplitude directly from the spectrogram.

minutes, the echo amplitude and frequency content show considerable variation. No 2-hop echoes were observed at Chistochina, nor at any of the sites in the northern hemisphere, even though 1-hop echoes were observed for approximately 30 minutes on board *Tangaroa*.

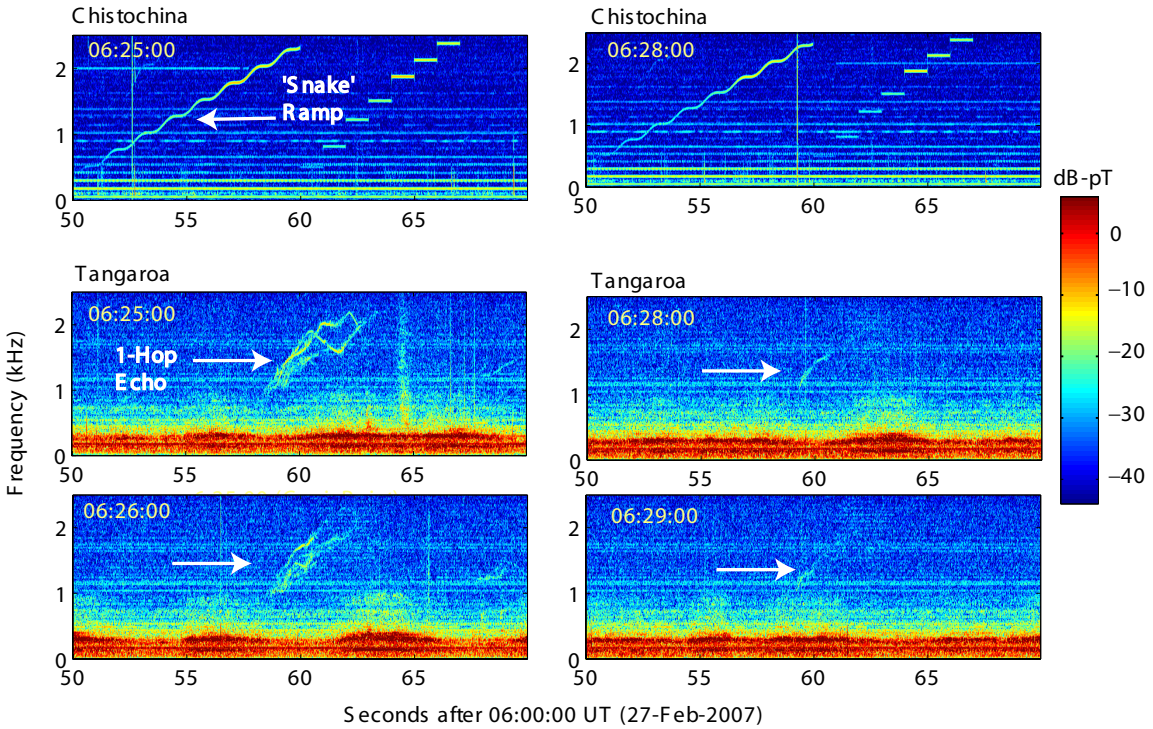

Figure 2.3: The top two records are spectrograms from Chistochina, while the bottom four are from *Tangaroa* at various minutes. One-hop echoes are observed to be triggered by a transmitted 'snake' ramp. The echoes exhibit considerable fading in amplitude and frequency content on the scale of minutes.

A few days later, on 4 March 2007, echoes of 3-second pulses at 1100 Hz were observed in both hemispheres on Buoy 1.5, Buoy 2.0, and at Chistochina. Observation of the 2-hop echoes abruptly commenced when the transmission format was changed from one with parabolic chirps and 1-second 1225 Hz pulses, to a format with 3-second 1100 Hz pulses, 1-second 900 Hz and 1600 Hz pulses, and a frequency-time ramp from 500 Hz to 3 kHz. Figure 2.4 shows spectra simultaneously observed at Chistochina (top panel), on Buoy 1.5 (middle panel), and from a later minute on

Buoy 2.0 (bottom panel). The data from Buoy 2.0 are compromised by impulsive interference radiated from the system electronics and manifested as vertical lines in the spectrum. The interference was mitigated using noise subtraction and echoes and triggered emissions are visible in between the remnant impulsive interference. The

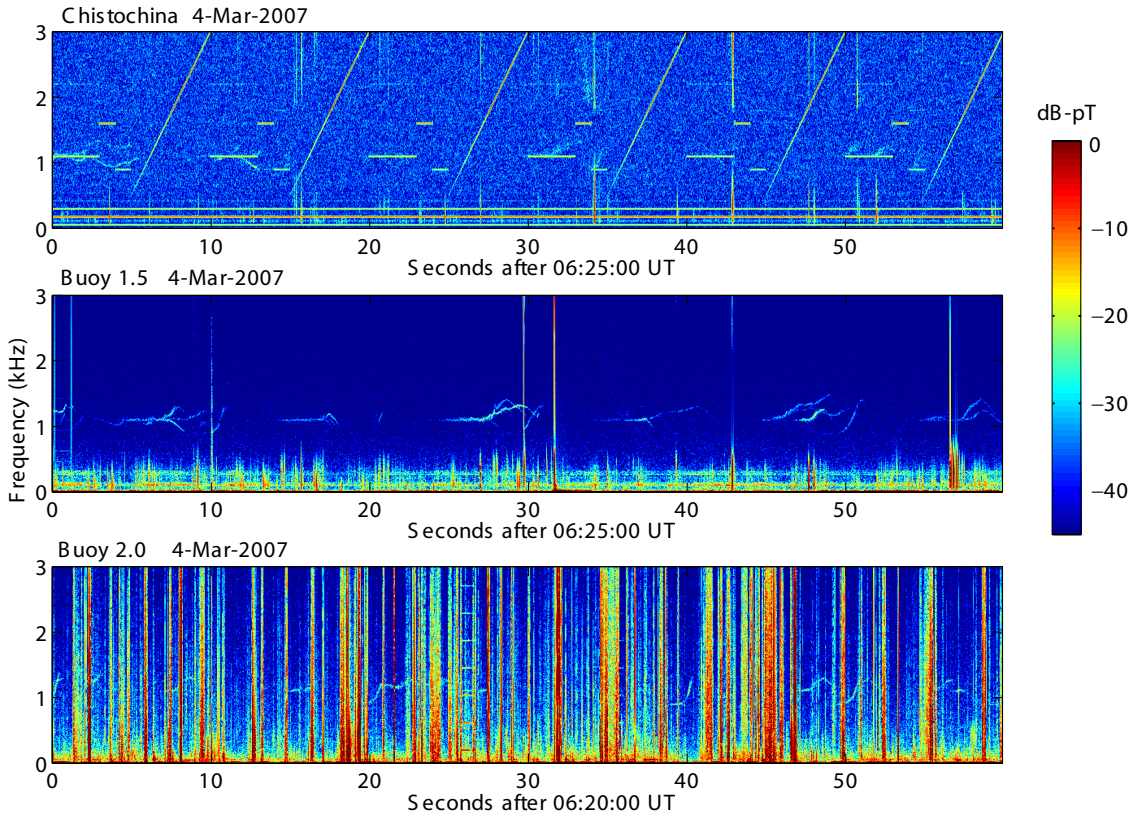

Figure 2.4: HAARP transmission and faint 2-hop echoes at Chistochina (top panel) and clear 1-hop echoes observed simultaneously on Buoy 1.5 (middle panel). The bottom panel shows echoes observed on Buoy 2.0 five minutes earlier when the transmission format was the same. The 2-hop echoes at Chistochina (top panel) appear superimposed on consecutive HAARP transmissions of the same frequency since the 2-hop propagation time and format repetition period are comparable, being 8.4 and 10 seconds, respectively.

observation of single frequency echoes on 4 March 2007 allows for quantification of temporal amplification resulting from the magnetospheric wave-particle interaction. Figure 2.5 shows temporal amplification of a 1-hop echo triggered by a 1.1 kHz pulse observed on Buoy 1.5. In this example the amplification rate is observed to be ∼10

dB/sec. In other cases, amplification rates as high as 30−50 dB/sec have been observed. In the Siple Station experiments amplification rates were reported to range from 20−150 dB/sec [*Helliwell*, 1988, and references therein]. The observations of 27 February 2007 and 4 March 2007 are reported by *Gołkowski et al.* [2008]

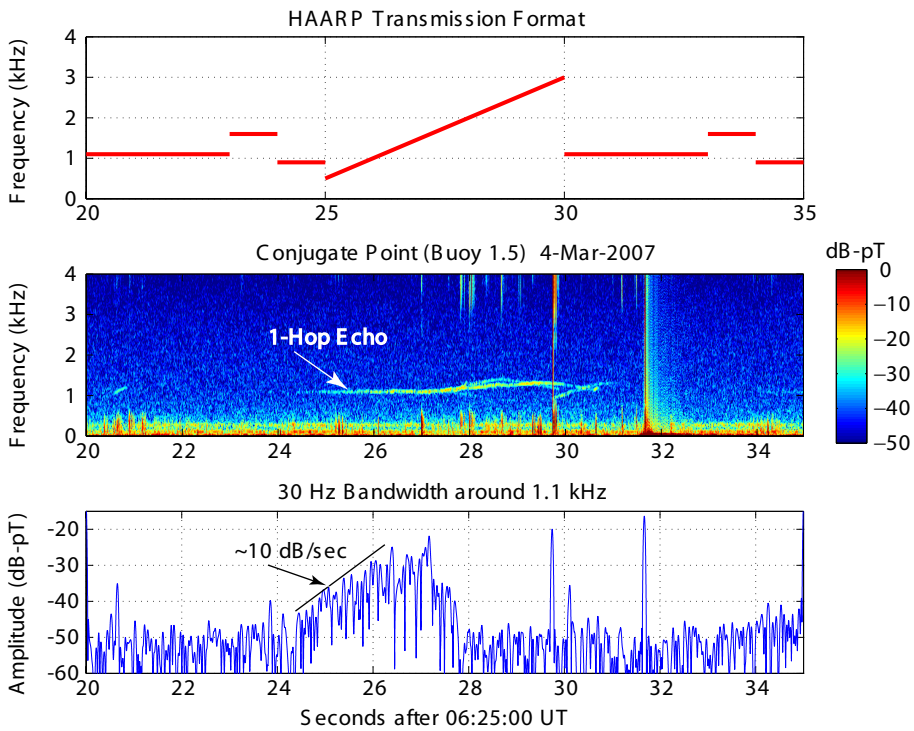

Figure 2.5: HAARP transmission format (top panel) and 1-hop echo of a 1.1 kHz pulse observed on Buoy 1.5 (middle panel). The frequency-time ramp is not observed to excite an echo even though it is in the same frequency range. The bottom panel shows the echo amplitude in a 30 Hz band around the transmitted pulse frequency.

23 August 2007

On 23 August 2007 2-hop echoes were observed at Chistochina with excellent signal to noise ratio (SNR), allowing for the identification of discrete magnetospheric propagation paths. The echoes were triggered by both pulses and frequency-time ramps in an 'active' frequency band spanning 1.6−2.6 kHz. Figure 2.6 shows the observed 2-hop

echoes and the effect of changing the transmitted ELF/VLF frequency to take advantage of the active band. In the left panel of Figure 2.6 the HAARP transmissions are just below 1.6 kHz and the only signals that excite echoes are weaker harmonics of the fundamental HAARP 3-second pulses which are at 1110 Hz, 1590 Hz, and 930 Hz. When the fundamental transmission frequency is increased (i.e., pulses at 2250 Hz, 1770 Hz and 2070 Hz), it can be seen in the right panel of Figure 2.6 that the corresponding echoes are higher in amplitude and richer in frequency content. Figure 2.7 shows another spectrogram showing data observed two minutes later where both ramps and pulses are seen to simultaneously excite 2-hop echoes.

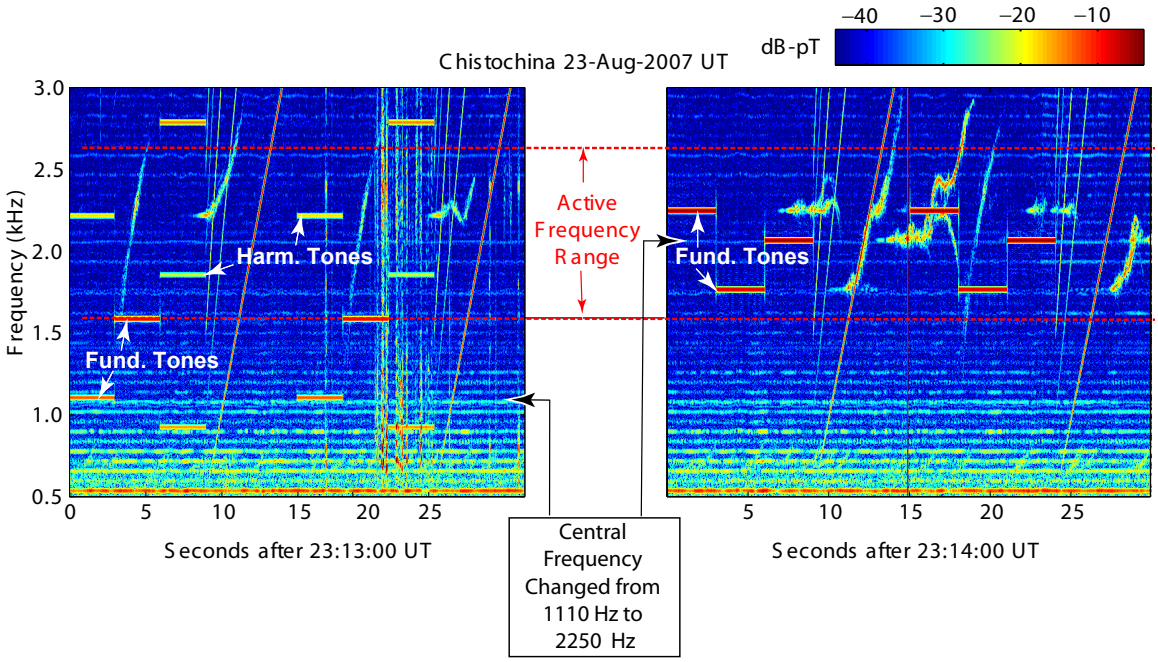

Figure 2.6: Two-hop echoes observed at Chistochina illustrating an active frequency range favorable for magnetospheric amplification. In the left panel only harmonics of pulses are in the active range. In the right panel, showing data from the subsequent minute, the transmission frequency has been changed to make all fundamental pulse frequencies fall in the active range, yielding higher amplitude 2-hop echoes.

On 23 August 2007 1-hop echoes were also observed on board the DEMETER

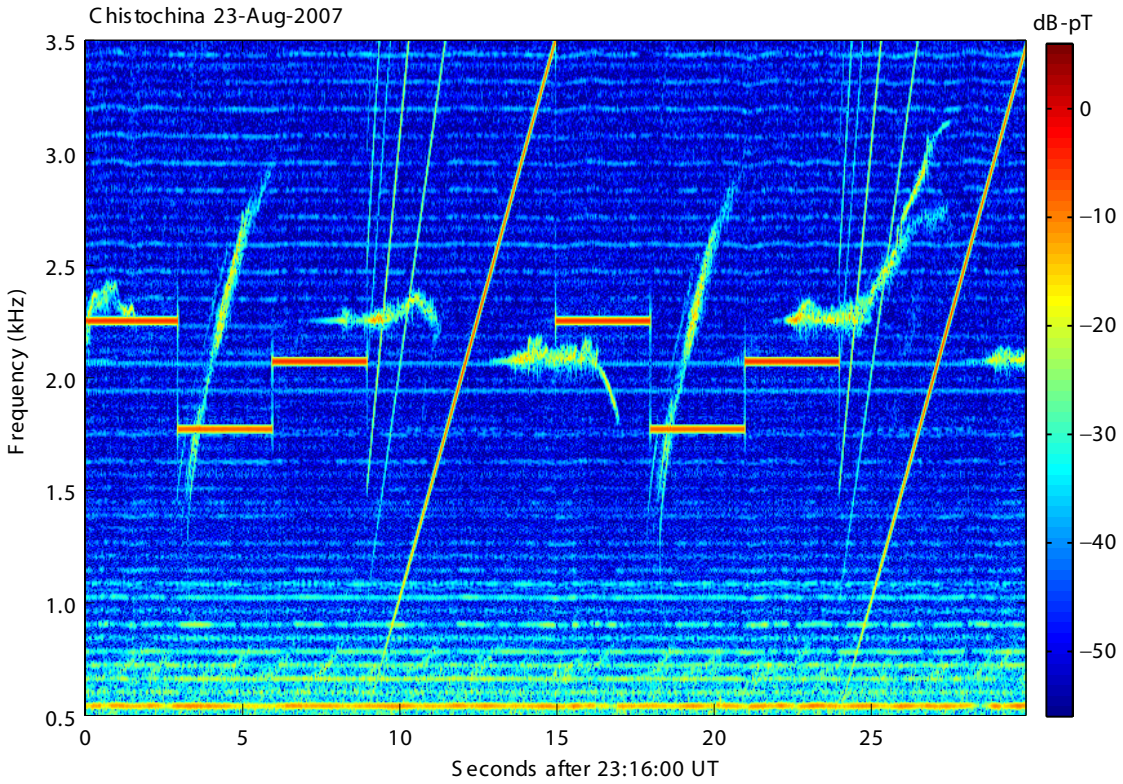

Figure 2.7: Two-hop echoes observed at Chistochina excited by frequency-time ramps and pulses over a ∼1.5 kHz band. The HAARP generated signals and 2-hop echoes exhibit particularly strong amplitudes.

satellite in the conjugate region as shown in Figure 2.8. Two aspects of the DEMETER observation are particularly noteworthy. Firstly, the echoes are observed continuously for 3 minutes during which the satellite traverses L-shells of 3.68 to 8.34, corresponding to a distance of several hundred kilometers. Secondly, the transmission involves alternate pulses at similar ELF/VLF frequencies but generated using two different HF frequencies of 3.25 and 9.0 MHz. This modulation format is accomplished by utilizing only half of the HF array for generation of each ELF/VLF frequency. Even though the echoes are observed over an expanse of many hundreds of kilometers and may have potentially traveled in several ducts spanning many L-shells, it is determined that the echoes all exhibit the same propagation delay consistent with

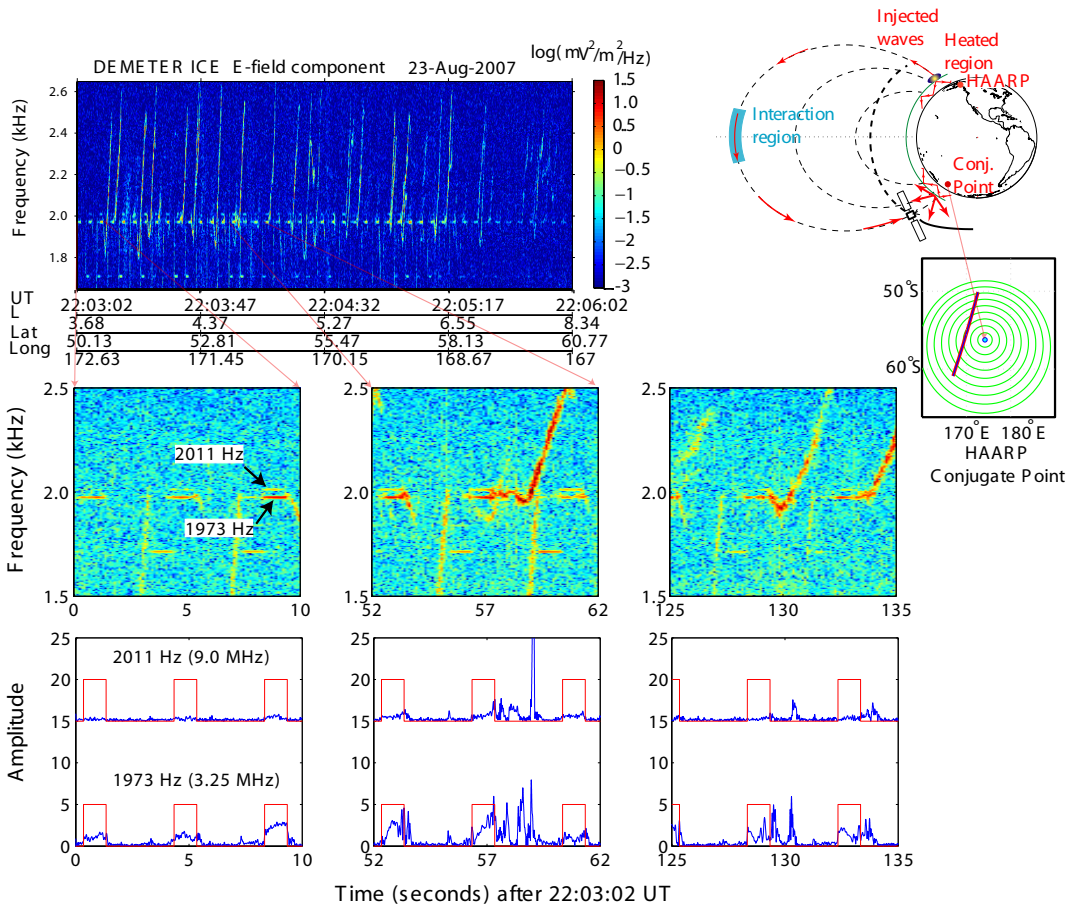

Figure 2.8: One-hop echoes observed on the DEMETER satellite during a pass over the HAARP conjugate point. The top-row from left to right contains a 3-minute spectrogram showing 1-hop echoes triggered by 1-second pulses and a cartoon showing the inferred propagation path of the signals to the satellite. The inset map shows the satellite footprint in the conjugate region with 100 km radius circles shown in red. The second row shows 10-second spectrograms from select times during the observation. The bottom row shows amplitude plots at the echo frequency in blue. The red trace is a superimposed timing signal to illustrate the constant propagation time of the echoes during the entire 3-minute record.

propagation along a single magnetospheric path. The long continuous observation is thus interpreted to result from propagation in a single duct followed by scattering from the lower boundary of the southern ionosphere to the satellite, yielding observation over an area much larger than any realistic duct dimension. This type of 'hybrid' propagation (i.e., ducted followed by non-ducted reflections) was previously reported in Siple experiments [*Bell et al.*, 1983], and is illustrated in the cartoon in the top right panel of Figure 2.8. Echoes excited by the 3.25 MHz carrier have higher amplitudes than echoes excited by the 9.0 MHz carrier. This result is in agreement with the amplitudes of HAARP signals as measured on the ground which show higher ELF/VLF amplitudes for lower HF carrier frequencies [*Moore*, 2007].

27 August 2007

On 27 August 2007, 1-hop echoes were observed on Buoy 2.0 during the 19:05 UT and 19:20 UT minutes. Figure 2.9 shows the echoes and associated emissions, which are triggered by 3-second pulses at frequencies of 1510 Hz, 1875 Hz, 2125 Hz, and 2375 Hz. No 2-hop echoes were observed in the northern hemisphere except for very faint triggered emissions that were identified to be induced by HAARP transmissions only after close examination of the Buoy 2.0 record. About an hour after the observations on Buoy 2.0, 2-hop echoes were observed on board DEMETER during a pass over Alaska a few hundred km east of the HAARP facility. No evidence of 2-hop echoes was observed at any ground stations in the northern hemisphere during the DEMETER pass. The 27 August 2007 observations are another example of the prevalence of 1-hop observations over 2-hop observations at ground stations. The observations aboard DEMETER on this day suggest that failure to penetrate the ionospheric boundary in the parent hemisphere is one of the reasons for this disparity.

30 August 2007

On 30 August 2007 several episodes of very faint and intermittent 2-hop echoes were observed at Chistochina before a full hour of much stronger echo observations later in the day. Two-hop echoes were first observed during 13:32-13:43 UT triggered by

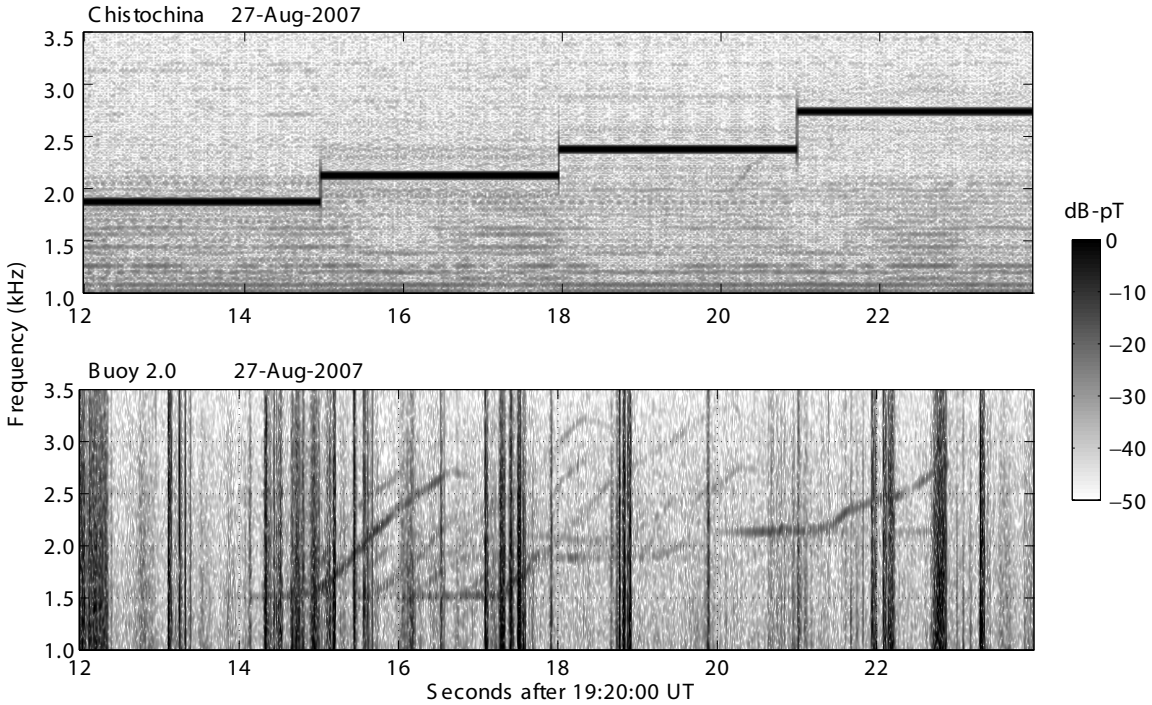

Figure 2.9: One-hop echoes observed on Buoy 2.0 (bottom panel) triggered by 3-second pulses at frequencies of 1510 Hz, 1875 Hz, 2125 Hz, and 2375 Hz. The HAARP transmissions can be seen in the top panel record from Chistochina. No 2-hop echoes are observed except for a faint triggered emission at 20.2 seconds. Both records are shown in gray scale to minimize the visual effect of the impulsive interference on the Buoy 2.0 record.

3-second 1875 Hz pulses. Unlike in previous cases, changing the format to focus transmissions on this frequency did not yield more echoes. Very faint 2-hop echoes were also observed at 14:02, 14:12, 15:30, 16:16, and 20:30−20:53 UT. At 20:13 UT 2-hop echoes were observed on DEMETER and starting at 22:00 strong 2-hop echoes were observed at Chistochina. The format was changed to one involving a new method of HF modulation, known as geometric modulation [*Cohen et al.*, 2008a], and 2-hop echoes continued to be observed for about an hour afterward. The effect of geometric modulation versus amplitude modulation on echo observations is discussed in Chapter 3.

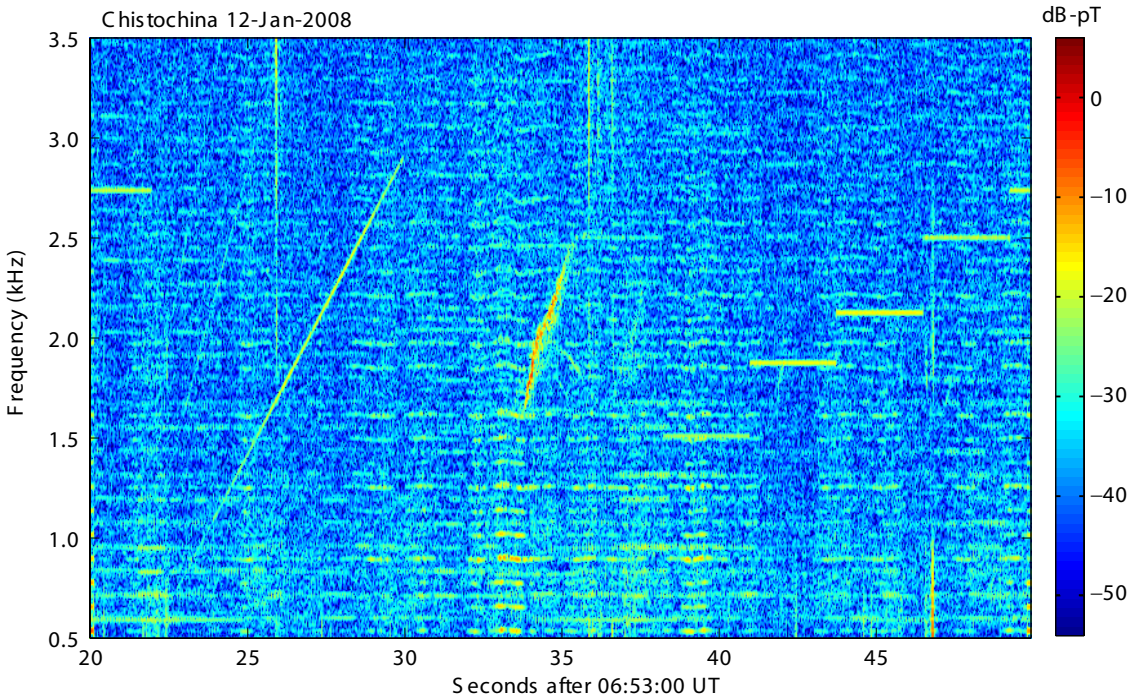

Figure 2.10: Spectrogram from Chistochina showing a 2-hop echo at ∼33−36 seconds excited by a 300 Hz/sec frequency-time ramp transmitted at 22-30 seconds in the record.

12 January 2008

On 12 January 2008 2-hop echoes excited by frequency-time ramps were observed at Chistochina. No echoes were observed from pulses in the same frequency range. Figure 2.10 shows an example observation from this day. It is interesting to contrast this case with the observations from 23 August 2007 shown in an identical format in Figure 2.7. On both days the transmission format includes frequency-time ramps and pulses in the 1−3 kHz band, but the amplitude of the HAARP signals observed on the ground is at least 10 dB higher on 23 August 2007. Despite this disparity and the fact that on 12 January 2008 2-hop echoes are observed to be excited only by frequency-time ramps, the amplitude of the 2-hop echo from 12 January 2008 is actually greater than that from 23 August 2007. An increased level of background noise from power line radiation is also visible in Figure 2.10.

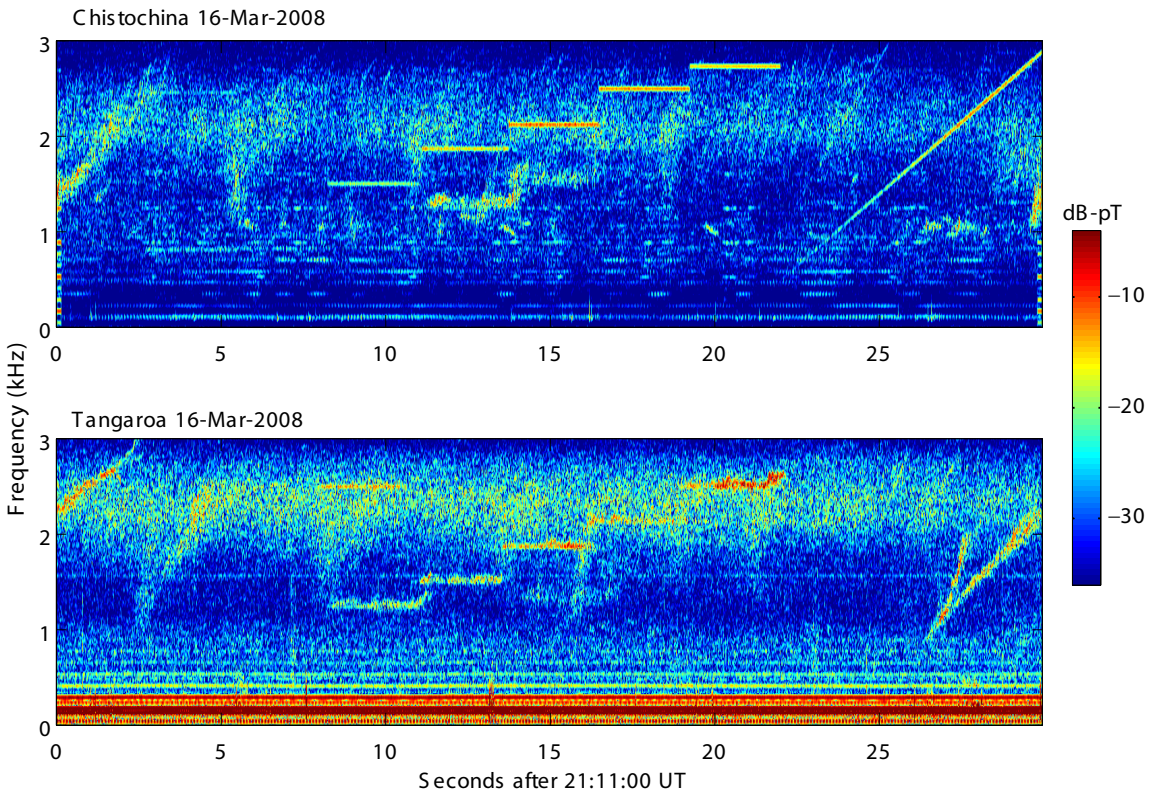

Figure 2.11: Spectrogram records from Chistochina (top panel) and *Tangaroa* (bottom panel) showing 1-hop echoes excited by all pulses and ramps in the 1−3 kHz band.

16 March 2008

For several days in March 2008 HAARP transmissions were carried out to coincide with the passage of *Tangaroa* through the conjugate region. For a period of almost 2 hours in 16 March 1-hop echoes were observed on *Tangaroa*. Figure 2.11 shows a case were the entire transmission format made up of ramps and pulses in the 1−3 kHz band is observed to trigger 1-hop echoes. Evidence of 2-hops echoes is also present at Chistochina (top panel of Figure 2.11) but these are more faint and not as easily identifiable.

9−11 May 2008

During May 2008, whistler mode echoes were observed on consecutive campaign days for the first time. Two-hop echoes were observed in varying intervals during the hours 15:00−22:00 and showed considerable variation including periods of enhanced echo amplitudes on time scales of 30−60 minutes. During several of the echo observations special formats were transmitted to investigate the effect of the beam orientation on the echo observations. Analysis of these results is presented in Chapter 3.

2.3 Summary of Observations

The cases mentioned above illustrate the variety and diversity of the HAARP induced whistler mode echo observations. Table 2.1 is a tabulation of all HAARP induced whistler mode echo observations through May 2008. Having outlined the general characteristics of the observations we proceed to analyze the factors governing and limiting observation occurrence in Chapter 3 and placing the observations in a theoretical context in Chapter 4.

Date	HF Power (MW)	HF (MHz)	Time (UT)	Time (MLT)	Location
20-Apr-04	0.96	3.25, 5.8	03:15-03:45	16:14-16:44	Chist., *Tang.*
27-Feb-07	3.56	3.25	6:20-6:37	19:19-19:36	*Tangaroa*
4-Mar-07	3.44	3.25	06:17-06:35	19:16-19:34	Chistochina
	3.44	3.25	06:25	19:24	Buoy 1.5
	3.44	3.25	06:20	19:19	Buoy 2.0
23-Aug-07	1.80	3.25, 9.5	22:03-22:06	11:02-11:05	DEMETER (C)
	3.58	3.25	23:05-23:21	12:04-12:20	Chistochina
27-Aug-07	3.6	3.25	19:05, 19:20	08:04, 08:19	Buoy 2.0
30-Aug-07	3.58	3.25	13:32-13:43	02:31-02:42	Chistochina
	3.58	3.25	14:02, 14:12	03:01, 03:11	Chistochina
	3.58	3.25	15:30, 16:16	04:29, 05:15	Chistochina
	1.8	3.25, 9.5	20:12-20:14	09:11-09:13	DEMETER (O)
	3.58	3.25	20:30-20:53	09:29-09:52	Chistochina
	3.58	3.25	22:00-23:00	10:59-11:59	Chistochina
12-Jan-08	3.6	2.75	06:51-06:55	19:50-19:54	Chistochina
	3.6	2.75	10:02-10:17	23:01-23:16	Chistochina
31-Jan-08	3.6	2.75	13:21-13:38	02:20-02:37	Chistochina
16-Mar-08	3.6	2.75	20:30-20:31	09:29-09:30	*Tangaroa*
	3.6	2.75	20:50-21:26	09:49-10:25	Chist., *Tang.*
	3.6	2.75	21:36-22:06	10:35-11:05	*Tangaroa*
	3.6	2.75	22:13-22:18	11:12-11:17	*Tangaroa*
	3.6	2.75	22:43-22:47	11:42-11:46	*Tangaroa*
9-May-08	3.48	2.75	15:06-15:52	04:05-04:51	Chistochina
10-May-08	3.58	2.75	17:10-18:03	06:09-07:02	Chistochina
	3.58	2.75	20:28-20:38	9:27-9:37	Chistochina
	3.58	2.75	20:54-21:18	09:53-10:17	Chistochina
11-May-08	3.6	2.75	15:07-15:15	04:06-04:14	Chistochina
	3.6	2.75	15:28	04:27	Chistochina
	3.6	2.75	15:41-15:44	04:40-04:43	Chistochina
	3.6	2.75	16:30-17:17	05:29-06:16	Chistochina
	3.6	2.75	17:53-17:55	06:52-06:54	Chistochina
	3.6	2.75	18:02-18:06	07:01-07:05	Chistochina

Table 2.1: Summary of observation occurrence. Observations aboard DEMETER are designated (C) for passes in the conjugate region and (O) for passes over the HAARP facility.

Chapter 3

Occurrence Statistics and Dependencies

The observations presented in Chapter 2 demonstrate that the HAARP facility can be effectively used to excite whistler mode echoes. Table 2.1 lists the specific days, hours, and durations of echo observations. Although the list of observations is substantial (and continuously growing), it should be assessed in the context of total experiment runs. On almost all days of the experiment, ELF/VLF wave injection transmissions were conducted for at least 8 hours and on days corresponding to ship-borne measurements in the conjugate region transmissions were often carried out continuously for 24 hours. It is thus apparent that observations of HAARP induced whistler mode echoes are ephemeral and only occur under special conditions. Investigating the occurrence of HAARP induced echo observations and determining their dependencies is important not only for understanding the physics of the magnetospheric wave-particle interaction but also for optimal utilization of the vast resources required to run the HAARP facility. In this context, it is important to note that observation of whistler mode echoes requires the juxtaposition of three general conditions. High frequency modulation of existent auroral electrojet currents must first lead to generation of ELF/VLF waves of significant amplitude. The generated ELF/VLF energy must subsequently be coupled into an existing duct to allow propagation to the interaction region near the geomagnetic equator. Finally, a hot plasma distribution favorable for

growth is necessary to amplify the waves. In this chapter we investigate the conditions surrounding the echo observations and assess the influence of various factors on the excitation of whistler mode echoes with the HAARP facility.

3.1 HAARP ELF/VLF Generation Strength

ELF/VLF waves generated using HF heating regularly show significant variations in amplitude as observed on the ground that result from dynamic changes of the electrojet currents and the ionospheric D-region density profile. Often 10−20 dB variations in amplitude can be observed on time scales of hours and minutes [*Rietveld et al.*, 1987; *Cohen et al.*, 2008b]. Figure 3.1 shows the HAARP generated signal amplitude, as observed on the ground at Chistochina, for all days of the wave-injection experiments since the facility upgrade in 2007. The amplitude variation is expressed using range bars showing the 20th percentile, median and 95th percentile of the observed signals. The red stars in Figure 3.1 show the HAARP signal amplitudes for cases which 1-hop or 2-hop echoes are observed (the 20 April 2004 observation is also included). It is apparent that, in general, echo observations do not correspond to the strongest generated signals as observed on the ground. In fact there are times, such as those on 20 April 2004, when very weak signals as measured on the ground are observed to excite echoes and trigger emissions.

We next investigate the effect of generated signal amplitude on the time scale of a single period of echo observations. The observations of 20 April 2004 and 27 February 2007 are particularly well suited for such an examination since 1-hop echoes were observed to be triggered for ∼30 minutes during which time both the HAARP signals observed on the ground and echo amplitudes exhibited considerable variation. The top panel in Figure 3.2 shows the amplitude of the ELF/VLF magnetic field components recorded at Chistochina on 27 February 2007 during the observation of 1-hop echoes in the conjugate region. The middle panel shows the deviations from an hourly mean of three components of the Earth's magnetic field recorded with a magnetometer at the HAARP site. The magnetometer readings provide a measure of the electrojet strength and direction. The bottom panel shows the amplitude

of 1-hop echoes observed on *Tangaroa*, where red bars indicate that multiple parts the transmission format yielded echoes. The two maxima in the echo amplitude at minutes 06:25 and 06:32 UT show good correspondence with amplitudes of HAARP signals observed locally at Chistochina, which themselves exhibit strong correlation with the north-south horizontal (H) component of the geomagnetic field. It is worth noting that in general the relationship between magnetometer readings and HAARP ELF/VLF radiation is not straightforward and the close correlation seen here is not always observed [*Cohen et al.*, 2008b]. The magnetometer readings suggest that the increased HAARP signal strength is due to an increase in electrojet intensity rather than a change in direction. The correspondence between echo observations and HAARP signal amplitude ends at 06:45 UT, however, when the HAARP ELF/VLF intensity and the electrojet intensity (north-south horizontal component) exhibit a third maximum of equal amplitude during which no further echoes are observed on the ship. It seems that although the strength of HAARP ELF/VLF radiation clearly plays a role in echo observations, other processes are also at work.

The observations from 20 April 2004 are shown in Figure 3.3 and point toward a less definitive correspondence. The three panels in Figure 3.3 have the same layout as in Figure 3.2 in that HAARP signal strength, magnetometer reading, and 1-hop echo amplitude are shown respectively in the top, middle, and bottom panels. The 20 April 2004 observations differ from those of February 2007 in that the HF frequency was changed from 3.5 MHz to 5.8 MHz during the echo observation period. On this day we see that the observed 1-hop echo amplitudes show almost no correspondence to the HARRP signal amplitude. Most surprising is the brief enhancement in echo amplitude at 03:31 UT, even though HAARP generation as observed on the ground has dropped significantly due to the higher HF frequency employed. The magnetometer data show correspondence to the HAARP signal amplitude but the change in HF frequency is seen to have the dominant effect on observed signal amplitudes. We thus conclude that the strength of ELF/VLF radiation by the HAARP ionospheric antenna (as observed on the ground) is not the primary factor affecting observations of whistler mode echoes, and the relationship therein is at best secondary as shown in the 27 February 2007 case.

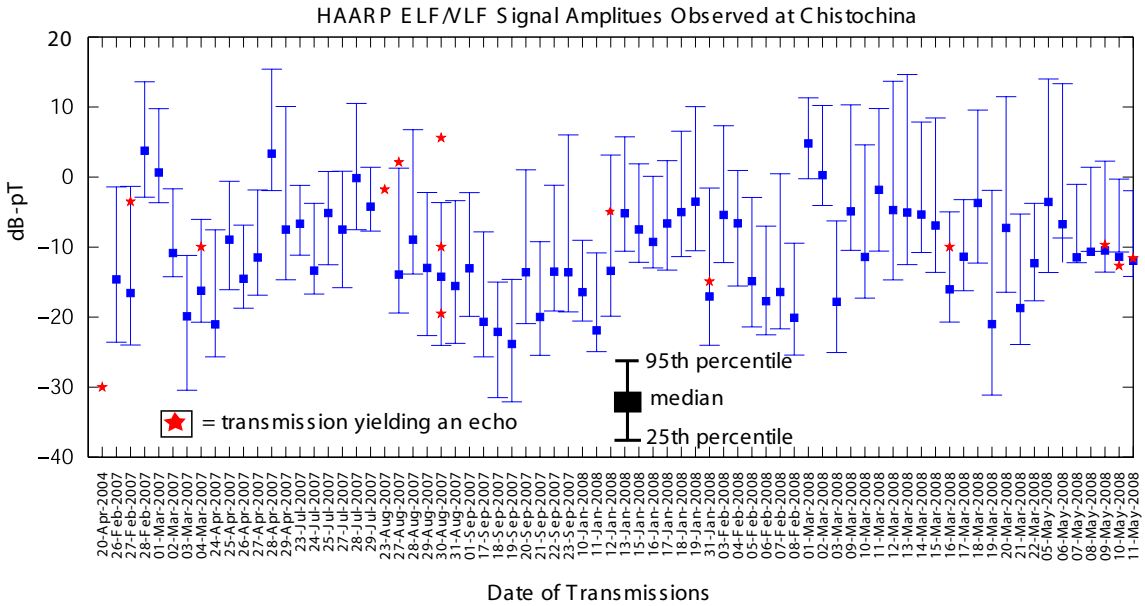

Figure 3.1: Amplitude variation of HAARP generated ELF/VLF signals for all days of wave injection experiments from HAARP facility upgrade through May 2008. Red stars indicate amplitudes of signals that yielded 1-hop or 2-hop echo observations.

Certain qualifications are in order with respect to the conclusion above. Although the relationship between ELF/VLF power radiated into space and that radiated into the Earth-ionosphere waveguide is a topic of active research [*Platino et al.*, 2006], it is likely that the radiation observed on the ground is proportional to the same currents that radiate into space. This expectation may be particularly true for observations made at Chistochina, which is located only 36 km away from the HAARP facility. Since this distance is much shorter than a wavelength, waveguide excitation effects do not play a strong role. This argument also applies across different HF carrier frequencies. A higher HF frequency is known to yield weaker ELF/VLF generation [*Stubbe et al.*, 1982] and has also been theoretically predicted to modulate currents at higher altitudes. A decrease in amplitude as observed on the ground with increasing HF frequency has been verified with experiments but there has been no evidence that an electrojet dipole antenna generated with a higher HF frequency is more efficient in injecting waves into space. In the 20 April 2004 observations, we thus do not attribute

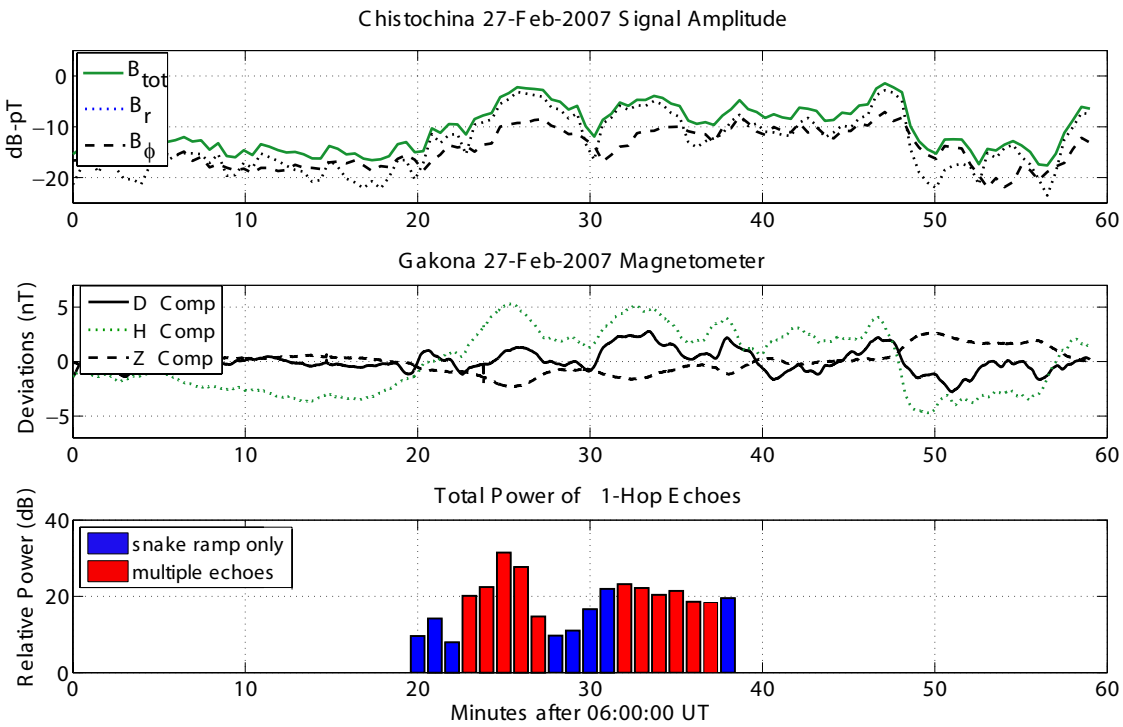

Figure 3.2: Top panel shows local HAARP ELF/VLF signal strength at Chistochina as observed in the amplitude of the radial magnetic field (B_r), the azimuthal magnetic field (B_ϕ), and the total magnetic field (B_{tot}). Middle panel shows variations of the geomagnetic field from a magnetometer at the HAARP site with positive northward component (H), positive eastward component (D), and positive downward component (Z). Bottom panel shows relative integrated power of echoes observed on *Tangaroa*. All three panels show maxima at 06:26 and 06:35, although no echoes are observed during the third maximum in signal power and electrojet strength at 06:46.

the enhancement of 1-hop echo observations after the change to the higher, 5.8 MHz, HF frequency to result from an elevated ELF/VLF dipole. The observations of 1-hop echoes on board DEMETER from 23 August 2007 (see Figure 2.8) also support the notion that higher HF frequencies generate weaker signals and trigger weaker echoes. Our conclusion about the lack of strong correlation between HAARP generated signal amplitude and observations of whistler mode echoes is not meant to imply that wave amplitude is not an important parameter in the magnetospheric wave-particle interaction. On the contrary, both theoretical treatments and observations discussed

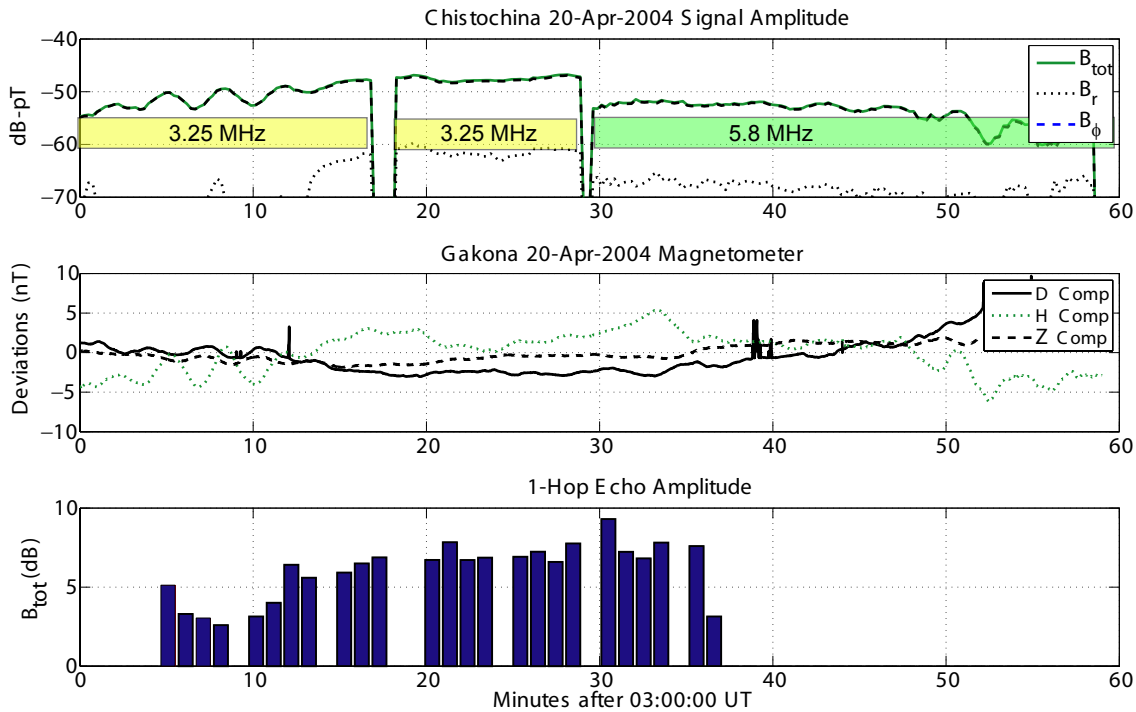

Figure 3.3: HAARP signal amplitude, magnetometer reading and 1-hop echo amplitude for 20 April 2004 observations presented in same format as Figure 3.2

in Chapter 4 underline the importance of the input wave amplitude in driving the hot plasma instability. It is worth noting that a non-linear input amplitude threshold was observed in the Siple Station experiments [*Helliwell et al.*, 1980a]. However, in the context of the conduct of the experiment at the highest operator level, it is clear that conditions of maximum observed HAARP ELF/VLF generation do not necessarily increase the probability of observing triggering of whistler mode echoes.

3.2 Determination of Magnetospheric Path

For whistler mode waves propagating in the magnetosphere, the plasma medium is highly dispersive, meaning that propagation velocity is a strong function of frequency.

It is possible to use the observed frequency-time dispersion of a signal to infer the characteristics of its magnetospheric propagation path. This approach has been used with great success for probing the magnetosphere [*Carpenter*, 1963] and has yielded the development of a body of techniques for analyzing whistlers generated by broadband radiation from terrestrial lightning [*Sazhin et al.*, 1992]. If whistler mode echoes are observed to be triggered by signals with a bandwidth spanning at least 1 kHz, the magnetospheric propagation path and the associated equatorial cold plasma density can readily be determined using these whistler analysis techniques.

In the HAARP wave injection experiments, the signals that fit this criteria are the time frequency ramps usually spanning the band of 500 Hz to 3.5 kHz. For a ducted path, assuming parallel propagation, the propagation time t of a 1-hop signal as a function of frequency f can be expressed using Equation (1.3) from *Park* [1972]

$$t(f) = \frac{1}{2c}\int_{mag} \frac{f_p}{f^{1/2} f_c^{1/2}\left(1 - \frac{f}{f_H}\right)^{3/2}} ds + \frac{1}{2c}\int_{iono} \frac{f_p}{f^{1/2} f_c^{1/2}\left(1 - \frac{f}{f_H}\right)^{3/2}} ds \qquad (3.1)$$

where $f_p \equiv \frac{1}{2\pi}\sqrt{\frac{N_e q^2}{m_e \epsilon_0}}$ is the electron plasma frequency and $f_c \equiv \frac{qB}{2\pi m_e}$ is the electron cyclotron frequency. The two integrals are to be evaluated along the magnetospheric and ionospheric portions of a ducted path with the transition taken at 1000 km altitude. Utilization of Equation (3.1) requires specification of f_p and f_c along the integration path. Since a ducted path is largely confined to the geometry of a geomagnetic field line, for a dipole field f_c can easily be expressed as a function of latitude ϕ, parametrized with the McIlwain L parameter:

$$f_c(L, \phi) = 8.736 \times 10^5 \frac{\sqrt{1 + 3\sin^2\phi}}{L^3 \cos^6\phi} \qquad \text{[Hz]} \qquad (3.2)$$

Specification of f_p requires knowledge of the cold electron density N_e along the ducted path. In the ionosphere, the cold plasma density can be effectively modeled using a

simple α-Chapman layer [*Park*, 1972] described as a function of altitude h by

$$N_e = N_{\text{imax}} \ \exp\left\{\frac{1}{2}\left[1 - z - \exp\left(-z\right)\right]\right\} \tag{3.3}$$

$$z = \frac{h - h_0}{H}$$

where N_{imax} is the maximum ionospheric electron density at altitude h_0 and H is the scale height. Typical values for N_{imax}, h_0, and H are 10^5 cm^{-3}, 300 km, and 75 km, respectively. For the cold electron distribution along geomagnetic field lines in the magnetosphere, an appropriate formulation is the diffusive equilibrium model developed by *Angerami and Thomas* [1964]. The magnetospheric electron density is given by

$$N_e = N_{\text{eq}} \sqrt{\frac{\sum_i \zeta_{i1} \exp\left(-\dfrac{z}{H_i}\right)}{\sum_i \zeta_{i1} \exp\left(-\dfrac{z_{\text{eq}}}{H_i}\right)}} \tag{3.4}$$

$$z = r_1 - \frac{r_1^2}{r} - \frac{\Omega^2}{2g_1}\left(r^2 \cos^2\phi - r_1^2 \cos^2\phi_1\right) \tag{3.5}$$

$$H_i = \frac{k_{\text{B}} T}{m_i g_1} \tag{3.6}$$

where

ζ = fractional abundance of ionic species

r = geocentric distance

Ω = angular rotational speed of the Earth

g = acceleration of gravity

k_B = Boltzman's constant

T = temperature

m = mass

The subscript i refers to the ith ionic species (O^+, He^+, and H^+), the subscript 1 refers to the reference level of 1000 km, and the subscript eq refers to the magnetic equator. Equations (3.4) through (3.6) show that the electron density depends on the temperature and ion content at the reference level as well as the geometry of the field

Model	Electron Temp.(K)	Composition at 1000 km O^+	H^+	He^+
DE-1	1600	90%	8%	2%
DE-2	3200	90%	8%	2%
DE-3	1600	50%	40%	10%
DE-4	800	50%	40%	10%

Table 3.1: Parameters of standard diffusive equilibrium models

line. Table 3.1 shows four standard combinations of ion content and temperature.

Using a model combination from Table 3.1, it is possible to completely evaluate the frequency dependent integrals in Equation (3.1) for chosen values of L, N_{eq}, and the three ionospheric parameters (N_{imax}, h_0, H). Determining the magnetospheric path and associated cold plasma density for an observed dispersed echo thus involves finding values of the five parameters (N_{eq} L, N_{imax}, h_0, H) that yield values of $t(f)$ that most closely match the observations. Since the magnetospheric portion of the propagation path accounts for about 90% of the observed dispersion [*Park*, 1972], the evaluation of $t(f)$ is most sensitive to L and N_{eq}. To determine the parameters for the propagation paths traversed by HAARP triggered echoes, the ionospheric parameters in both hemispheres are estimated using data from an ionosonde located at the HAARP facility. A two parameter numerical optimization routine is run to subsequently find the most likely values of the magnetospheric parameters L and N_{eq}. For the case of 2-hop echo observations, the optimization algorithm involves two consecutive evaluations of the integrals in Equation (3.1).

As mentioned above, magnetospheric path determination techniques are only useful for echoes triggered by signals of at least ∼1 kHz bandwidth. Figure 3.4 shows 2-hop echoes observed at Chistochina on 23 August 2007 triggered by a 500 Hz/sec frequency-time ramp spanning 500 Hz to 3.5 kHz. The frequency-time signature of the transmitted ramp is shown in the figure as a yellow dash-dot reference line as the actual transmission took place ∼6.5 seconds before the observation of the 2-hop echoes shown to begin at 17.8 seconds in the record. The effect of dispersion can clearly be seen in the change in frequency-time shape of the 2-hop echoes with respect to the

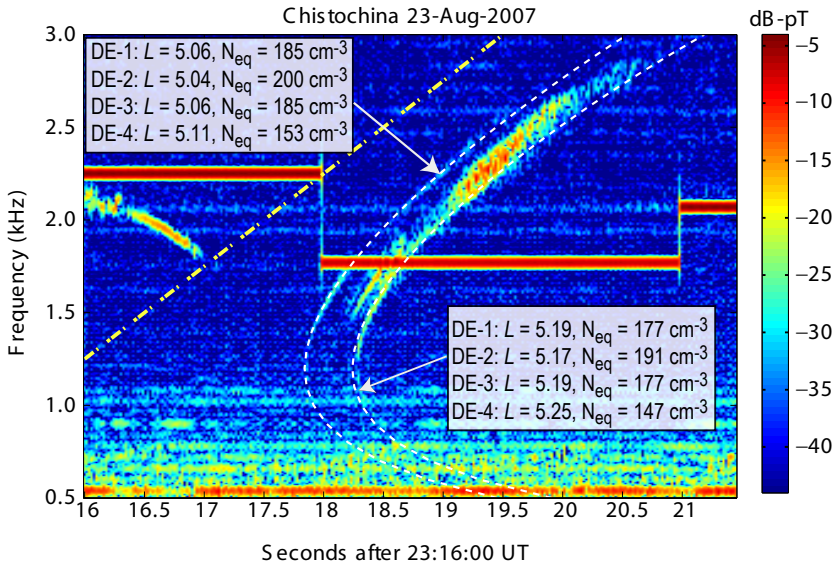

Figure 3.4: Example of observed dispersion of 2-hop echoes triggered by a frequency-time ramp and fitted curves based on magnetospheric plasma models.

original ramp. Multiple echoes propagating along distinct magnetospheric paths are also apparent. The white dotted lines in Figure 3.4 show the simulated dispersion using the four models described in Table 3.1 and L and N_{eq} input values as shown in the figure. The ionospheric parameters, N_{imax}, h_0, H, are chosen as $10^{4.5}$ cm^{-3}, 225 km, and 50 km, respectively, based on available ionosonde data. The two simulated dispersion curves bound the fastest and slowest echo propagation paths and match the shape of the observed echoes. Although there is some variation in results between the four dispersive equilibrium models, for each there is a consistent span of $\sim$0.13 L and $\sim$8 cm^{-3} between the bounding paths. The similarity between the DE-1 and DE-3 models suggest the dominant influence of electron temperature over ion composition. The results shown in Figure 3.4 are consistent for the full 16 minutes of observation of 2-hop echoes at Chistochina on 23 August 2007. The $\sim$0.13 L spread in the magnetospheric paths corresponds to $\sim$900 km at the geomagnetic equator but only $\sim$50 km at an altitude of 80$-$100 km. Thus, while the magnetospheric wave particle interactions are independent, the path separation in the ionosphere is only on

the scale of the HF heated region. Although the center of the HAARP induced (∼85 km altitude) ELF/VLF dipole is located at $L \simeq 4.94$, the ∼35 km wide HF heated region is encompassed by L-shells of $5.06 < L < 5.17$ when projected to an altitude of 300 km using an IGRF model of the geomagnetic field. Assuming that HAARP ELF/VLF signals couple into ducts at ∼300 km in the ionospheric F-region, the L-shell propagation path range determined from the observations matches the heated region and points to signals being injected into the magnetosphere directly above the heating facility. This conclusion is further supported by the simultaneous observation of a new phenomena of echo-heating cross modulation discussed in Chapter 5. It is worth noting that the issue of duct geometry and energy confinement continues to be a topic of active research [*Streltsov*, 2007; *Streltsov et al.*, 2006]. While it is convenient to assume extension of ducted propagation deep into the lower ionosphere, *Strangeways et al.* [1982] presents evidence of energy coupling into and out of ducts at altitudes of ∼1000 km. In this context, the assertion that HAARP signals couple into ducts at 300 km altitude is reasonable.

Figure 3.5 shows the magnetospheric path and associated cold plasma density results for all observations for which such a determination was possible. The path results are clustered around the L-shells corresponding to the dimensions of the heated region projected to a 300 km altitude as shown in the figure. It thus appears that the HAARP facility is most effective in injecting waves into the magnetosphere directly over the HF array as opposed to first exciting propagating modes in the Earth ionosphere waveguide which then couple into the magnetosphere at locations away from the facility. This result is in agreement with recent satellite measurements of HAARP signal injection into the magnetosphere showing a column of high amplitude upward radiation concentrated in a region of ∼30 km diameter directly above the heater [*Piddyachiy et al.*, 2008]. A recent theoretical model of ELF/VLF radiation from modulated ionospheric currents also shows a similar overhead columnar excitation [*Lehtinen and Inan*, 2008]. In the context of echo observation occurrence it thus seems that echoes are most commonly observed if magnetospheric ducts are available directly above the heating facility.

Included in Figure 3.5 are equatorial density profiles corresponding to 'quiet' and

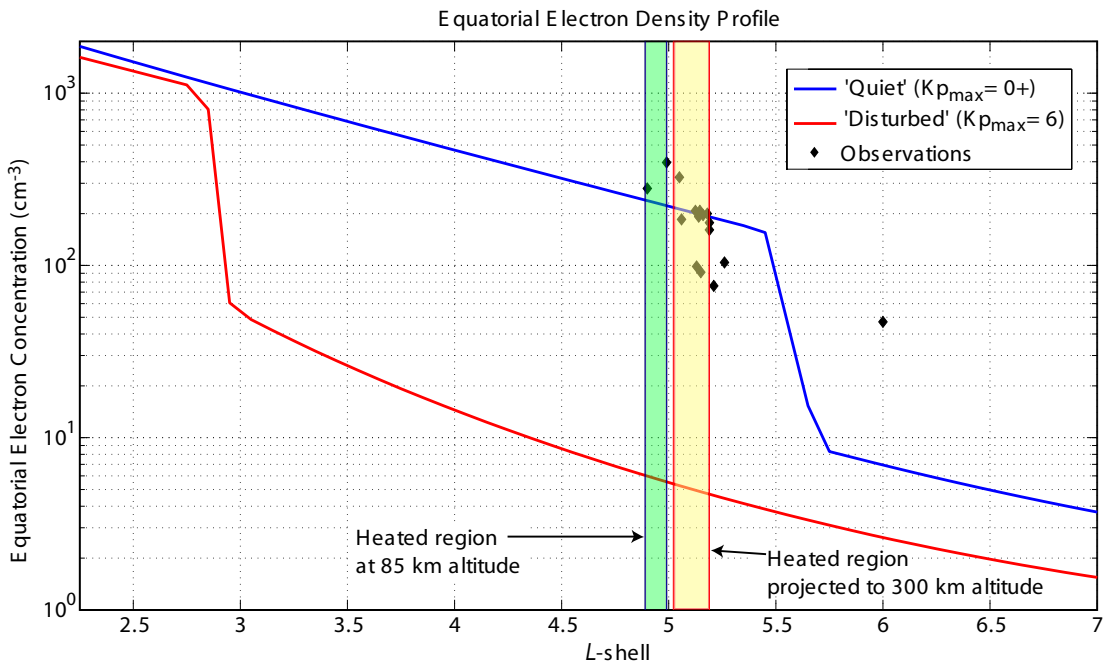

Figure 3.5: Magnetospheric path and equatorial cold plasma density determinations from observed echoes plotted with equatorial density profiles typical for quiet and disturbed magnetospheric conditions. The L-shells corresponding to the HAARP heated region at 85 km and projected to 300 km above the HAARP HF array are also shown.

'disturbed' geomagnetic conditions derived from geomagnetic Kp indices using the empirically derived formulations of *Carpenter and Anderson* [1992]. The quiet profile shown in blue corresponds to a $Kp_{\max}$ of 0+ while the disturbed profile shown in red corresponds to $Kp_{\max}$ of 6. $Kp_{\max}$ is defined by *Carpenter and Anderson* [1992] as the highest Kp value recorded in the preceding 24 hours. The equatorial cold plasma density values derived from the echo observations are in close agreement with the quiet profile corresponding to locations clearly inside the plasmapause. Consequently, the location of the plasmapause with respect to the HAARP facility may be one of the best metrics for assessing the likelihood of observing excited magnetospheric echoes.

3.3 Modulation Technique and Beam Geometry

In the course of the HAARP wave injection experiments different methods of modulating the electrojet were explored in addition to conventional amplitude modulation (AM). On 30 August 2007 whistler mode echoes were observed to be excited by a transmission that included the same ELF/VLF format generated using four different types of modulation techniques. The four different modulation techniques are shown schematically in the top row of Figure 3.6. The first technique is the conventional AM approach where the HF beam is cycled ON and OFF at the desired ELF/VLF frequency with a 50% HF duty cycle. The line sweep and circle sweep techniques involve leaving the HF beam ON and achieving modulation of the electrojet currents by moving the beam at the desired ELF/VLF frequency along either a line or circle pattern in the sky. Since these techniques achieve modulation via the changing position of the beam they are appropriately called 'geometric modulation' [*Cohen et al.*, 2008a]. The final technique is known as 'beam painting' and creates an effectively larger beam by quickly scanning the beam in a larger area and taking advantage of the fact that electron cooling rates are slower than heating rates. The beam painting technique is essentially still an AM approach since the quick scanning is followed by HF OFF for half of the modulation period. Because of the 100% duty cycle of the geometric modulation techniques, they involve greater deposition of HF power. *Cohen et al.* [2008a] report that geometric modulation can yield enhancement of ELF/VLF amplitudes of up to ∼11 dB and allows for directional launching of ELF/VLF waves. The beam painting and circle sweep techniques both involve tilting the HF beam to the maximum offset of 15° from zenith. Consequently, the beam paint and circle sweep techniques involve a considerably larger illumination area than the AM and line sweep techniques.

The transmission format comprised of the four techniques was observed to excite echoes for an hour on 30 August 2007. The spectrogram in Figure 3.6 shows a minute long record from Chistochina where 2-hop echoes are observed to be triggered by 2 kHz pulses generated by the line sweep technique and circle sweep technique (but not the other techniques). The bottom panel in Figure 3.6 shows the amplitude of

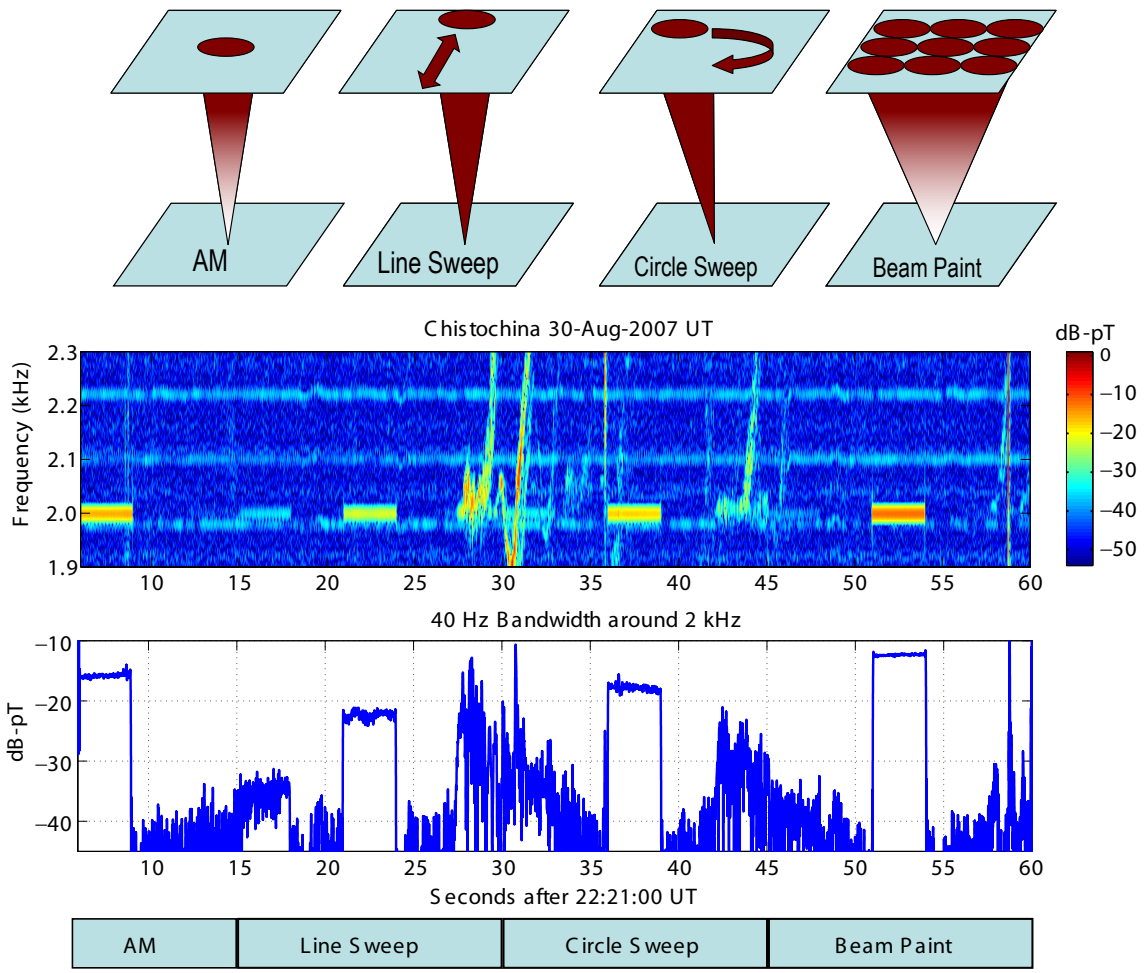

Figure 3.6: Experiment setup for transmission using four different HF modulation techniques illustrated in the top row. The middle and bottom panels show a sample result where 2-hop echoes are triggered by 2 kHz pulses generated using the line sweep and circle sweep techniques. The amplitudes of the signals at 2 kHz can be seen in the bottom panel.

the 2 kHz signals in a 40 Hz bandwidth. Even though the beam paint and AM techniques yield higher amplitude signals, they do not excite magnetospheric echoes. The record shown in Figure 3.6 is not representative of all cases since over the hour of echo observations different techniques triggered echoes in different minutes. Figure 3.7 shows scatter plots for echoes observed to be triggered by each of the four modulation techniques. The x-axis shows the observed generated signal amplitude and the y-axis

shows maximum echo amplitude. The circle sweep and beam paint techniques yield the strongest echoes even for weak signals as observed at Chistochina. The similarity of the beam paint and circle sweep results in Figure 3.7 suggest that the effective beam area is more important than the generated signal amplitude in determining excitation of magnetospheric echoes.

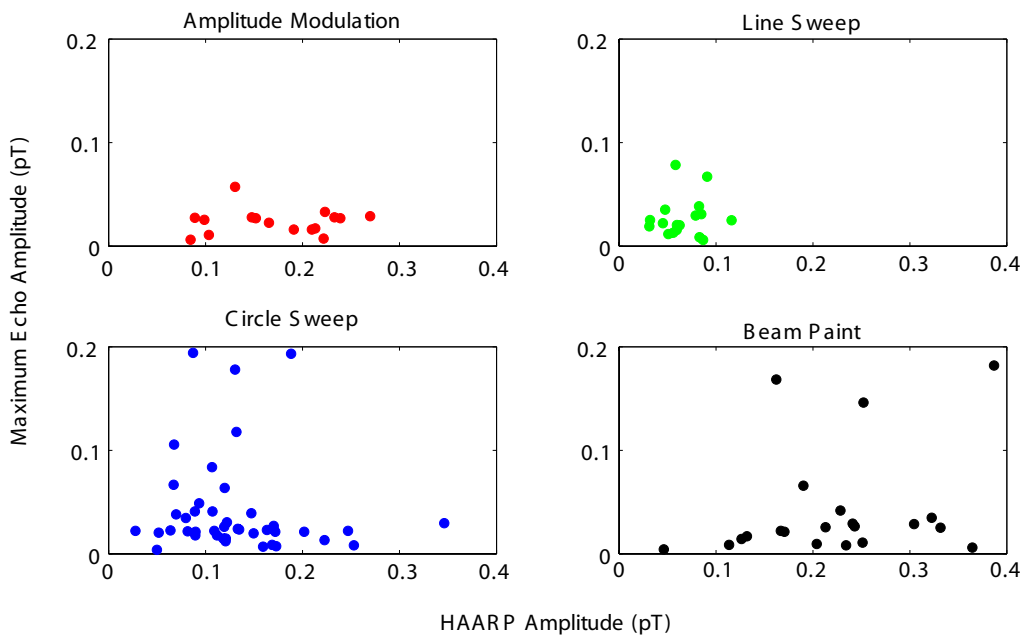

Figure 3.7: Scatter plots showing maximum echo amplitude versus HAARP signal amplitude observed on the ground for each of the modulation techniques described in Figure 3.6.

Since the effective beam size appears to be an important factor in determining excitations of observable echoes, a special transmission format was designed to investigate spatial effects of the beam position. In this format the same frequencies are generated using the AM technique but by aiming the beam to 4 different positions in the sky. The dwell time in each position is only 15 seconds, shorter than the typical time scales of changing echo response. Figure 3.8 shows the arrangement of the 4 different beam positions and also a spectrogram showing the triggering of 2-hop echoes by 1.525 kHz pulses observed at Chistochina on 10 May 2008. The format was transmitted from 17:27−18:17 UT and 2-hop echoes were observed to be excited by

transmissions from at least one of the beam positions from 17:27−18:00 UT. In Figure 3.8 2-hop echoes are observed to be triggered by the central (gray) and southeast (red) beam positions only. The beam position that is most favorable for triggering echoes exhibited variation during the half hour of echo observations. Figure 3.9 shows the number of echoes triggered by each position during consecutive 5 minute periods. The echoes can be seen to be initially preferably triggered by the central and southeast positions, and subsequently almost equally by all positions during 17:36−17:40 UT. During the 17:46−17:50 UT time segment the southeast position is again favorable, followed by a 10 minute period of dominance by the northeast position before the echoes cease to be observed after 18:00 UT.

Since it has already been demonstrated that the ELF/VLF signal strength (as observed on the ground) is not a dominant factor in excitation of echoes, the changing preferential excitation of echoes as a function of beam position points to a sensitivity to coupling energy into available ducts. Unfortunately, the results in Figure 3.9 cannot be reduced to an over-simplified scenario of a duct being located directly over a given beam position and drifting between positions accordingly. Although *Andrews et al.* [1978] and more recently *Gołkowski and Inan* [2008] have shown evidence of observable duct drift on similar time scales, it must be remembered that HAARP ELF/VLF signals most likely couple into ducts several hundred kilometers above the heated area. Propagation through the ionosphere to the duct entry point is strongly affected by the ionospheric medium. The upper ionosphere is known to host many irregularities [*Dyson*, 1969; *Clark and Raitt*, 1976; *Gross and Muldrew*, 1984; *Sonwalkar and Harikumar*, 2000] and the HAARP heater itself is known to generate irregularities during its operation [*Djuth et al.*, 2006], so the mapping of beam positions that excite echoes to fixed duct entry points is not straightforward. Nonetheless, both the results from various beam positions/orientations and the magnetospheric path determination results discussed above suggest that availability and coupling into ducts are the primary factors controlling the occurrence of whistler mode echo observations.

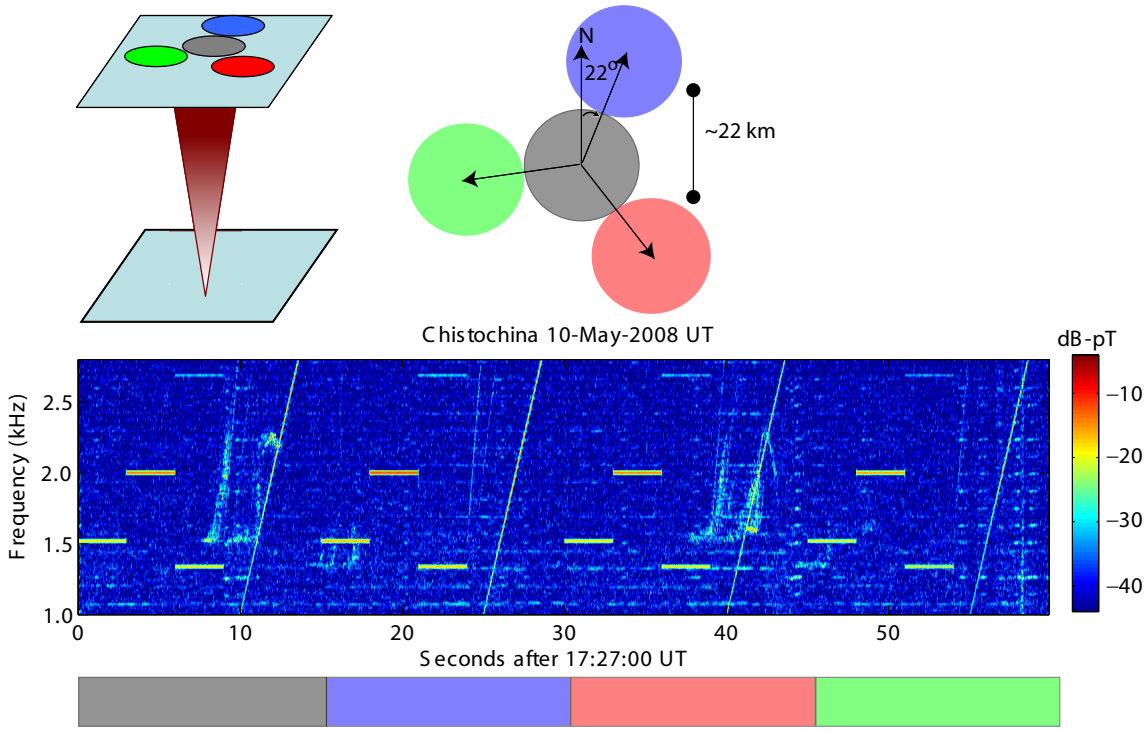

Figure 3.8: The schematics in the top row show the experiment setup for investigating the effect of HF beam position on triggering of echoes. The HF beam is directed to four adjacent overhead positions marked in gray, blue, red and green colors. The dwell time in each position is 15 seconds and signals are generated using AM modulation. The spectrogram shows a sample result showing 2-hop echoes observed at Chistochina triggered by the gray and red positions.

3.4 Comparison with Siple Station Results

To shed further light on the conditions that are conducive to HAARP induced whistler mode echo observation, we compare the HAARP observations with statistics from the Siple Station experiments. *Carpenter and Bao* [1983] performed an occurrence study of echoes triggered by the Siple Transmitter and in certain respects the HAARP echo observations are compatible with their findings. *Carpenter and Bao* [1983] found that Siple triggered echoes were preferentially observed under quiet magnetospheric conditions and primarily inside the plasmapause (see also *Carpenter and Miller* [1983]),

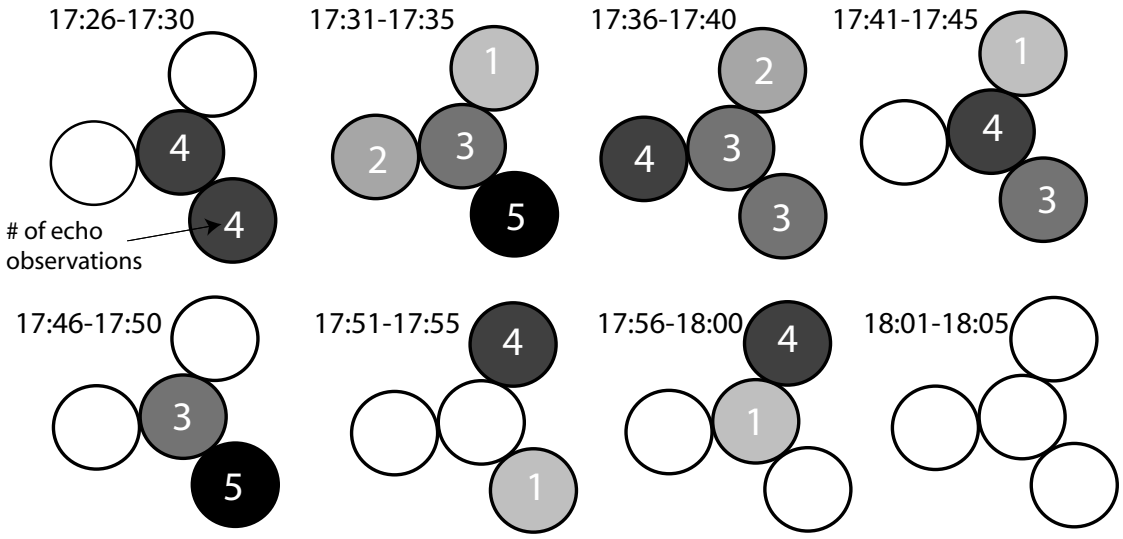

Figure 3.9: Number of echo observations triggered by ELF/VLF signals generated in each overhead beam position as described in Figure 3.8. At different times different beam positions are favorable to exciting echoes.

in excellent agreement with result from HAARP shown in Figure 3.5. At this point, it is difficult to say whether propagation inside the plasmapause is favorable for magnetospheric amplification because of the higher cold plasma densities or the presence of guiding structures. *Carpenter and Bao* [1983] also identify a diurnal preference for echo observations during the hours 4:00−10:00 MLT and a secondary peak at ∼19:00 MLT. The modest number of HAARP observations prevents computation of reliable statistics for a direct comparison, but a survey of observation times in Table 2.1 does not indicate any consistent diurnal effect, as yet, for the HAARP experiment.

Further insight is provided by a recently performed statistical analysis of 1-hop and 2-hop echo receptions from the 1986 Siple Station experiments. In 1986, the Siple transmitter was operated 139 days of the year, spaced between March 1986 and January 1987, with the largest gaps in the data being May and September due to

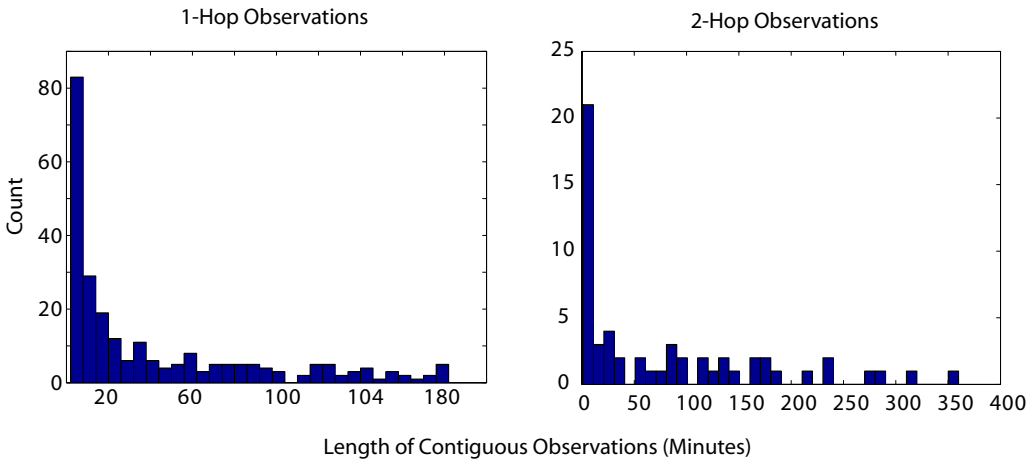

Figure 3.10: Histograms of contiguous observations of 1-hop and 2-hop echoes of Siple signals from 1986. One-hop results are from continuous recordings at the Siple conjugate point, 2-hop results are from synoptic recordings at Siple Station taken one minute out of every fifteen minutes. The short duration of observation periods agrees with HAARP results.

equipment issues. The ELF/VLF data in this period were recorded on analog magnetic tape at Siple Station and the conjugate point at Lake Mistissini in Québec, Canada. Recordings at Siple Station were made in a synoptic manner throughout the entire day. In contrast, recordings at Lake Mistissini were made in a continuous manner during periods in which the Siple facility was transmitting. All of the data from this period at both stations were digitized and 20 second spectrograms spanning 2−6 kHz were made and visually inspected for evidence of 1-hop and 2-hop echoes. A 1-hop reception was determined to have occurred if the Siple transmission was visibly detectable on the continuous spectrograms within a two-minute period. A 2-hop reception was determined to have occurred if the echo was visible during the :05, :20, :35, and :50 synoptic minutes which were common to all synoptic recording schemes used at Siple Station in 1986. The tabulated statistics were used to investigate the occurrence of 1-hop and 2-hop echo observations. Out of 7860 minutes of recordings at Siple Station during transmitter operations, 582 minutes contained 2-hop echoes

yielding an observation percentage of ∼7%. At Lake Mistissini, on the other hand, 1-hop echoes were observed 10472 out of 27408 minutes yielding an observation percentage of ∼38%. These numbers imply that 1-hop echo observations are about 5 times more likely than 2-hop echo observations.

The above direct comparison of the continuous and synoptic observation percentages needs to be understood in the context of the assumption that, statistically speaking, the synoptic recordings at Siple Station yield the same measurement of the 2-hop distribution as the continuous recordings at Lake Mistissini do of the 1-hop distribution. Since both sample sizes are sufficiently large, the only circumstance under which the assumption would not hold would be if the observations exhibited a preference for specific minutes of the hour, which is not likely for a natural phenomenon. It is perhaps not surprising that 2-hop observations are more rare since they necessitate an appreciable reflection at the conjugate ionospheric boundary, coupling back into the guiding duct, and probably reamplification during a second equatorial crossing. The HAARP observations are consistent with the Siple results in that during several observation periods, namely on 27 February 2007, 27 August 2007, and 16 March 2008, only 1-hop and no 2-hop echoes were observed.

The Siple statistics also quantify the expected duration of 1-hop and 2-hop echo observation. The left panel in Figure 3.10 shows a histogram of length of contiguous reception of 1-hop echoes in minutes, where contiguous is defined as not exhibiting gaps in echo reception longer than 4 minutes. The right panel shows the same histogram for 2-hop observations with the exception that contiguous is defined as being observed in synoptic minutes spaced 15 minutes apart. Both histograms suggest that the 20−45 minute durations of echo observation typical in the HAARP results as shown in Table 2.1 are in agreement with the Siple experiment in that the latter shows that a clear majority of contiguous observations last less than 60 minutes. These time scales on the order of tens of minutes are likely the result of changing duct geometry or coupling characteristics as discussed at the end of Section 3.3.

Even though the statistics from the Siple experiment are useful in providing a context for analysis of the new HAARP results, it is important to be aware of the differences between the two experiments. In addition to different magnetic latitudes

($L \simeq$4.3 for Siple, $L \simeq$4.9 for HAARP), the two facilities differ greatly in radiation power and pattern. For the original 960 kW HF HAARP array, radiated ELF/VLF power was estimated to range between 2 W and 30 W [*Moore et al.*, 2007; *Platino et al.*, 2006]. Assuming a best case linear scaling, the 3.6 MW HAARP array has a maximum ELF/VLF radiation power on the order of 100 W, compared to over 1 kW for the Siple transmitter [*Helliwell*, 1988]. Therefore, HAARP ELF/VLF waves injected into the magnetosphere are likely often close to the minimum threshold necessary for magnetospheric amplification on highly active paths [*Helliwell et al.*, 1980a]. Furthermore, the Siple antenna radiated power directly into the Earth-ionosphere waveguide where it would spread and leak into the magnetosphere at distances up to 200 km away from the transmitter [*Carpenter and Miller*, 1976; *Helliwell et al.*, 1980a]. Since the altitude of the HAARP modulated electrojet dipole spans the lower ionospheric reflection height ($\sim$75$-$85 km), the coupling into the Earth-ionosphere waveguide and the radiation pattern injected into the magnetosphere are much more complicated. As previously mentioned, the HAARP radiation pattern into the magnetosphere is believed to be characterized by a narrow ($\sim$30 km) 'column' geometry [*Lehtinen and Inan*, 2008; *Piddyachiy et al.*, 2008] which may reduce the chances of coupling energy (at levels that exceed the threshold of amplification) into ducts that are not directly overhead.

3.5 Summary

Based upon the current set of observations we conclude that the primary factors limiting observation of triggered whistler mode echoes are propagation conditions that include the availability of ducts to guide waves to the magnetospheric equatorial interaction region and ionospheric conditions allowing waves to be coupled into said ducts. Both observations and theory predict the necessity of a duct in the close vicinity of the heated region for echo observation. Since HAARP induced echoes have so far been observed exclusively inside the plasmapause, the best prediction metric for echo observations is quiet magnetospheric conditions yielding extension of the plasmasphere to HAARP latitudes. The prevalence of observed echoes during

quiet magnetospheric conditions is likely closely tied to the higher availability and stability of ducts under these conditions [*Carpenter and Šulić*, 1988]. The association of quiet geomagnetic conditions with weaker electrojet currents [*Baumjohann*, 1983] is likely a reason for correspondence of echo observations to weak amplitudes of HAARP signals observed on the ground. However, since disturbed conditions are associated with stronger electrojet currents and more powerful ELF/VLF generation, it is likely that HAARP induced echoes propagating outside of the plasmapause may be observed in the future, as was the case for certain transmissions during the Siple Station experiment [*Carpenter and Miller*, 1983].

Chapter 4

Characterization of Wave-Particle Dynamics: Theory and Observations

The amplification of whistler mode waves in the magnetosphere is caused by the interaction of ducted waves with hot plasma (energetic) electrons. The primary mode of interaction is cyclotron resonance in which the waves can coherently modify the energy and momentum of electrons that stream in the opposite direction. The modified energetic electron distribution subsequently radiates energy, which causes the amplification of the wave. Since the state of the energetic electrons is modified as the interaction progresses, the problem is intrinsically non-linear as is manifested by its most common features of temporal growth and generation of frequency components other than that of the input wave. The non-linearity combined with the inhomogeneity of the magnetospheric medium make the problem analytically intractable [*Matsumoto and Kimura*, 1971]. Rigorous theoretical treatment of the problem must therefore be pursued through numerical simulations. In this chapter we first outline the theoretical background and current understanding of the triggered emission instability and subsequently analyze our observations in the context of a specific numerical model. We use the model of *Gibby* [2008], which is the most recent and comprehensive treatment and constructively extends earlier numerical work of similar nature known

as the Vlasov Hybrid Simulation [*Nunn*, 1990, 1993; *Nunn et al.*, 1997, 2003, 2005].

4.1 Theoretical Background

Theoretical treatments of non-linear magnetospheric amplification and triggered emissions are typically based on several key assumptions. Because of its much higher density as compared to the hot plasma population, the cold plasma is assumed to determine wave propagation and govern the wave dispersion relation. Both hot and cold plasma populations are assumed to be collisionless. Since the frequency range of interest in the hundreds of Hz to several kHz band, the effects of ions can usually be ignored.

4.1.1 Cyclotron Resonance

Whistler mode waves in the magnetosphere propagate much slower than waves in free space and are (by definition) limited to angular frequencies ω less than the electron cyclotron frequency $\omega_c = qB_0/m_e$ where q is the fundamental charge, m_e is the rest mass of the electron, and B_0 is the strength of the static geomagnetic field. A magnetospheric duct confines propagation to the direction along the geomagnetic field line and greatly simplifies the analysis since variations need to be considered only in the dimension parallel to the magnetic field. Under these conditions, the dispersion relation for whistler mode waves is given by

$$\frac{c^2k^2}{\omega^2} = 1 + \frac{\omega_p^2}{\omega\left(\omega_c - \omega\right)} \simeq \frac{\omega_p^2}{\omega\left(\omega_c - \omega\right)} \tag{4.1}$$

where c is the free space speed of light, k is the wavenumber, and

$$\omega_p = \sqrt{\frac{q^2 N_e}{m_e \epsilon_0}}$$

is the plasma frequency, where N_e is the number density of cold electrons and ϵ_0 is the permittivity of free space. The whistler mode wave is intrinsically right hand

circularly polarized as shown in the schematic in Figure 4.1.

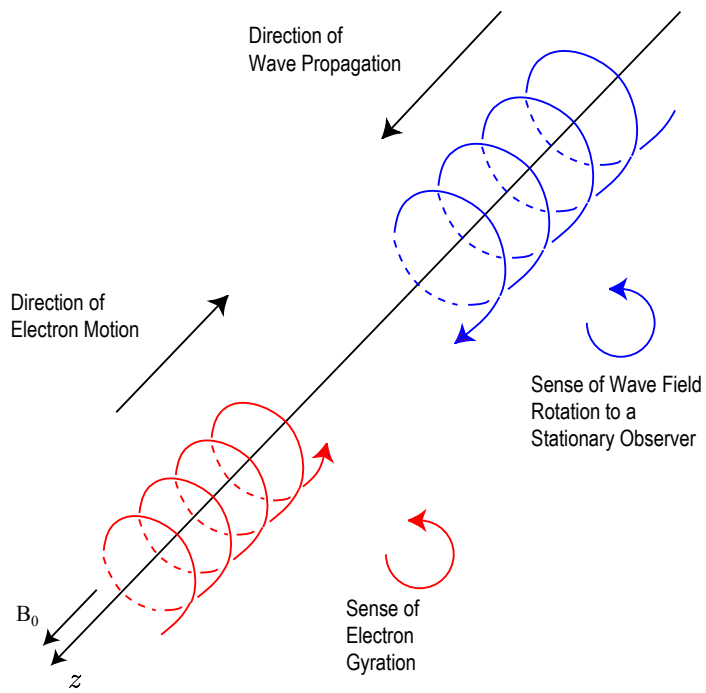

Figure 4.1: A schematic representation of cyclotron resonance, in which the sense of gyration for a counter-streaming electron is the same as the wave field rotation for a whistler mode wave propagating along the magnetic field direction. Adapted from *Walt* [1994].

The trajectories of energetic electrons in the magnetosphere are in general helical with each particle possessing velocity components both parallel ($v_{||}$) and perpendicular ($v_{\perp}$) to the geomagnetic field lines ($\mathbf{B}_0$). The direction of particle velocity with respect to $\mathbf{B}_0$ is given by the pitch angle α, where $\tan\alpha = \dfrac{v_{\perp}}{v_{||}}$. The sense of rotation for the electrons in the course of their gyromotion, as governed by the Lorentz force, is the same as the sense of rotation of the field vectors for the circularly polarized whistler mode wave (i.e., right handed). For certain values of wave frequency ω and parallel electron velocity $v_{||}$, the wave fields can be in resonance with particles traveling in the opposite direction. This interaction is illustrated in Figure 4.1 with resonance said to occur when

$$\omega_c - kv_{||} \simeq \omega \tag{4.2}$$

The resonance condition expressed in Equation (4.2) is often described as the wave frequency being Doppler-shifted into the frame of the electron such that it equals the gyrofrequency. The parallel velocity that satisfies Equation (4.2) is known as the resonant velocity and denoted by v_{R}.

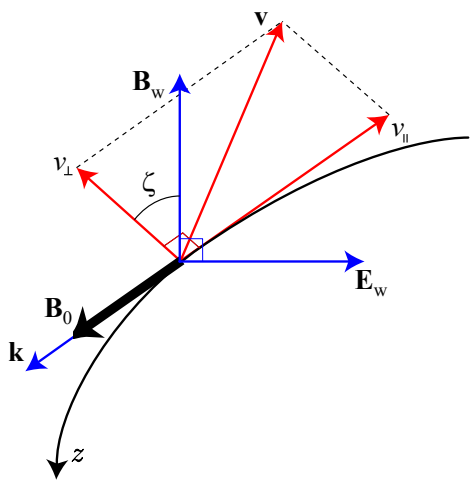

Figure 4.2: The coordinate system used to model the interaction. The whistler mode wave propagates along the magnetic field line in the $+z$ direction, while the electron streams along the field line in the $-z$ direction. The electron velocity vector is decomposed into components perpendicular and parallel to the magnetic field, with a gyrophase angle between the perpendicular velocity vector and the wave magnetic field vector. Reproduced from Figure 3.4 in *Gibby* [2008].

4.1.2 Single Particle Dynamics

When the resonance condition is satisfied, the wave and electrons can interact over non-negligible time scales. It should be noted that all terms in Equation (4.2) depend on the strength of the geomagnetic field (k also depends on the cold plasma density) and therefore vary along the propagation path. For this reason the predominant portion of the interaction occurs near the geomagnetic equator where the inhomogeneity of the magnetic field is minimized and interaction time (i.e., the time over which Equation (4.2) is valid) is maximized. The effect of the whistler mode wave on the particle trajectories in an inhomogeneous geomagnetic field can be described

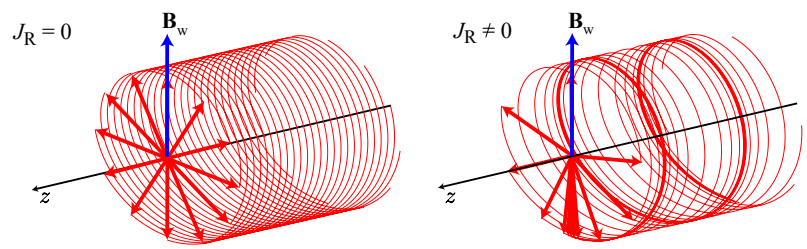

Figure 4.3: Illustration of resonant current formation. On the left twelve electrons with a single parallel velocity and uniform distribution in gyrophase yielding zero net resonant current. On the right the electrons have become 'phase-bunched' after interaction with a whistler mode wave and now their vector sum constitutes a non-zero resonant current. Adapted from *Helliwell and Crystal* [1973].

by the following equations derived from Lorentz force mechanics driven by the wave magnetic (B_w) and electric ($E_\mathrm{w} = \frac{\omega}{k} B_\mathrm{w}$) fields [*Dysthe*, 1971].

$$\frac{dz}{dt} = -v_{||} \tag{4.3}$$

$$\frac{dv_{||}}{dt} = -\frac{q}{m_e} B_\mathrm{w} v_\perp \sin\zeta - \frac{v_\perp^2}{2\omega_c}\frac{\partial\omega_c}{\partial z} \tag{4.4}$$

$$\frac{dv_\perp}{dt} = \frac{q}{m_e} B_\mathrm{w} \left(\frac{\omega}{k} + v_{||}\right) \sin\zeta + \frac{v_{||} v_\perp}{2\omega_c}\frac{\partial\omega_c}{\partial z} \tag{4.5}$$

$$\frac{d\zeta}{dt} = \omega_c - \omega - k v_{||} + \frac{q}{m_e} B_\mathrm{w} \frac{\left(\frac{\omega}{k} + v_{||}\right)}{v_\perp} \cos\zeta \tag{4.6}$$

The coordinate system for Equations (4.3)−(4.6) is presented in Figure 4.2 where E_w and B_w are the wave electric and magnetic fields respectively, and the electron velocity vector is decomposed into three components ($v_{||}$, $v_\perp$, ζ) corresponding to the parallel and perpendicular velocities with respect to the geomagnetic field and the phase angle between the perpendicular velocity vector and the wave magnetic field. The spatial dimension z is along the geomagnetic field line. Equations (4.3)−(4.6) are referred to as equations of motion since they describe the modification of particle trajectories from their adiabatic, unperturbed, state. For sufficiently high wave amplitudes the motion equations for resonant particles ($v_{||} = v_\mathrm{R}$) approach that of a pendulum with

equilibrium position at ζ=180°, and the electrons are said to be trapped in the wave potential well [*Dowden et al.*, 1978; *Bell and Inan*, 1981; *Omura et al.*, 1991]. Trapped particles are forced to remain in cyclotron resonance with the wave much longer than they would under their unperturbed adiabatic motion. There is established consensus that trapping of particles is necessary for non-linear magnetospheric amplification [*Omura et al.*, 1991; *Nunn et al.*, 2005; *Gibby et al.*, 2008]. The conditions for particle trapping are most easily presented in the form of the collective inhomogeneity factor S first derived by *Nunn* [1974]. For simplicity we present a version developed by *Omura et al.* [1991].

$$S \equiv \frac{1}{\omega_t^2}\left[\left(3v_{\mathrm{R}} - \frac{kv_\perp}{\omega_c}\right)\frac{\partial\omega_c}{\partial z} - \frac{2\omega + \omega_c}{\omega}\frac{d\omega}{dt}\right] \tag{4.7}$$

where $v_{\mathrm{R}} = (\omega - \Omega_e)/k$ is the electron resonance velocity that satisfies Equation (4.2). If $|S| < 1$ the electrons can be phase trapped in the wave potential well and oscillate with frequency approaching ω_t, also known as the trapping bandwidth, as S approaches 0. The trapping bandwidth is related to the wave amplitude B_{w} by

$$\omega_t \equiv \left(kv_\perp \frac{q}{m_e} B_{\mathrm{w}}\right)^{1/2} \tag{4.8}$$

Equations (4.7) and (4.8) show that for constant frequency pulses ($\frac{d\omega}{dt} = 0$) the wave amplitude needs to overcome only the inhomogeneity of the geomagnetic field $\frac{\partial\omega_c}{\partial z}$) in order to trap electrons. Trapping thus occurs for minimal wave amplitudes at the geomagnetic equator where $\frac{\partial\omega_c}{\partial z} = 0$. For input waves with temporally changing frequency, the $\frac{d\omega}{dt}$ term in Equation (4.7) can serve to counter balance the inhomogeneity and is likely the reason for preferential amplification of certain frequency-time signatures.

Although the number of trapped particles is small in relation to the total population, the importance of particle trapping is that a 'separatrix' is formed between trapped and untrapped particles. Trapped particles experience modification of their trajectories by the wave as they are forced to remain in cyclotron resonance. At the same time, trajectories of untrapped particles remain outside of the the wave potential

well [*Omura and Summers*, 2006]. As the trapped and untrapped electron populations both stream toward the equator, their relative trajectories are significantly modified from the unperturbed adiabatic state.

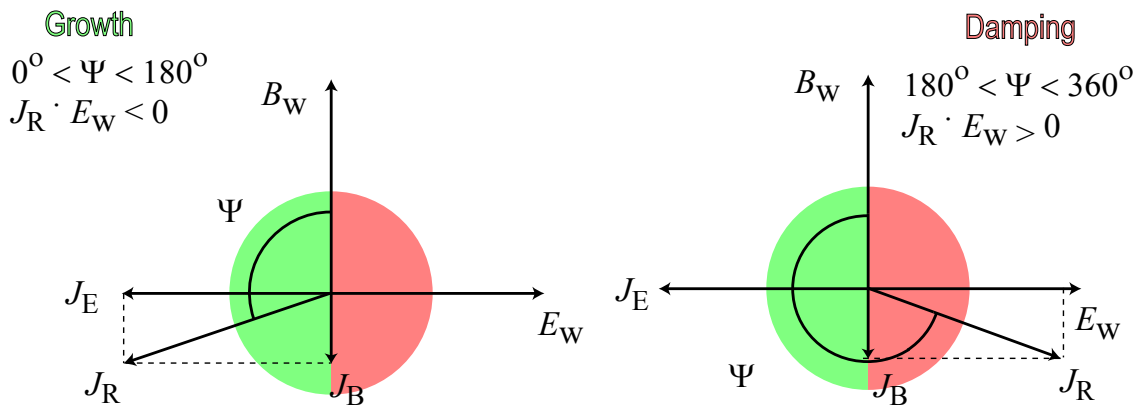

Figure 4.4: Resonant current configuration. The resonant current is divided into two components, J_E parallel to the wave electric field and J_B parallel to the wave magnetic field. Growth occurs when the angle between the resonant current vector and the wave magnetic field vector is between 0 and 180°. For angles between 180° and 360° the plasma currents damp the wave.

4.1.3 Resonant Currents

Having described the effect of the wave on single particles we next turn to the manner in which the electrons affect the wave by forming radiating currents. Although examination of single particle trajectories is effective in describing the effects of the wave, investigation of the formation of currents requires summing over the entire particle population (resonant and not resonant) and is more elegantly accomplished using a phase-space distribution function.[1] The density of electrons as a function of position and velocity is called the energetic electron velocity space distribution function, [*Gurnett and Bhattacharjee*, 2005, Sec. 7.0], expressed here as $f(\mathbf{r}, \mathbf{v})$. Since $\mathbf{r}$ and $\mathbf{v}$ are spatial and velocity vectors, respectively, f is a distribution over 6 dimensions. The

[1]Neglect of non-resonant particles in calculations of radiating currents has been criticized [*Nunn et al.*, 2005] as a shortcoming of the works of *Helliwell and Crystal* [1973] and *Carlson et al.* [1990]

radiating current flow in the hot plasma distribution is given by

$$\mathbf{J}_{\mathrm{R}} = -\left|q\right| \int\int\int \mathbf{v}_{\perp} f d^3 v \tag{4.9}$$

where the integral is taken over all velocity space [*Dowden et al.*, 1978]. Examination of the integrand in Equation (4.9) reveals that for non-zero current values the distribution cannot be uniform in $\mathbf{v}_{\perp}$. This condition is illustrated in Figure 4.3 which shows 12 electrons both uniformly distributed in gyrophase (left diagram) and 'bunched' in gyrophase (right diagram). Only the non-uniform distribution on the right hand side yields a non-zero radiating current vector. It should be noted that the illustrative example in Figure 4.3 is limited to electrons with only a single parallel velocity. Considering electrons with a single parallel velocity precludes the treatment of the case where a lower density of resonant electrons, as compared to the non-resonant ones, can still yield a non-zero result to Equation (4.9). This situation is analogous to currents in doped semiconductors where the absent electrons are termed 'holes' and their corresponding motion is referred to as a hole current. In numerical models of triggered emissions such a current formed by lower densities of resonant electrons relative to the entire distribution is observed to be formed and is termed the electron phase space hole [*Omura and Summers*, 2006; *Gibby et al.*, 2008].

The radiating currents generated in the hot plasma drive wave growth or damping. Whether the wave is amplified or attenuated depends on the orientation of the hot plasma current vector with respect to the wave fields. Figure 4.4 shows example orientations of the resonant radiant current vector in a coordinate axis of the wave electric and magnetic fields. The resonant current vector is resolved into J_{E} and J_{B}, which are components parallel to the electric and magnetic fields of the input waves. If the current vector is antiparallel to the wave electric field, the wave is amplified. If the current is in the same direction as the electric field, the net effect is damping of the wave. The resonant currents affect both the amplitude and the phase of the input wave. The evolution of the wave amplitude (B_{w}) and phase (ϕ) in the presence of a resonant current is described by the following two approximate equations [*Nunn*,

1974].

$$\frac{\partial B_{\mathrm{w}}}{\partial t} + v_g \frac{\partial B_{\mathrm{w}}}{\partial z} = -\frac{\mu_0}{2} v_g J_{\mathrm{E}} \tag{4.10}$$

$$\frac{\partial \phi}{\partial t} + v_g \frac{\partial \phi}{\partial z} = -\frac{\mu_0}{2} v_g \frac{J_{\mathrm{B}}}{B_{\mathrm{w}}} \tag{4.11}$$

The underlying assumptions and derivation of Equations (4.10) and (4.11) are presented in Appendix A.

4.1.4 Non-linear Amplification Mechanism

As has been shown, the basic effects of whistler mode waves on energetic electrons and resonant currents on propagating waves can be readily described from first principles. However, the dynamics and interplay of the two effects in the inhomogeneous magnetosphere is not easily accessible. Rigorous treatment of non-linear magnetospheric amplification is only feasible with a numerical simulation, beyond the scope of this work. What follows is a heuristic description of the amplification dynamics based on modeling results of *Gibby et al.* [2008] in close agreement also with predictions of the Vlasov Hybrid Simulation (VHS) code [*Nunn*, 1990, 1993; *Nunn et al.*, 1997, 2003, 2005].

The interaction region for magnetospheric amplification is believed to be located within a few thousand kilometers of the geomagnetic equator as illustrated in the cartoon in the left hand side of Figure 4.5. The wave amplitude threshold for electron trapping as a function of distance along the geomagnetic field can be derived from Equations (4.7) and (4.8). An example of the general shape of this curve is shown in green (B_{tr}) in panels (a)−(c) of Figure 4.5. At the magnetic equator, the magnetic field does not change ($\frac{\partial \omega_c}{\partial z} = 0$) so the trapping threshold is singularly zero. Away from the equator, the trapping threshold continually increases following the sharpening gradients of the geomagnetic field. If the input wave amplitude does not significantly exceed the trapping threshold, the input wave is only *linearly* amplified. Such a situation is illustrated in panel (a) of Figure 4.5 where the wave amplitude is shown to monotonically increase across the interaction region. Although linear amplification is also driven by resonant hot plasma currents, it intrinsically does not

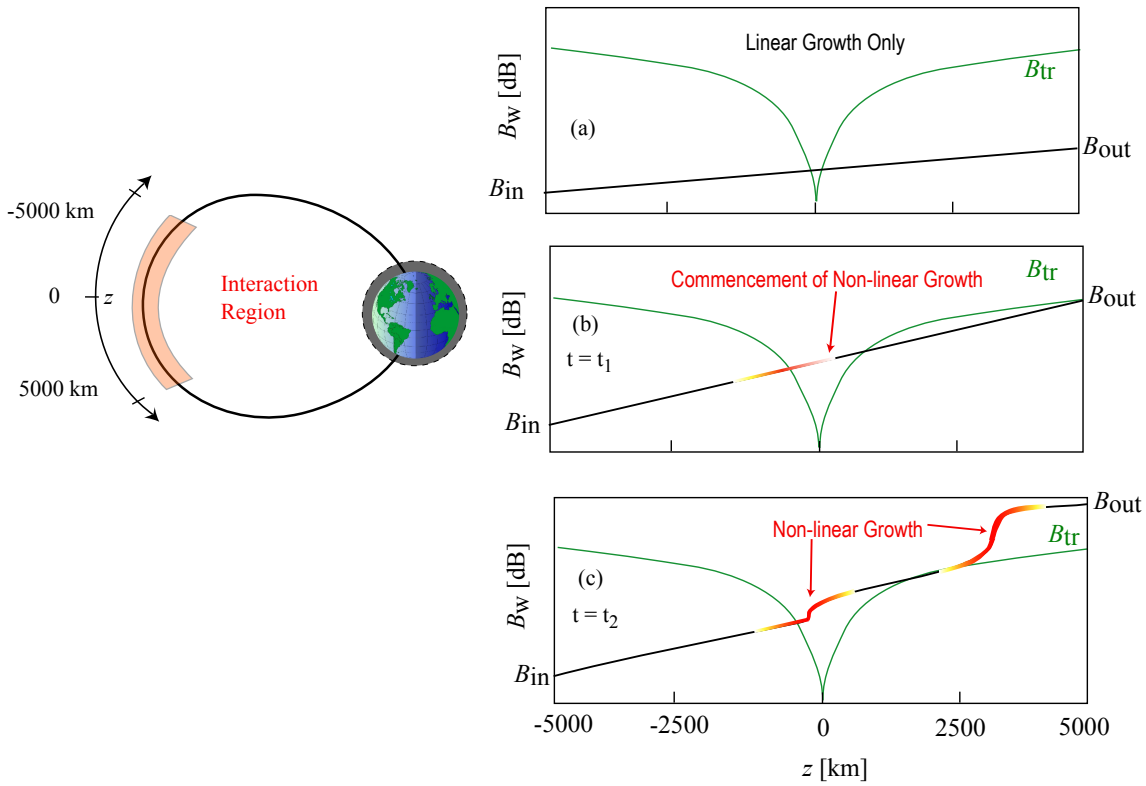

Figure 4.5: Evolution of non-linear amplification. Illustration of spatial variation of wave amplitude in the magnetospheric interaction region, which is shown in the cartoon on left hand side. The green curve ($B_{\rm tr}$) in panels (a)−(c) represents the wave amplitude threshold for electron trapping as a function of distance from the magnetic equator. In panel (a), the wave amplitude (black curve) does not exceed the trapping threshold and the wave is only linearly amplified. In panel (b) the wave amplitude exceeds the trapping threshold and non-linear growth commences. Panel (c) shows the progression of the situation in panel (b) where non-linear growth is present at two locations.

involve significant alteration of the energetic electron distribution and can be derived using a linear plasma theory approach, resulting in an imaginary component of the refractive index. Linear wave growth and its implications for hot plasma populations in the magnetosphere are discussed by *Kennel and Petschek* [1966] who show that such growth results directly from the pitch angle anisotropy of the energetic electron distribution and may therefore be an almost permanent feature of the magnetosphere because of inherent anisotropy of the electron distribution function at the very least

near the loss cone and possibly also at higher pitch angles. A theoretical study by *Karpman and Shklyar* [1972] shows that the sign of a non-linear growth rate (i.e., positive for amplification, negative for damping) must coincide with the sign of the linear growth rate.

Significant input wave amplitude or significant linear growth causes the trapping threshold to be exceeded. As shown in panel (b) of Figure 4.5, electrons are initially trapped in the region closest to the equator. Particle trapping is a prerequisite for non-linear growth but the formation of radiating resonant currents that drive the amplification depends on the phase of the trapped particles relative to the wave fields and the difference in density between the trapped and untrapped populations. In a recent paper, *Omura et al.* [2008] show that radiating currents can be estimated directly from the collective inhomogeneity factor S (see Equation (4.9)). On the other hand, *Gibby et al.* [2008] model the case of non-linear amplification with minimal subsequent triggering of free running emissions and find that the strongest radiating currents form upon the transition from the trapped state to the untrapped state. The general location of the non-linear growth region is indicated by the red arrows in Figure 4.5. The non-linear growth that commences near the equator causes the trapping threshold to be subsequently exceeded past the equator. Such a situation is illustrated in panel (c) of Figure 4.5 which shows the resultant evolution of the conditions in panel (b). In panel (c) two regions of non-linear growth are apparent and further evolution of the situation becomes increasingly complex.

Once the electrons have streamed through the interaction region and are no longer trapped in the wave potential their trajectories revert to adiabatic motion. It is this adiabatic trajectory of a radiating population of electrons that is believed to give rise to triggering of frequency risers and fallers by a monochromatic input wave [*Nunn*, 1974; *Roux and Pellat*, 1978]. Since adiabatic motion is governed solely by the inhomogeneity of the geomagnetic field, triggering of a faller versus a riser depends on the location of the downstream boundary of the trapping region in relation to the equator. In the case analyzed by *Gibby et al.* [2008] the radiating currents of the electrons that transition from the trapped to untrapped state work to eventually attenuate the input wave after initial amplification. This result comes about because

the downstream trapping boundary for this case is located close to the equator. Near the equator the geomagnetic inhomogeneity is a minimum and the phase variation associated with adiabatic motion of previously resonant electrons is only on the scale of a single wave period (i.e., not fast enough to generate a significant frequency change). For such slow phase variations, including those in the main trapping region, it is useful to frame the resonating currents in terms of the magnitude and direction of the non-linear current vector with respect to the wave fields as shown in Figure 4.4. In the *Gibby et al.* [2008] treatment, the local inhomogeneity of the geomagnetic field causes the current vector that initially drove amplification to eventually swing past 180° and begin to attenuate the wave. This attenuation is posited by *Gibby et al.* [2008] to be the mechanism responsible for the saturation effect in VLF triggered emissions.

In general, after the initiation of non-linear growth, the dynamics in the interaction region are an interplay between attenuation caused by populations that move into the damping phase and amplification by more recently trapped populations up the field line. The specific evolution of the process is determined by the distribution of spatial gradients in wave amplitude, thus making the input wave amplitude and the hot electron flux and anisotropy key parameters of this interaction.

4.2 Observations in Theoretical Context

Terrestrial ELF/VLF wave injection experiments are rigorous methods of magnetospheric probing, but can be inherently challenging to compare directly to theoretical predictions since ground based observations represent the combined effects of many complex and sometimes competing processes in the magnetospheric interaction region. Parameters determined from observations thus correspond to integrated values of variables used in theoretical formulations, where the integrals are taken spatially over the entire interaction region. Furthermore, propagation from the interaction region to the ground based receiver entails many loss mechanisms such as ionospheric absorption and scattering that are difficult to quantify. Nevertheless, ground based

amplitude and phase measurements can serve to quantify key parameters and elucidate dynamics.

4.2.1 Resonance and Trapping Conditions

Magnetospherically amplified signals are known to spread in bandwidth [*Stiles and Helliwell*, 1975] with the broadened spectrum corresponding to the trapping bandwidth in Equation (4.8). It is thus possible to use the observed bandwidth broadening to estimate the trapping wave amplitude in the interaction region. We focus here on 1-hop observations since they involve only a single traverse of the interaction region. Panel (a) in Figure 4.6 shows a spectrogram of a 1-hop echo observed on Buoy 1.5, triggered by a 1100 Hz transmitted pulse. Panel (b) shows the frequency spectrum of a portion of this echo enclosed by the white dotted lines in panel (a). It is observed that the bandwidth of the echo is $\sim$50 Hz compared to the less than 1 Hz bandwidth of the original HAARP transmitted pulse. Using the observed bandwidth as a measure of the trapping bandwidth (ω_t), the trapping wave amplitude (B_{w}) can be calculated from Equation (4.8) if values for pitch angle and cold plasma density are assumed. Based on the propagation time and the magnetospheric path results discussed in Chapter 3, an equatorial electron density of 250 cm^{-3} at L=4.9 is reasonable.

Panel (c) in Figure 4.6 shows the resulting wave amplitudes and resonant electron energies versus pitch angle calculated at the geomagnetic equator. The shaded region in Figure 4.6 corresponds to high pitch angle (α >60°) electrons that likely drive the gyroresonance instability [*Bell et al.*, 2000]. The electrons involved in the amplification of the injected waves must have had energies ranging from a few tens to 100 keV with trapping wave amplitudes in the range 0.1−0.4 pT. The results in Figure 4.6 are typical for other observations for which such calculations were performed [*Inan et al.*, 2004]. The estimation of the trapping wave amplitude is significant since the amplitude of the wave in the interaction region is a parameter that has never been measured directly as such an observation requires an extremely fortuitous satellite pass. From these results we conclude that at L-shells accessible to HAARP signals magnetospheric amplification requires ducted wave amplitudes of a few tenths of pT

and interaction with electrons in the tens of keV range.

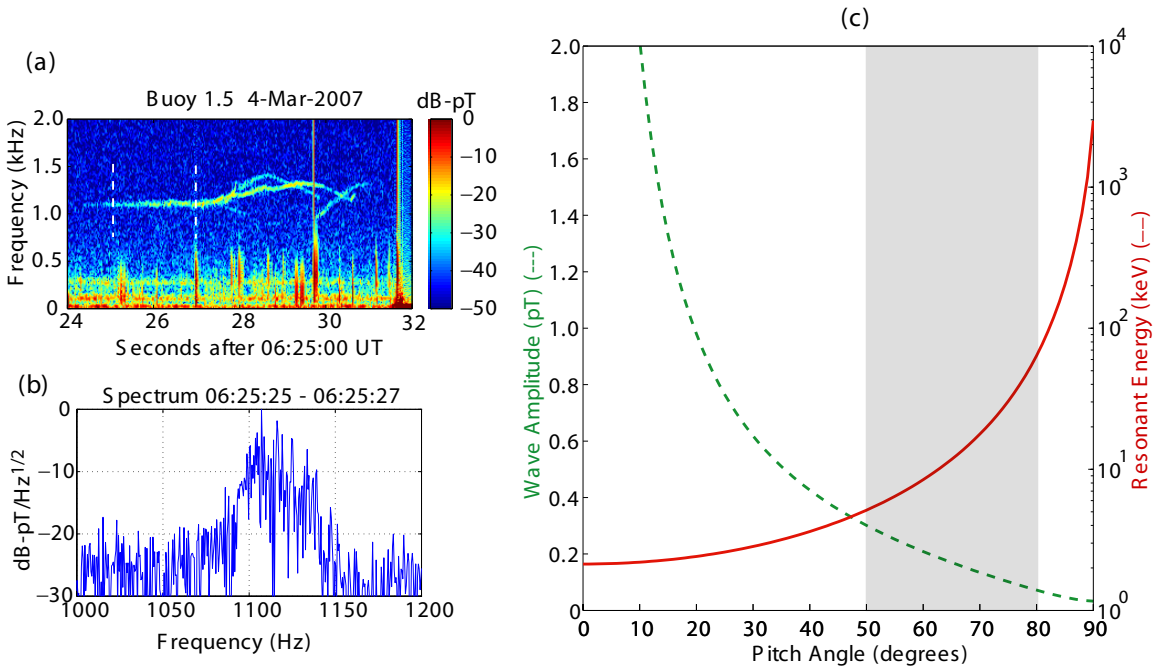

Figure 4.6: One-hop echo and associated frequency spectrum observed on Buoy 1.5 shown in panels (a) and (b). Panel (c) shows resonant electron energies (solid red line) and trapping wave amplitude (dashed green line) versus equatorial pitch angle values. The shaded region corresponds to pitch angles between 50° and 80° believed to be the main driver of amplification.

4.2.2 Characterization of Non-linear Resonant Current

Using the evolution of the amplitude and phase of whistler mode echoes it is possible to characterize the dynamics of the non-linear current vector in the magnetosphere. Equations (4.10) and (4.11) show that variation of the wave amplitude and phase is driven by the components of the current vector. At any instance in time, the spatial variations of wave amplitude and currents in the interaction region can be expressed as:

$$\frac{\partial B_{\mathrm{w}}}{\partial z} = -\frac{\mu_0}{2} J_{\mathrm{E}} \tag{4.12}$$

$$\frac{\partial \phi}{\partial z} = -\frac{\mu_0}{2}\frac{J_\mathrm{B}}{B_\mathrm{w}} \tag{4.13}$$

The change in wave amplitude in Equation (4.12) can also be manipulated to express an exponential growth rate γ.

$$\gamma = \frac{1}{B_\mathrm{w}}\frac{\partial B_\mathrm{w}}{\partial z} = -\frac{\mu_0 J_\mathrm{E}}{2B_\mathrm{w}} \tag{4.14}$$

As mentioned above, any quantities observed on the ground are the result of dynamics integrated over the entire interaction region. The growth rate and phase as observed on the ground are thus given by

$$\gamma_\mathrm{obs} = \int_{-\Delta z}^{\Delta z} \gamma dz = \int_{-\Delta z}^{\Delta z} -\frac{\mu_0 J_E}{2B_\mathrm{w}} dz \tag{4.15}$$

$$\phi_\mathrm{obs} = \int_{-\Delta z}^{\Delta z} \frac{d\phi}{dz} dz = \int_{-\Delta z}^{\Delta z} -\frac{\mu_0 J_\mathrm{B}}{2B_\mathrm{w}} dz \tag{4.16}$$

The integrals in Equations (4.15) and (4.16) constitute average values of the resonant currents over the interaction region, i.e.,

$$\gamma_\mathrm{obs} = -\mu_0 \left\langle \frac{J_\mathrm{E}}{B_\mathrm{w}} \right\rangle \Delta z \tag{4.17}$$

$$\phi_\mathrm{obs} = -\mu_0 \left\langle \frac{J_\mathrm{B}}{B_\mathrm{w}} \right\rangle \Delta z \tag{4.18}$$

The observed phase and amplitude can thus be used to estimate the average magnitude ($\langle |J_\mathrm{R}| \rangle$) and orientation ($\langle \Psi \rangle$) of the non-linear resonant current vector as illustrated in Figure 4.4.

$$\langle |J_\mathrm{R}| \rangle \propto \sqrt{\gamma_\mathrm{obs}^2 + \phi_\mathrm{obs}^2} \tag{4.19}$$

$$\tan \langle \Psi \rangle = \frac{-J_\mathrm{E}}{J_\mathrm{B}} \simeq \frac{-\gamma_\mathrm{obs}}{\phi_\mathrm{obs}} \tag{4.20}$$

Although the magnitude and orientation expressed in Equations (4.19) and (4.20) are average values across the entire interaction region, their joint evolution in time is illustrative of the dynamics of the amplification mechanism and serves to relate

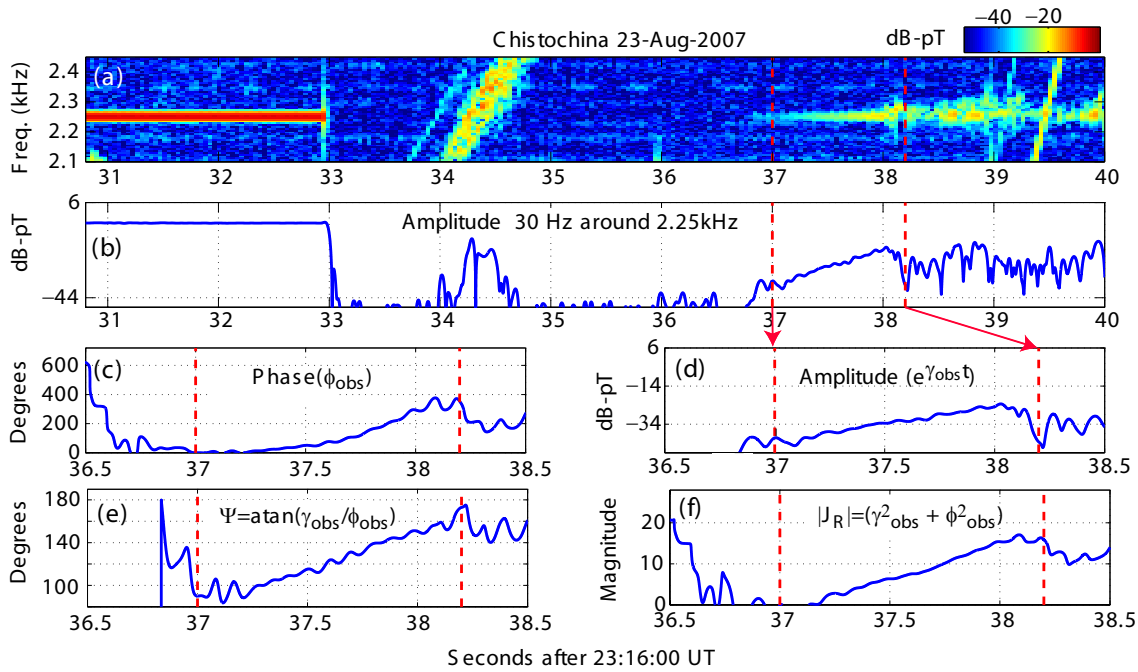

Figure 4.7: Spectrogram of transmitted 2.25 kHz pulse and triggered 2-hop echo (panel (a)). Corresponding amplitude in a narrow band around transmission frequency is shown in panel (b). Amplitude and phase for the 2-hop echo only (demarked by red dotted lines) are shown in panels (c) and (d). Panels (e) and (f) show the derived magnitude and phase of the non-linear current vector.

ground observations to theoretical formulations. Figure 4.7 shows an example measurement in which the average non-linear current vector has been decomposed from a 2-hop echo observation. Panel (a) in Figure 4.7 shows a spectrogram from Chistochina where a 2-hop echo is seen to be triggered by a 2.25 kHz, 3-second pulse. Panel (b) shows the amplitude in a 30 Hz bandwidth around the pulse frequency. In panels (c) and (d) the phase and amplitude of the 2-hop echo have been isolated corresponding to the red dotted lines in the upper panels. We have limited our analysis to the initial growth phase of the 2-hop echoes before any triggering of emissions with rapidly changing frequencies. In the context of the generation mechanism this portion of the interaction corresponds to radiating currents generated by electrons

within the particle trap or just outside of the trap but close to the equator as presented in *Gibby et al.* [2008]. Panels (e) and (f) show the calculated average phase and magnitude of the non-linear current vector as derived from the 2-hop echo phase and amplitude using Equations (4.19) and (4.20). It is seen that as the 2-hop echo amplitude increases, the magnitude of the resonant current vector also increases and the phase angle approaches 180°. This result is not surprising since after its growth phase the 2-hop echo is seen to saturate and attenuate, which is manifested by the resonant current vector surpassing 180° in phase (see Figure 4.4). After the 2-hop echo becomes dominated by off frequency components (after 38.3 seconds, second red line) the measurement of its relative phase is no longer possible. The general calculated behavior of the resonant current vector is as predicted by theoretical models, especially the notion of saturation as described by *Gibby et al.* [2008]. More specifically, the amplitude and phase during initial non-linear growth are both observed to increase but phase advance outpaces amplitude growth. According to Equations (4.10)−(4.11) this more rapid phase advance relative to amplitude growth implies rotation (clockwise in Figure 4.4) of the non-linear current vector and is in agreement with numerical models [*Omura and Summers*, 2006; *Gibby*, 2008].

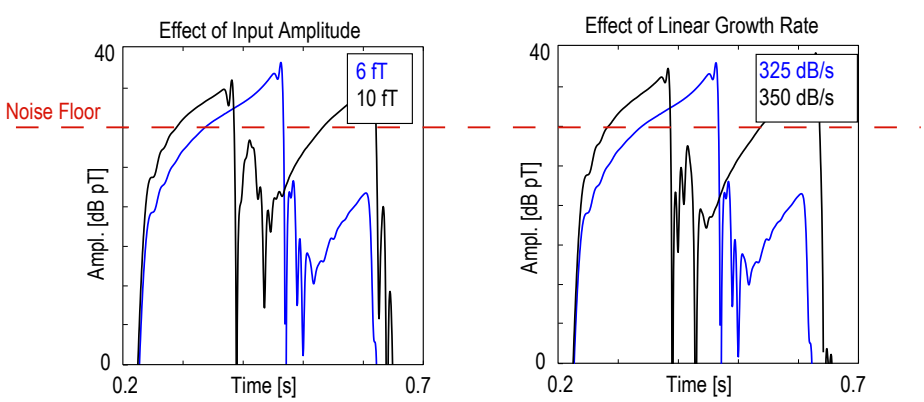

Figure 4.8: Predicted echo amplitudes as a function of time for different input wave amplitude (left panel) and different linear growth rates (right panel). The red dotted line shows a realistic noise floor that would limit observations and indicates that for a ground based receiver the effect of lower input amplitude or lower linear growth would both yield delayed onset of observations. Adapted from *Gibby* [2008].

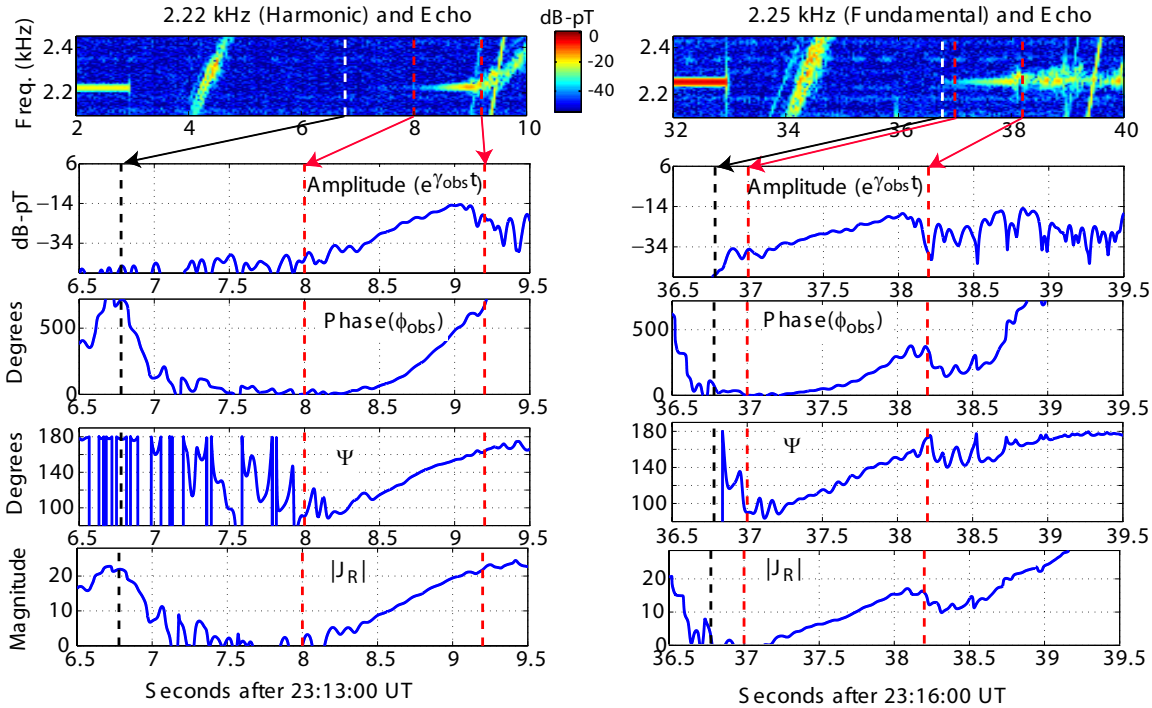

Figure 4.9: The panels on the left hand side show the observed amplitude and phase, and derived non-linear current vector parameters for a 2-hop echo excited by a 2.22 kHz signal that is a harmonic of a 1.11 kHz transmission. The panels on the right hand side show the same parameters for a 2-hop echo excited by a 2.25 kHz fundamental transmission. Black and white dotted lines are reference lines showing constant delay from transmission. Red dotted lines demark echo onset and coherent growth phase. The harmonic signal is ∼14 dB weaker than the fundamental transmission and the 2-hop echo excited by the harmonic is observed to arrive with a ∼1 second delay in relation to the 2-hop echo from the fundamental transmission.

The tracking of the vector decomposition of the non-linear current allows for a more detailed interpretation of observations in a theoretical context. Figure 4.8 shows the results of a sensitivity study performed using the numerical model of *Gibby* [2008]. The two panels in Figure 4.8 show the predicted echo amplitudes as a function of time for different input wave amplitudes (left panel) and different *linear* growth rates (right panel). The red dotted line shows a noise floor that would exist for any realistic observations of the phenomena, limiting observations to amplitudes above the line.

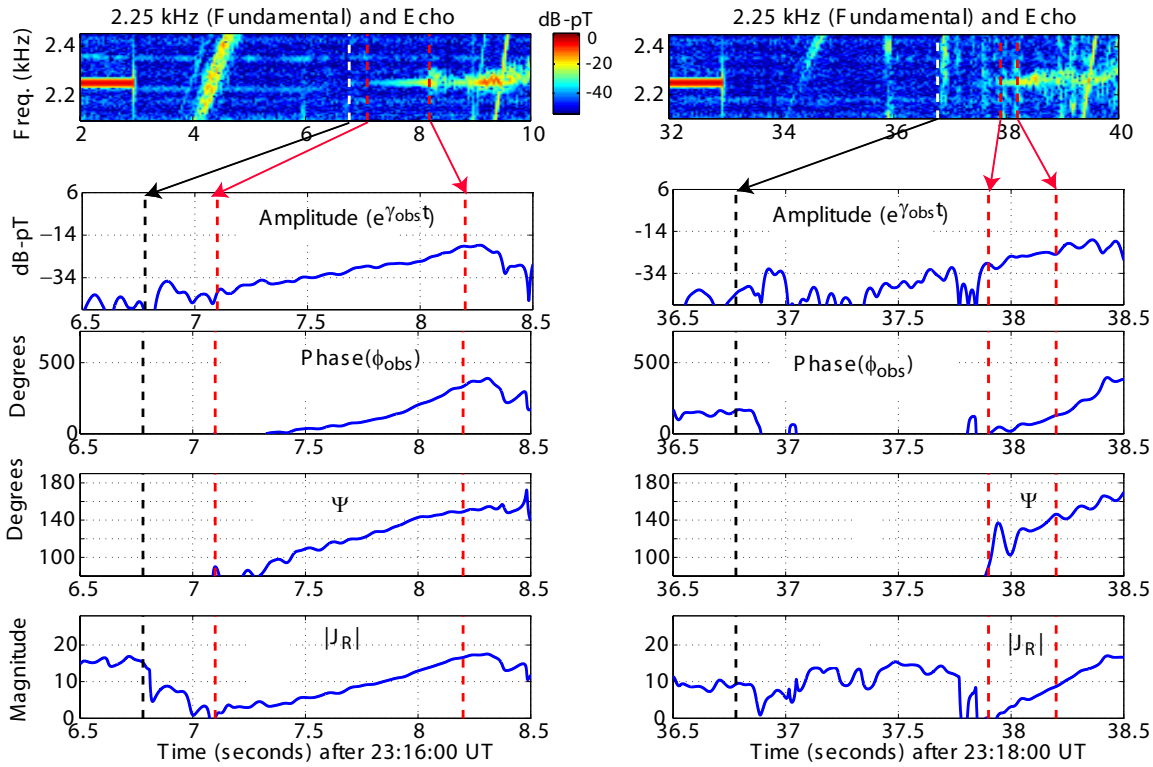

Figure 4.10: Same as Figure 4.9 except that now both echoes are triggered by signals of the same amplitude and the difference in onset delay is attributed to lower linear amplification.

The level of the noise floor above the non-linear growth threshold is appropriate for the HAARP experiment since all recorded observations of echoes exhibit temporal growth, meaning that unlike in the Siple Station experiment [*Paschal and Helliwell*, 1984] the noise floor is above amplitudes that result solely from linear growth. The numerical results indicate that for a ground based receiver the effect of the lower input amplitude or lower linear growth rate would be the same, namely a delayed echo onset time. As discussed in Section 4.1.4, the dynamics of the amplification are determined by the presence of wave amplitude gradients with respect to the trapping amplitude threshold. Part of the reason for the similarity between variations of the input amplitude and linear growth rate is that both lead to lower wave amplitudes in the interaction region and cause the primary trapping of electrons to occur further

up the field line, leading to a delayed observation onset (see Figure 4.5).

The delayed onset of echo observations resulting from different input amplitudes can be seen in the HAARP observations. Figure 4.9 show the same analysis for two cases of similar frequency and format, but significantly different input amplitude observed only 3 minutes apart. The left hand panels in Figure 4.9 show the analysis of an echo triggered at 23:16 UT by a pulse at 2.22 kHz that is a harmonic of a fundamental transmission at 1.11 kHz. The harmonic is much weaker (about 14 dB) than the fundamental as is normally the case. The panels on the right hand side of Figure 4.9 show analysis of an echo excited by a fundamental tone at 2.25 kHz at 23:16 UT after a transmission format change at 23:14 UT. The white dashed line in the spectrograms in the top row corresponds to the black dotted lines in the lower panels and all of these lines are reference lines representing constant delay from transmission across both cases. The two red dashed lines respectively mark the onset of the observed 2-hop echoes and the end of the coherent growth phase of those echoes. The echo in the low amplitude (harmonic) case is seen to arrive much later than the higher amplitude (fundamental) transmission. The significantly closer proximity of the white and black lines to the first red line in the second case shows that the higher input amplitude leads to a delayed echo onset of about a full second in this case. It is important to note that apart from this onset delay, the dynamics of the amplification for the two cases is strikingly similar, as can be seen in the similarity of the average magnitude and phase of the non-linear current vector in the bottom four panels of Figure 4.9. Both cases show an increase in amplitude and advance of phase to 180°, at about the same rates.

The correspondence of onset delay to input amplitude variation illustrated in Figure 4.9 is further evidence of the degree to which the observations agree with the numerical results of *Gibby et al.* [2008] and *Gibby* [2008]. Moreover, having exposed this close connection it is also possible to use the observations to comparatively investigate the hot plasma distribution in the magnetosphere. Figure 4.10 shows a presentation identical to Figure 4.9 except that now the 2-hop echoes are triggered by pulses that are both fundamental tones and consequently have the same amplitude. The disparity in spacing between the reference lines and red lines of echo onset

across the two cases in Figure 4.10 shows that for the right hand case the echo onset is delayed. Given that the two input amplitudes are the same, based on the predictions of the *Gibby* [2008] model, the difference in arrival onset can be inferred to result from a lower linear amplification. A lower linear amplification results from either a lower electron flux or a lower pitch angle anisotropy of the electron distribution. The observed amplitude and phase of ground based observations can thus be used to track the evolution of the hot plasma distribution in the magnetosphere. Although observations of phase and amplitude of whistler mode echoes have been reported before [*Dowden et al.*, 1978; *Paschal and Helliwell*, 1984], the analysis presented herein constitutes the first interpretation of the observed joint variation of amplitude and phase in the context of a rigorous numerical model.

Chapter 5

Cross Modulation between Whistler Mode Echoes and HF Heating

In this chapter we present a new phenomenon serendipitously discovered in the course of HAARP wave injection experiments. The observations are interpreted in a theoretical context and the observed concept is investigated experimentally as a new method for ELF/VLF wave generation with the HAARP heating facility.

5.1 Observation

The first and most representative observation of cross modulation between whistler mode echoes and HF heating occurred on 23 August 2007. Figure 5.1 shows a spectrogram record from Chistochina in which HAARP transmissions and corresponding triggered 2-hop echoes are marked by the white arrows. In addition to the 2-hop echoes excited by the ramps and pulses, 'replicas' of the 2-hop echoes shifted up in frequency are visible in the record as shown by the black arrows. The frequency shift of the echo replicas corresponds exactly to the ELF frequency of the simultaneous HAARP transmission. The replicas thus appear to be a direct result of non-linear cross modulation between the incoming 2-hop echoes and the concurrent modulation

of the HF heater. One of the first implications of the observations of such cross modulation is that the 2-hop echoes on their return to the northern hemisphere must have been propagating through the ionosphere in the heated region above the HAARP facility. This is in direct agreement with the whistler mode path determination results for this day and others discussed in Chapter 3 and supports the accuracy of the dispersion analysis and path determination techniques therein.

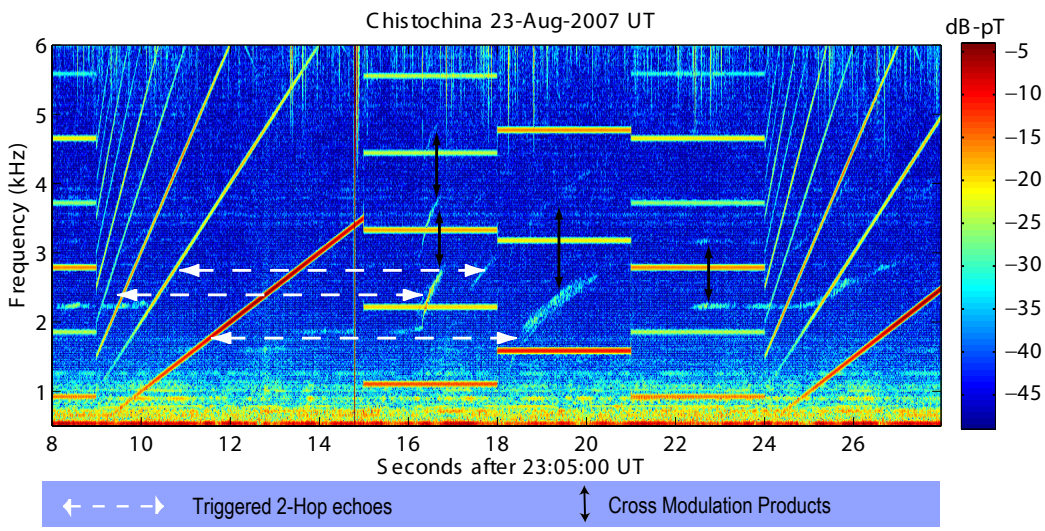

Figure 5.1: Echo heating cross modulation observed at Chistochina. HAARP transmitted ramps and pulses excite 2-hop echoes. Modulation products of 2-hop echoes with simultaneous HAARP transmissions are also seen in the record.

5.2 Theoretical Modeling

The cross modulation effect is exhibited by echoes propagating through the HF heated region. The HF modulated heating modifies the conductivity of the ionosphere and thereby changes the propagation characteristics for electromagnetic waves propagating in this medium. To study the effects of HF waves on the ionosphere we use a numerical heating model which takes into account the propagation of and energy deposition by the HF waves as a function of time and altitude. Here we rely on a

numerical heating model based on the work of *Moore* [2007]. Figure 5.2 shows the effect of a single 1.110 kHz AM modulation cycle on typical daytime and nighttime ionospheres and the corresponding induced propagation characteristics for a 2 kHz wave. The primary effect of the HF heating is to change the electron temperature as shown in panel (b) of Figure 5.2. The electron temperature change manifests itself almost exclusively as a change in wave attenuation (panel (d)), leaving the real part of the refraction index (wavenumber in panel (c)) virtually unchanged. It is this modulating attenuation in sync with the ELF/VLF AM modulation of the HF beam that generates the cross modulation products shown in Figure 5.1. This phenomenon is analogous to the Luxembourg effect [*Bailey and Martyn*, 1934] in that one signal modifies the ionosphere and so imposes its modulation on another signal that propagates through or in the vicinity of the same medium. Manifestation of this effect in the VLF band was reported by *Inan* [1990]. It is clear from panel (d) in Figure 5.2 that the change in attenuation is more dramatic for a daytime ionospheric profile in agreement with the observations on 23 August 2007 which took place during 12:00 MLT.

A quantitative comparison of the observed cross modulation and that predicted by the numerical heating model can be achieved by examining the frequency spectra. Panel (a) in Figure 5.3 shows a spectrogram of an observed 2-hop echo and its cross modulation products from a simultaneous 1110 Hz HAARP transmission. Panel (c) shows the frequency spectrum at the time corresponding to the white dotted line in panel (a). The 'fundamental' echo is identified in panel (c) with the red arrow and its primary cross modulation products (spaced by 1110 Hz) are identified with black arrows. Panel (b) shows 2 periods of the attenuation waveform that results from propagation through the modified ionosphere as shown in Figure 5.2. The attenuation wave form is calculated assuming vertical propagation of a 2 kHz wave through the center of the modeled heating region. The attenuation waveform is therefore a time series of vertical integrations of the imaginary part of the refractive index in the ionosphere for a 2 kHz wave. The 2 kHz frequency is chosen since this frequency is close to the band of the 'fundamental' echo in Figure 5.3. Panel (d) in Figure 5.3 shows the predicted raw cross modulation spectrum obtained by multiplying the

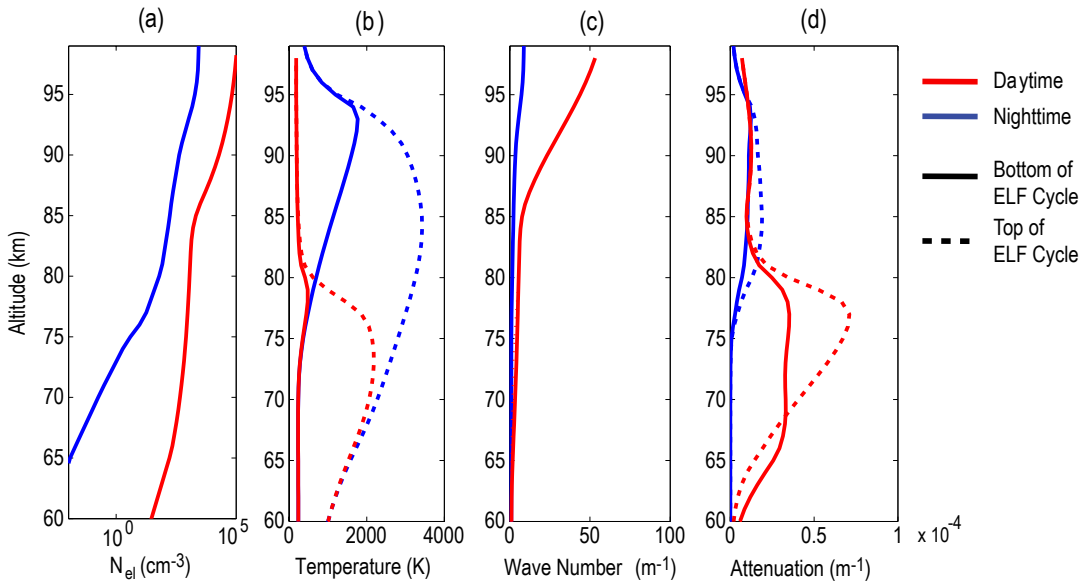

Figure 5.2: Effect of HF modulated heating on ionospheric medium. Typical daytime and nighttime profiles are shown in panel (a). The resulting electron temperature increase from modulated heating is shown in panel (b). Panels (c) and (d) show the wave number and attenuation for a 2 kHz wave corresponding to the real and imaginary parts of the refractive index.

attenuation waveform by a sinusoid at the echo fundamental frequency of 2450 Hz. The spectrum in panel (d) is obtained by multiplication of two waveforms but it must be noted that the observed modulation products are the result of radiating currents from the interaction region, which in this case is the HF heated region. Since the heated region is on the order of ∼30 km it is much smaller than the wavelengths of the echo and any cross modulation products. The cross modulation products are thus radiated with frequency dependent radiation efficiency as for an elementary Hertzian dipole. *Inan and Inan* [2000] present the following simplified formula for the Hertzian dipole radiation efficiency [p. 491]

$$P_{\text{rad}} \propto 80\pi^2 \left(\frac{dl}{\lambda}\right)^2 \tag{5.1}$$

where dl is the length of the antenna and λ is the wavelength. Equation (5.1) shows

that the expected radiated power pattern is inversely proportional to the square of the wavelength or directly proportional to the square of the frequency. Panel (e) in Figure 5.3 shows the cross modulation spectrum after such frequency scaling. The scaled spectrum in panel (e) shows excellent agreement with the observed spectrum in panel (a). In particular, the levels of the upper modulation products at 3560 Hz and 4670 Hz agree in relative magnitude. In the observed spectrum the amplitudes of these components as shown in the figure are -30.7 and -36.5, respectively, while in the predicted spectrum the amplitudes are -13.8 and -19.6. In both cases the difference between the components is -5.8 dB. The close agreement suggests that our interpretation of the phenomenon is basically correct and also that the ionospheric and HF heating models utilized are accurate. It should be noted that any comparison to the amplitudes of the 'fundamental' components at 2450 Hz is not meaningful since for the observed case this amplitude represents the portion of the 2-hop echo that does not exhibit cross modulation and is received directly from the magnetosphere. In the modeled case the component at 2450 Hz results was arbitrarily set to 0 dB.

One of the characteristics of the observed cross modulation products in Figure 5.1 and panel (a) in Figure 5.3 is the prominence of the upshifted products (frequency sums) over the downshifted (frequency differences) products. The frequency differences are not readily visible in the spectrograms at all. The spectrum in panel (c) of Figure 5.3 shows that this result is in part due to the increased noise floor below $\sim$2 kHz and also the small antenna radiation scaling discussed above. Although not readily visible in the spectrogram, the frequency difference component at 1340 Hz can be seen marked by the black arrow in panel (c) of Figure 5.3.

5.3 Cross Modulation for Generation

The observation of cross modulation of ELF/VLF signals in the HAARP heated region suggests the possibility of using the same concept as a new method for ELF/VLF generation with the HAARP HF facility. In particular, it is desirable to extend generation beyond the hardware imposed 30 kHz upper limit of AM modulation and explore possibly more efficient methods of generating low ELF and ULF frequencies.

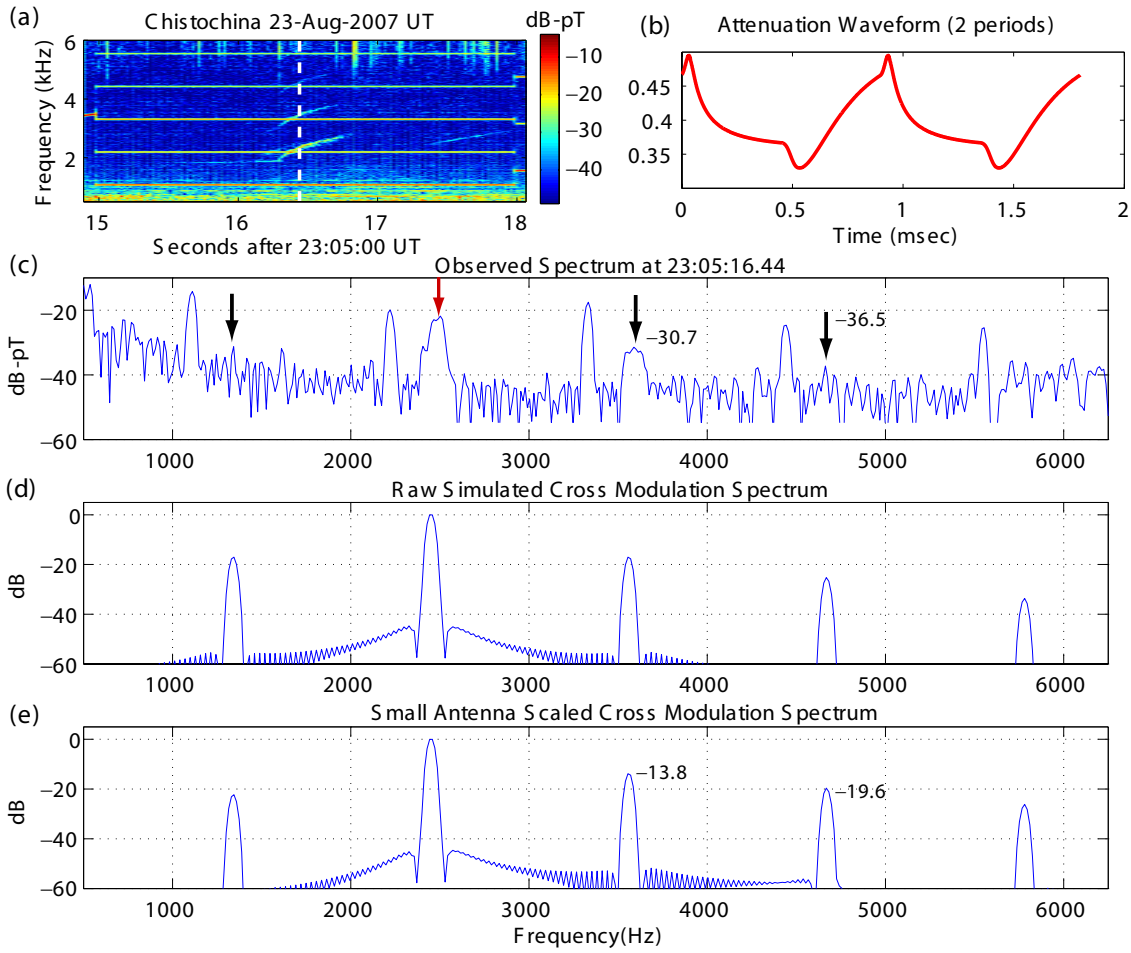

Figure 5.3: Spectrogram with 2-hop echo and cross modulation products from a 1110 Hz transmission in panel (a). Panel (c) shows the spectrum corresponding to the time denoted by the white doted line in panel (a). Panel (b) shows the time dependent attenuation caused by HF heating with 1110 Hz amplitude modulation. The spectrum of the attenuation wave form modulated by the instantaneous 2-hop frequency observed in panel (c) is shown in panel (d). Panel (e) shows the same result as panel (d) but scaled by the small antenna frequency dependence.

The cross modulation based generation concept is presented in Figure 5.4. Whereas the original observations of cross modulation involved an incident 2-hop echo and the beam of the full HF array, the new generation concept involves splitting the array to generate two co-located HF beams. The role of the 2-hop echo can then be taken up by the higher frequency HF beam since a higher HF frequency yields a higher effective dipole altitude. The cross modulation products would be generated when waves from the higher HF dipole are modulated by the attenuation induced by the lower HF beam. The frequencies chosen for the experiment were 2.75 MHz and 4.5 MHz.

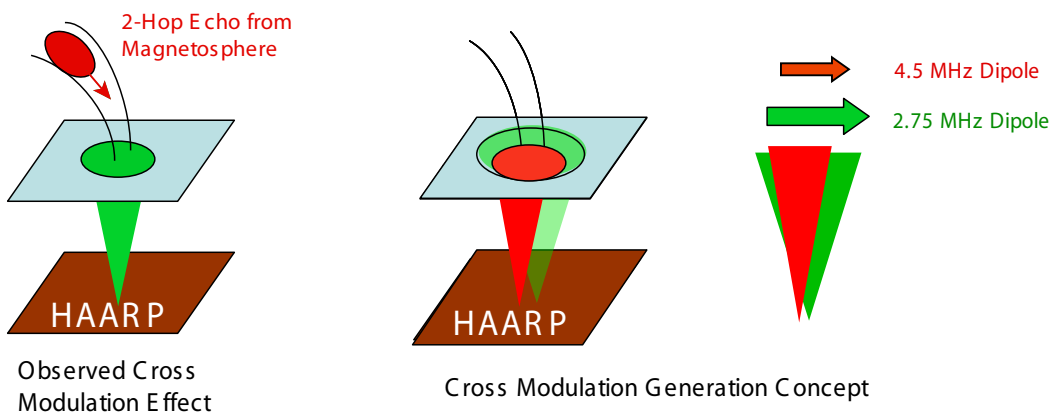

Figure 5.4: Concept for using cross modulation as a generation technique.

Figure 5.5 shows a sample record from an experimental run designed to test this alternate form of generation for the low kHz band. The top panel shows the transmission format consisting of two simultaneous modulations on 2 HF carriers. In the bottom 4 panels, narrowband amplitude data from Chistochina show detection of signals at frequencies corresponding to the sums of the modulated pulses, clear evidence that the method does indeed generate the expected frequencies. Analogous experiments were performed over a wide range of desired output frequencies ranging from 630 Hz to 37 kHz using various combinations of driver frequencies. Figure 5.6 shows the cumulative frequency response of the cross modulation method as well as

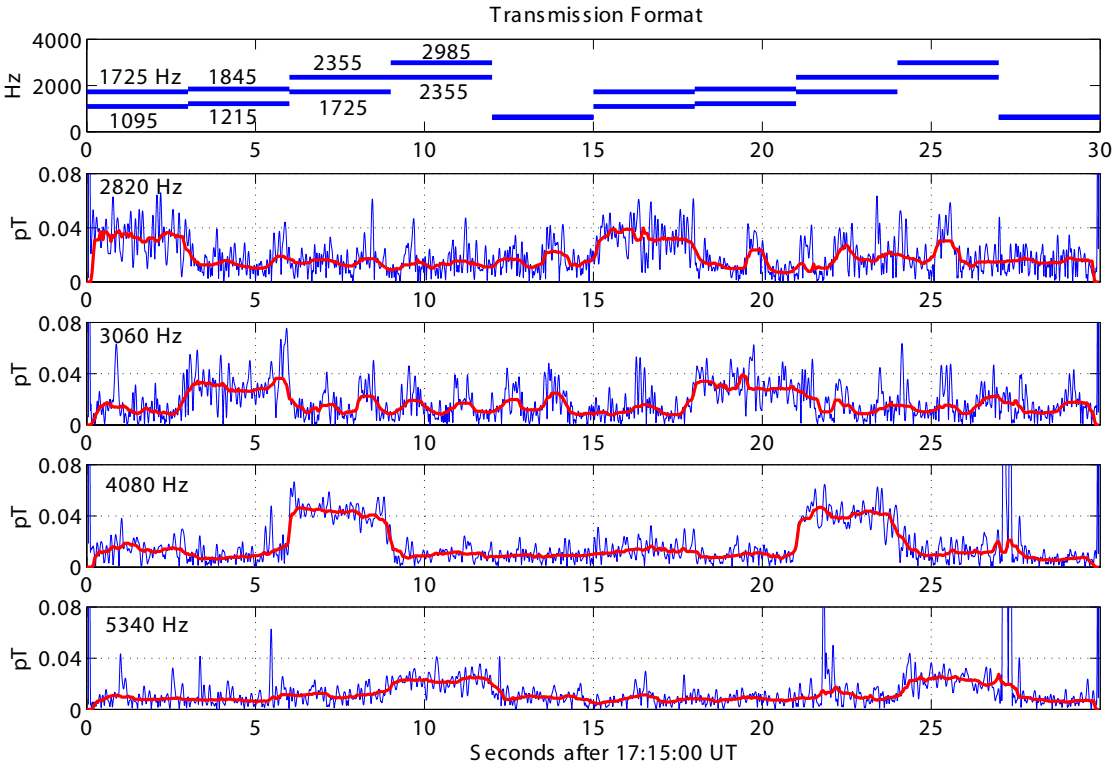

Figure 5.5: Example data from Chistochina showing generation of cross modulation (frequency sum) products.

conventional AM generation and observed noise floor recorded at the same time. Although data in Figure 5.6 illustrates that the cross modulation generation method generates observable signals in a wide frequency range, the technique is seen to yield signal amplitudes about an order of magnitude lower than conventional AM generation. The relative frequency response appears to be similar for both techniques as shown by the best fit lines in Figure 5.6. The maximum at ∼2 kHz is the ionospheric resonator effect typical for all ionospheric modulation techniques.

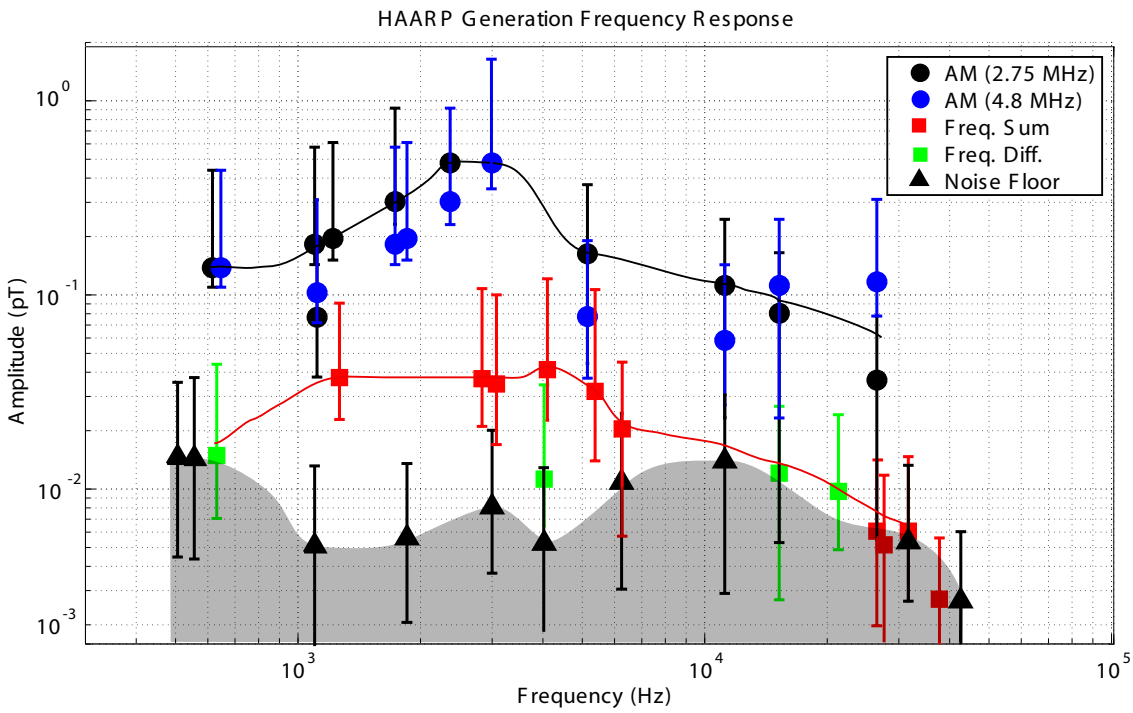

Figure 5.6: Results of HAARP generation using AM modulation (circles) and the cross modulation technique (squares). The range bars show the minimum, mean, and maximum signals observed.

Chapter 6

HAARP Induced Electron Precipitation

A secondary goal of the HAARP wave injection experiments is to induce and detect controlled loss of energetic radiation belt electrons from the magnetosphere. Under strict adiabatic conditions, the energetic particles executing helical motion in the magnetosphere remain trapped indefinitely. However, numerous processes, including cyclotron resonance interactions with whistler mode waves, can perturb particle trajectories from their trapped motion to one in which the particles mirror at lower altitudes and are lost to collisions with atmospheric constituents. The loss of a previously trapped magnetospheric particle to collisions in the atmosphere is known as particle precipitation. The change in direction of the momentum of a particle induced by a wave is known as pitch angle scattering. When the equatorial pitch angle of a particle falls below the so called loss cone angle, the particle is precipitated within a bounce period. Although non-linear magnetospheric amplification intrinsically involves perturbation of particle trajectories, pitch angle scattering is a more general phenomenon driven by both ducted and non-ducted waves in the magnetosphere. We thus consider electron precipitation in the context of HAARP generated ELF/VLF waves that propagate in ducts and are amplified, as well as non-ducted and unamplified signals. The conduct of controlled electron precipitation experiments is relevant in the context of the possible use of man-made waves to mitigate increased radiation

belt fluxes that are known to be harmful to space assets [*Inan et al.*, 2003]. Although to date no conclusive evidence of HAARP induced electron precipitation has been found, the theoretical predictions and experimental trials presented in this chapter provide a valuable assessment of current capabilities and a foundation for future work.

6.1 Experiment Setup

Observation of particle precipitation poses a unique experimental challenge. Because of the high density of the lower atmosphere, direct detection of energetic particles from the magnetosphere requires the placement of detectors at significant altitudes. Satellites have been used to detect precipitation induced by both ground based transmitters [*Imhof et al.*, 1983a,b] and lightning [*Inan et al.*, 2007a]. However, particle detectors on satellites must have high sensitivity and angular resolution in order to resolve small fluctuations of fluxes near the loss cone. Unfortunately, many satellites do not have sensitive detectors since these instruments are often designed to observe the very intense and energetic fluxes in the auroral regions.[1] Another difficulty in satellite detections of precipitation is spacecraft motion, which limits the duration of observations for a terrestrial wave injection experiment at a fixed location. Indirect approaches to detection of precipitation are based on observing the effects of energetic particles impinging onto the atmosphere. Mounting detectors on balloons has proven successful in detecting x-rays produced by precipitating electrons associated with natural magnetospheric emissions [*Rosenberg*, 1981; *Rosenberg et al.*, 1981]. Optical emissions resulting from precipitating electrons have been detected using photometers and *Helliwell et al.* [1980b] report optical signatures associated with natural VLF emissions in the 2−4 kHz band near Siple Station. However, detection of precipitation induced x-rays or optical emissions is impeded by a high background noise level and relatively weak signatures of precipitation events. The results of *Rosenberg* [1981], *Rosenberg et al.* [1981], and *Helliwell et al.* [1980b] are relatively rare observations resulting from unusually intense natural VLF waves (chorus emissions) and

[1] In this regard the DEMETER satellite is a rare exception as its high aperture particle detector was designed primarily for investigations at low latitudes.

associated high precipitation fluxes. It is thus unlikely that precipitation induced by the HAARP facility, with unamplified radiated ELF/VLF power of ∼100 W [*Platino et al.*, 2006; *Moore et al.*, 2007], will be observable using x-ray or optical detection techniques.

An alternate method for detecting energetic particle precipitation is by observing effects of the precipitation on the electromagnetic properties of the ionosphere. Density changes in the ionosphere due to particle precipitation change the electrical conductivity and thus affect the propagation properties of the Earth ionosphere waveguide. Changes in the Earth ionosphere waveguide in turn change the amplitude and phase of VLF waves propagating therein. Sensing the ionosphere by monitoring the amplitude and phase of subionospherically propagating VLF signals is known as VLF remote sensing and in its most common form takes advantage of VLF signals from powerful navy communication transmitters in the 10−30 kHz band. This indirect method of observing precipitation is shown schematically in Figure 6.1 and has been used extensively to observe precipitation induced by lightning [*Peter and Inan*, 2007], natural magnetospheric emissions [*Dingle and Carpenter*, 1981], and ground based transmitters [*Inan et al.*, 2007b]. The high sensitivity of the VLF remote sensing method arises from the fact that VLF waves reflect from the D-region, where ambient electron densities are very low (∼100−1000 cm^{-3}), making even small density perturbations significant and detectable.

The map in Figure 6.2 shows a subset of the web of VLF transmitter paths to various Alaska receiver sites. For clarity only the paths from the two nearest transmitters of NLK in Washington and NPM in Hawaii are shown, although the signals from more distant transmitters such as NAA in Maine, NWC in Australia, and NLM in North Dakota are also observed. The VLF remote sensing technique is most sensitive to precipitating electrons in the 100−300 keV energy range, which deposit their energy (thus creating secondary ionization) near or immediately below the nighttime VLF reflection height of ∼85 km [*Carpenter et al.*, 1997]. For transient bursts of electron precipitation a key feature of the effect is a sharp change in observed amplitude and phase of the VLF transmitter signal at the onset of precipitation followed by a slow recovery to ambient conditions on the order of seconds to tens of seconds. It

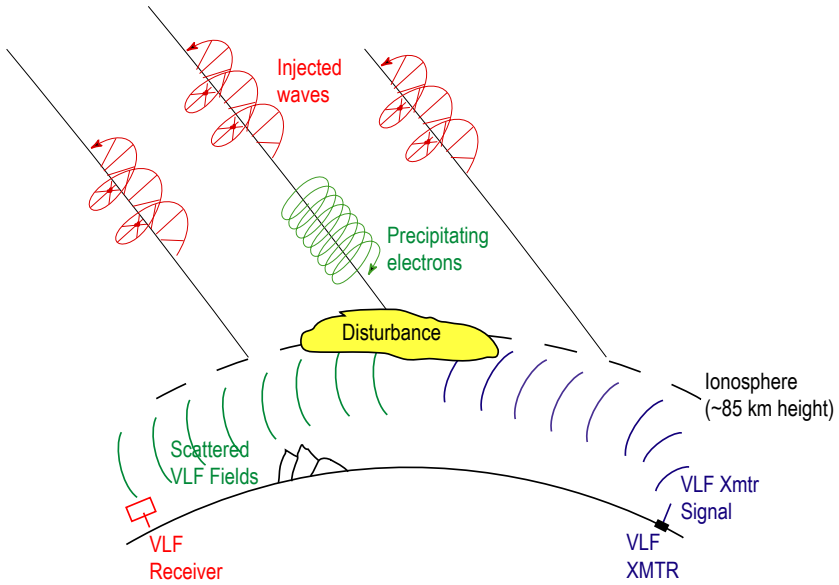

Figure 6.1: Concept of using subionospherically propagating VLF signals to detect an ionospheric disturbance induced by energetic particle precipitation.

is important to note that the VLF remote sensing technique only detects changes in ionospheric conductivity. For a controlled precipitation experiment it is thus necessary to induce a transient effect since the VLF amplitude and phase response to a steady stream of precipitation would be difficult or perhaps impossible to detect. In the simplest case, an ON/OFF condition for the precipitation inducing radiation is used. Unlike precipitation induced by lightning which is readily observed for individual events, the effect of precipitation induced by HAARP ELF/VLF signals and other man-made sources is bound to produce a much weaker signature. For this reason repetitive formats are employed to allow the detection of a weak signature using Fourier analysis. Repetitive transmission formats were used by *Inan et al.* [2007b] to detect precipitation induced by the NPM transmitter using the VLF remote sensing technique. Many of the formats utilized in HAARP precipitation experiments were inspired by the NPM controlled precipitation experiment.

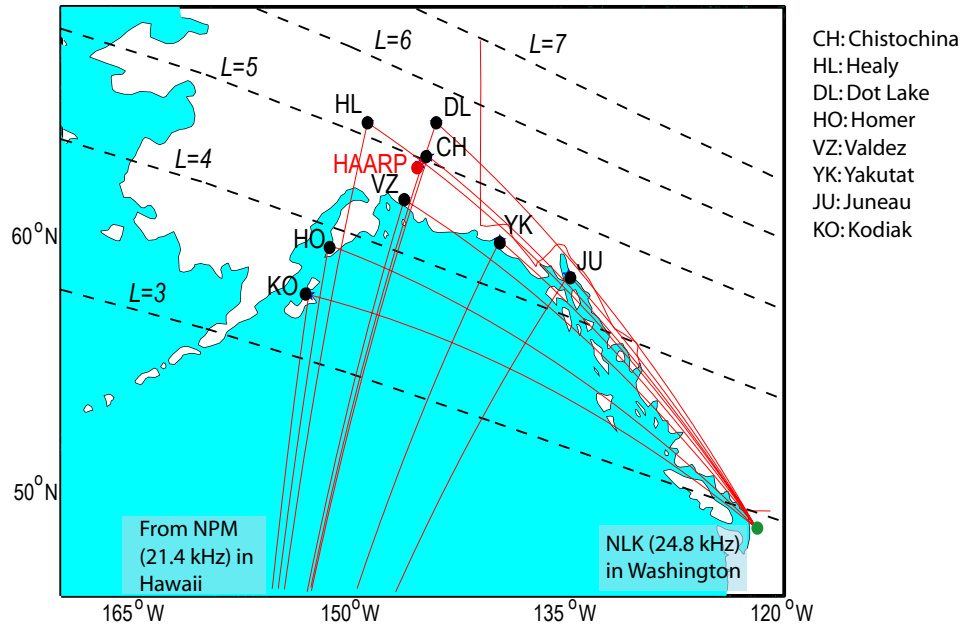

Figure 6.2: Map showing subset of VLF transmitter paths to Alaska receiver sites.

6.2 Theoretical Predictions

The equations that govern pitch angle scattering of energetic electrons by whistler mode waves closely resemble Equations (4.3)−(4.6) which are for the special case of interactions with ducted waves. As mentioned above, precipitation can be induced by both ducted and non-ducted waves. Ducted and magnetospherically amplified waves have the potential to be more effective at pitch angle scattering because of their higher amplitude. HAARP induced ELF/VLF radiation is on the order of only ∼100 W [*Platino et al.*, 2006; *Moore et al.*, 2007], making it several orders of magnitude lower than radiation from lightning or navy communication transmitters that has been observed to precipitate electrons. It is thus possible that HAARP generated ELF/VLF signals would not be able to precipitate detectable fluxes of energetic particles without ∼10−20 dB of magnetospheric amplification. As was discussed in Chapters 2 and 3, non-linear amplification of HAARP induced ELF/VLF signals is observed only during a small fraction of transmissions and requires the presence

of ducts near the heating facility. On the other hand, HAARP induced ELF/VLF waves are expected to regularly propagate in the magnetosphere in the non-ducted mode. Non-ducted ELF/VLF signals induced by HAARP were observed at altitudes of ∼26,000 km on board the CLUSTER spacecraft [*Platino et al.*, 2004]. The HAARP signals observed on CLUSTER were interpreted to have undergone coupling from whistler mode waves to quasi-electrostatic lower hybrid waves through scattering mechanisms discussed by *Bell and Ngo* [1990]. Such electrostatic waves are also believed to precipitate energetic particles through resonant interactions [*Lyons et al.*, 1972; *Bell and Ngo*, 1988]. It is thus worthwhile to consider precipitation induced by non-ducted unamplified HAARP induced ELF/VLF waves despite the weak amplitudes of these signals. While the precipitation fluxes induced by ducted waves impinge on the ionosphere largely at the duct endpoint, the location of non-ducted precipitation fluxes relative to their injection point is dependent upon the deposition of whistler mode raypaths. Non-ducted waves spread into the magnetosphere and tracking their trajectories requires numerical ray tracing techniques. A simulation of non-ducted HAARP induced precipitation was performed taking advantage of existing propagation and pitch angle scattering models [*Bortnik et al.*, 2006] and is described below.

Propagation in the magnetosphere is modeled using the Stanford Ray Tracing Code [*Inan and Bell*, 1977] with the input power distribution based on DEMETER satellite observations [*Piddyachiy et al.*, 2008]. The excitation pattern can be seen in the upper right panel of Figure 6.3 and exhibits the narrow 'column' geometry discussed in Chapter 3. The precipitation of energetic electrons is calculated from the wave trajectories using the method of *Bortnik et al.* [2006] with an energetic electron distribution (with square pitch angle distribution) based on measurements from the POLAR spacecraft [*Bell et al.*, 2002]. The output of the precipitation calculation is the particle flux onto the ionosphere.

Figure 6.3 shows the expected magnetospheric wave trajectories and incident particle precipitation on the ionosphere for a 3-second 500 Hz pulse. The initial particle fluxes impinge on the ionosphere equatorward of the HAARP facility. As the

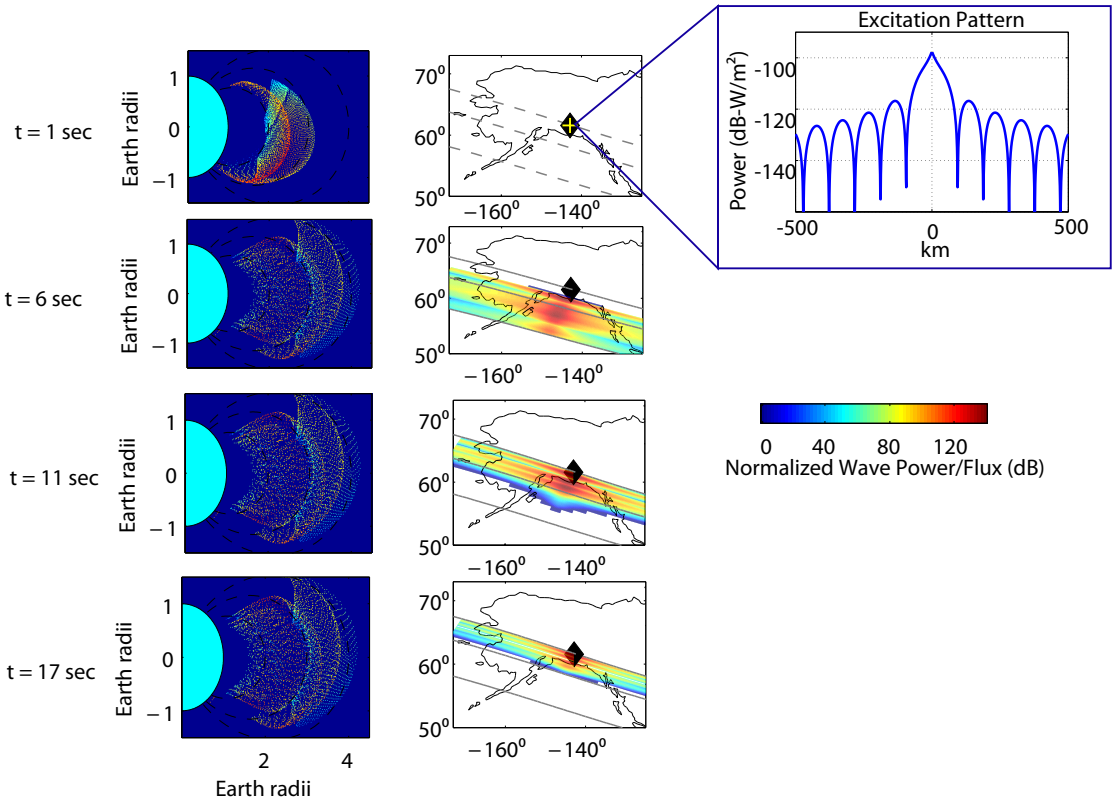

Figure 6.3: Predicted wave trajectories and precipitation flux from 500 Hz 3-second pulses with excitation pattern shown in upper right panel. A 500 Hz 3-second pulse is launched at $t = 0$.

waves magnetospherically reflect and begin to fill the magnetosphere, the precipitation fluxes move northward, eventually reaching the latitude of the HAARP facility although only ∼15 seconds after the original transmission.

The simulation results predict that the VLF transmitter paths most affected by non-ducted precipitation are those that pass about 150−200 km south of HAARP. This result makes the NLK to Valdez and NLK to Homer paths the most sensitive to precipitation induced by HAARP generated non-ducted waves. On the other hand, the magnetospheric path determination for ducted and amplified waves discussed in Section 3.2 suggests precipitation from amplified waves would occur directly above the heating facility. Therefore, the transmitter paths most sensitive to precipitation

induced by ducted and amplified waves are NPM to Dot Lake and NLK to Healy.

6.3 Effect of HF Heating

The initial transmission formats designed for detection of HAARP induced precipitation involved repetitive ON/OFF keying of ELF/VLF signals. During the OFF time the HAARP facility would simply not radiate HF power. Soon after it was discovered that the ionospheric disturbance of HF heating versus non-heating [see *Bell et al.*, 1995] is the dominant effect observed on the subionospheric VLF transmitter signals. This effect complicates the detection scheme since the heating and precipitation periodicities are the same and any ionospheric perturbation resulting from precipitation is drowned out by the stronger heating effect. While it was expected that the heating effect might be dominant for transmitter propagation paths that traverse directly under the heated region, the effect was also observed for paths that passed up to 150 km away from the HAARP facility. The close-up map in Figure 6.4 shows the physical scale of the HF heated region for 3.2 MHz and 5.8 MHz carrier frequencies. Most of the precipitation experiments discussed here were conducted before the 2007 HAARP upgrade so the beam sizes correspond to the original 960 kW array. The size of the 3.2 MHz beam can be seen to extend all the way to the Chistochina (CH) receiving station.

Figure 6.5 shows the results of an almost 3 hour transmission of ELF/VLF pulses with 10 second periodicity (5 seconds ON, 5 seconds OFF) conducted in December 2005. The transmission format with corresponding full ON/OFF cycling of HF power is illustrated in panel (e). The HF frequency utilized for the experiment was 3.25 MHz. Panels (a) and (b) show the frequency spectra of the amplitude and phase of the NPM transmitter to Dot Lake (DL), panels (c) and (d) show the same for the NLK transmitter, and panels (f) and (g) show the superposed epochs of the amplitude of both transmitters. The observed amplitude and phase of both transmitters exhibit the 10 second periodicity (0.1 Hz) of the HAARP transmission format. During this time, the 0.1 Hz periodicity was also observed in the amplitude and phase of all transmitter signals observed at Chistochina. Since a periodicity corresponding to the modulation

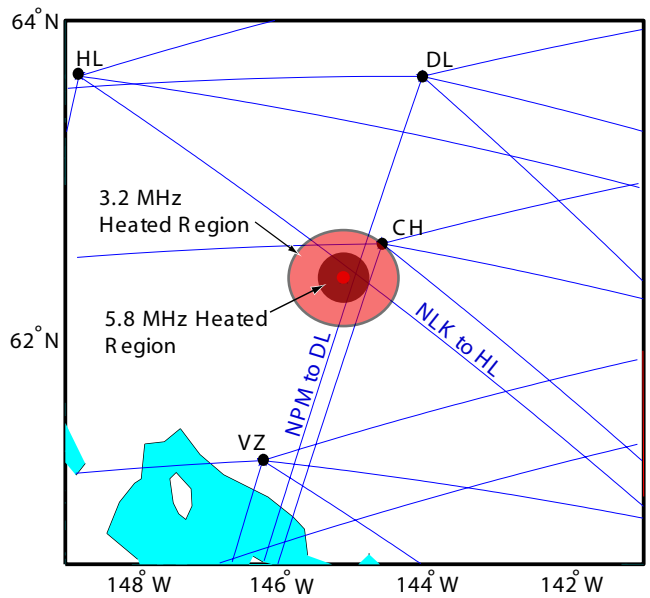

Figure 6.4: HAARP HF heated regions in relation to VLF transmitter propagation paths.

periodicity could result from either precipitation or heating, it is necessary to examine the signal in the time domain in order to distinguish between the two effects. Heating and cooling time scales in the ionosphere are on the order of milliseconds; ionospheric recovery times from precipitation induced secondary ionization are on the order of tens to hundreds of seconds [*Pasko and Inan*, 1994]. Thus while heating induced perturbations in subionospherically propagating VLF signals should be in (ON−OFF) sync with the heating signal, perturbations from precipitation will exhibit a delayed exponential recovery. The superposed epoch of the NPM transmitter amplitude in panel (f) of Figure 6.5 exhibits a square wave shape characteristic of a heating induced perturbation and is similar to the results of *Bell et al.* [1995] who examined VLF heating signatures induced by the HIPAS heater. The superposed epoch for the NLK transmitter amplitude shown in panel (g) is more noisy but is interpreted to also result primarily from heating and not precipitation. It is not surprising that all transmitter paths to Chistochina and the NPM path to Dot Lake are strongly affected by heating.

As can be seen from the map in Figure 6.4, the 3.25 MHz heating area extends out to the Chistochina receiver and the NPM to Dot Lake path passes directly over the facility. However, the observation of a heating signature on the NLK to Dot Lake path, which at its nearest point, is 150 km from the HAARP facility suggests significant scattering from the heated region, yielding reception of multiple propagation paths at Dot Lake. It is worthy to note that *Bell et al.* [1995] only found evidence of heating signatures on paths within 20 km of the HIPAS facility. The contrasting detection of heating signatures at a 150 km distance found here could be due to the higher power of the HAARP facility as compared to HIPAS or the specific transmitter path geometries involved.

6.4 Mitigation of HF Heating

Since the presence of a strong heating signature on the VLF remote sensing paths in the vicinity of the HAARP facility precludes the detection of particle precipitation, efforts were taken to mitigate this effect with special transmission formats. Instead of creating ELF/VLF periodicity by directly turning the HF beam ON and OFF, it was decided to leave HF power continuously ON and impose ELF/VLF periodicity solely through changes in modulation. Keeping HF average power constant should remove the heating induced ionospheric perturbations. For square wave amplitude modulation constant average HF power can be achieved by changing the HF signal to CW at 50% power during ELF/VLF 'OFF' periods. The transmission scheme for this second experiment is illustrated in panels (a) and (b) of Figure 6.6. In addition to modifying the HF power as mentioned above, the even and odd minutes were alternated between pulses and frequency-time ramps and the overall periodicity was changed to 12 seconds. Since the pitch angle scattering equations that drive precipitation are dependent on the ELF/VLF wave frequency, any observable differences between the even and odd minutes would likely be evidence of a precipitation effect.

Sustaining HF power at 50% during modulation OFF times was effective in reducing ionospheric heating effects. No 12 second periodicity was observed on any transmitter paths at Chistochina nor on any transmitter paths that did not traverse

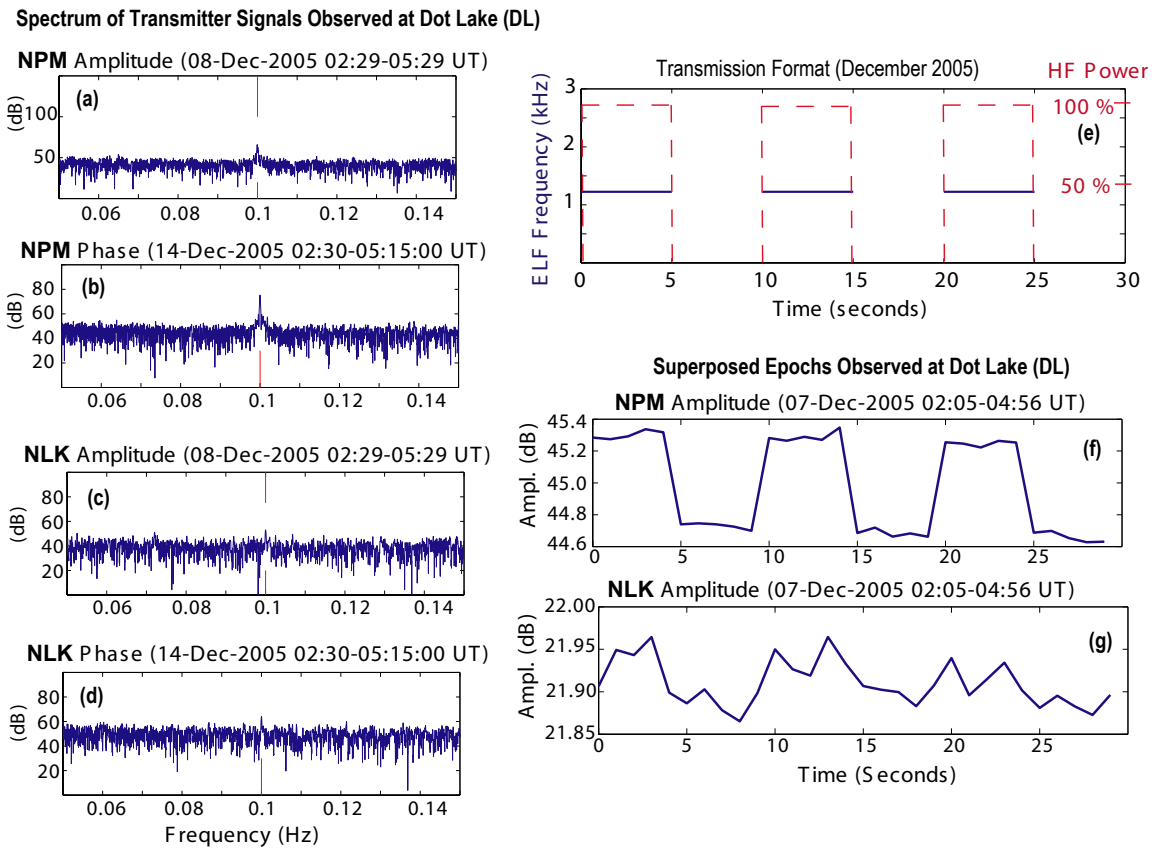

Figure 6.5: Effect of HF Heating observed in initial precipitation experiment. The transmission format is shown in panel (e). Frequency spectra of amplitude and phase of the NPM and NLK transmitters observed at Dot Lake are shown in panels (a)-(d). Panels (f) and (g) shows time domain superposed epochs of observed amplitude.

directly under the heated region. The heating effect was reduced to propagation paths only directly under the heated region, suggesting that periodic scattering from the heated area had been effectively reduced. The localized effect of the HF heated region on subionospheric paths can be seen in the results in panels (c) and (d) of Figure 6.6 which show spectra of amplitude data of the NLK transmitter observed at Healy (HL). For the transmission utilizing a 5.8 MHz carrier frequency, yielding a smaller beam size, no periodicity is observed. However, when the HF carrier is changed to 3.2 MHz, half an hour later on the same day, the 12 second periodicity is observed. The larger beam of the 3.2 MHz carrier perturbs the subionospheric VLF signal while

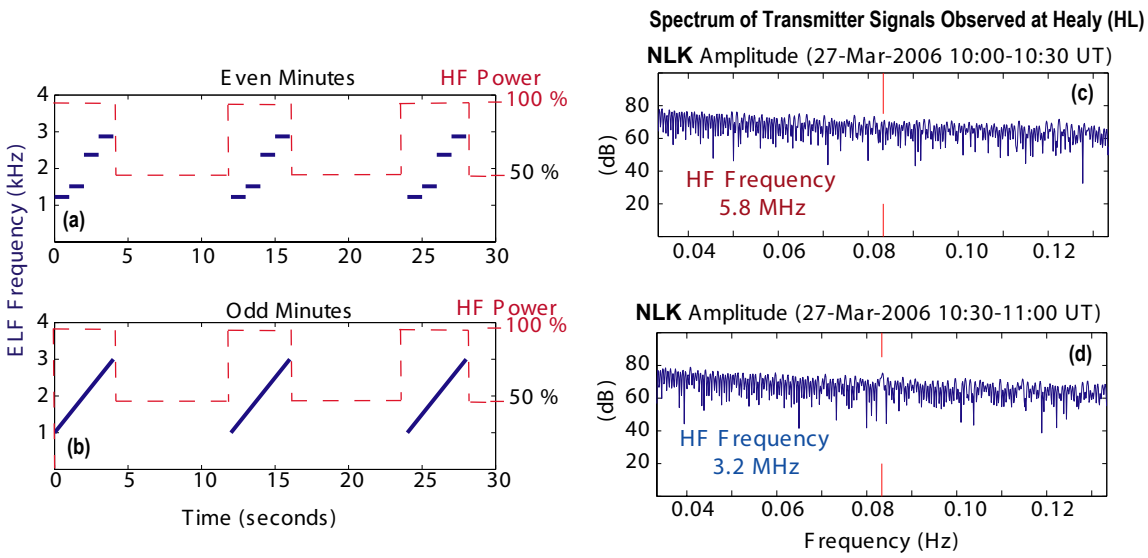

Figure 6.6: Transmission format for mitigating heating effect with 12 second periodicity but constant average HF power shown in panels (a) and (b). Spectrum of NLK amplitude observed at Healy showing periodicity for 3.2 MHz carrier frequency (panel (d)) but not the 5.8 MHz carrier frequency (panel(c)).

the smaller 5.8 MHz beam does not. The sensitivity to the beam size as a function of HF carrier is in sharp contrast to the original unmitigated transmissions where the heating effect was observed on paths within a ∼150 km radius of the heated region.

6.5 Ionospheric Effect of ELF/VLF Modulation Frequency

Another approach to detection of controlled precipitation is to transmit ELF/VLF waves constantly, albeit with a periodic format. Although such a scheme is bound to have a weaker periodic signature than an ON/OFF approach, for ducted and amplified waves in particular, the specifics of the frequency-time format can affect the wave amplitude and hence the precipitation fluxes. Figure 6.7 shows an example where the 10 second periodicity of the ELF/VLF format was distinctly observed on the NLK to Healy path. This record was very closely scrutinized since it was

recorded during simultaneous observation of 1-hop and 2-hop echoes thus suggesting the possibility of precipitation caused by amplified and triggered signals directly over the heating facility. However, examination of the time domain shows this not to be the case. The bottom panel in Figure 6.7 shows superposed epochs which are seen to directly correspond in time to the transmission format. There is no delayed ionospheric recovery as would be expected for a precipitation signature. It thus appears that even the smallest changes in modulation frequency, which are expected to have only a minor second order effect on the ionosphere, influence the subionospheric paths directly under the heated region. While this is a testament to the sensitivity of the VLF remote sensing technique in detecting ionospheric perturbations, in the present context it severely limits our ability to detect precipitation occurring directly above the heating facility.

6.6 Summary and Future Work

To date no conclusive evidence of HAARP induced electron precipitation has been found using the VLF remote sensing technique. Detecting precipitation directly over the heating facility is encumbered by ionospheric perturbations caused by HAARP ELF/VLF generation. Even small changes in modulation frequency affect the amplitude and phase of subionospherically propagating signals. Mitigating the heating effect by transmitting constant average HF power allows for employment of the VLF remote sensing technique in the vicinity of the HAARP heater at a minimum distance of $\sim$35 km for typical HF frequencies.

Precipitation induced by non-ducted waves is predicted to be incident on the ionosphere $\sim 150-200$ km south of the HAARP facility. Non-ducted precipitation has a wide geographical extent and significant time lag due to effects of magnetospheric reflections. More effective detection of non-ducted precipitation could be achieved by matching the transmission format to the expected ionospheric perturbation time scales for a specific transmitter-receiver configuration. Such a format is based on treating the magnetosphere-ionosphere system as a matched filter that can yield a maximum response for an appropriate input.

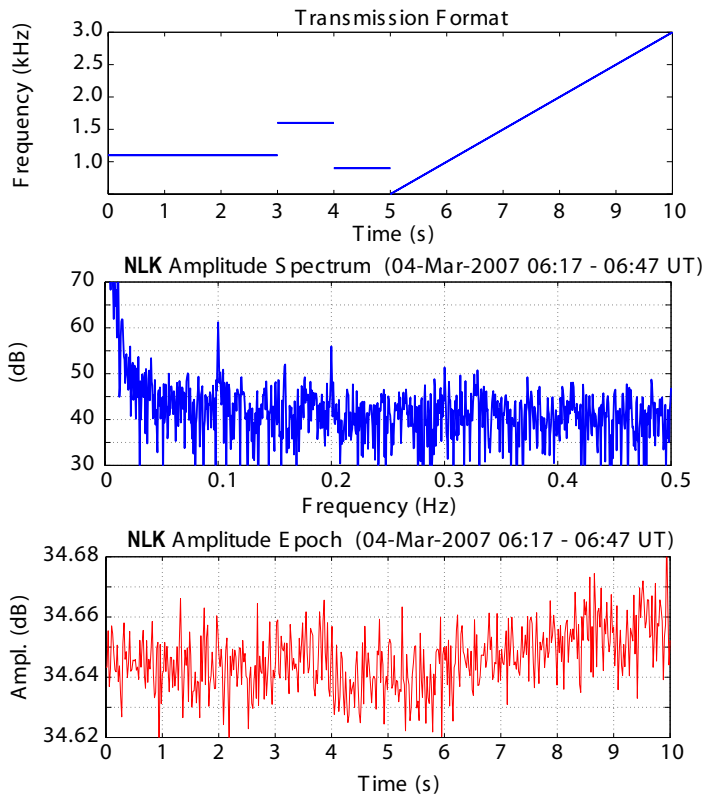

Figure 6.7: Transmission format with no 'OFF' time but 10 second periodicity shown in top panel. The middle panel shows the spectrum of the NLK amplitude observed at Healy which exhibits the 10 second periodicity. The bottom panel shows the superposed epochs of the NLK amplitude.

Chapter 7

Summary and Suggestions for Future Work

7.1 Summary of Contributions

Several years of experiments illustrate the effectiveness of using the HAARP HF facility for magnetospheric wave injection experiments. Observations of magnetospheric echoes at the conjugate point and in the northern hemisphere as well as on board the DEMETER satellite testify to the excitation of magnetospheric amplification and triggering of emissions by HAARP generated ELF/VLF signals. The variability of the magnetospheric response to both the frequency band and the frequency time format of the injected signals illustrate the need for near-real-time monitoring of the experiment. The ability to change the transmission format on minute time scales is necessary for ensuring successful observations. These requirements can be met with the current HAARP facility and the constructed Stanford Alaska VLF network. It is found that HAARP induced triggered emissions occur primarily inside the plasmapause and are thus associated with quiet magnetospheric conditions. Observations of whistler mode echoes do not coincide with the strongest ELF/VLF generated amplitudes, and the input amplitude as observed on the ground is found to be significant only on the multi-minute time scales of a single observation period. Dispersion analysis indicates that the signals yielding amplified echoes are injected into the magnetosphere directly

above the HF heater, in agreement with satellite observations and numerical models that show the highest amplitudes of the HAARP induced ELF/VLF dipole to be confined to a narrow vertical column with a diameter on the scale of the heated region. The narrow column radiation geometry is most likely responsible for the sensitivity of echo observations to available ducts, as is suggested by experimental evidence involving spatially varying the position of the HAARP induced ELF/VLF dipole.

Measurements of the amplitude and phase of the observed amplified signals allow for the comparison of the observations with theoretical formulations and numerical models. In the determination of the average non-linear resonant current vector directly from observations it is found that the observations agree with theoretical and numerical predictions. In particular the joint evolution of observed amplitude and phase of magnetospheric echoes is verified and the effect of variable input amplitude is also in agreement with numerical sensitivity studies. Characterization of the non-linear current vector from the observed amplitude and phase allows for insight into the evolution of the magnetospheric hot plasma distribution.

In the course of the experimental observations a new phenomena of cross modulation between whistler mode signals and HF heating was discovered. The concept was investigated as a new method of generating signals with an HF heater. ELF/VLF signals using the new technique are readily detected, including frequencies greater than the 30 kHz modulation upper limit of the HAARP array. However, the signals generated with this technique are found to be about an order of magnitude weaker than those generated with conventional amplitude modulation.

Although to date no direct evidence of HAARP induced electron precipitation has been found, the VLF remote sensing technique is suitable for continued experimental trials. Ray tracing and particle scattering codes predict precipitation resulting from non-ducted HAARP ELF/VLF waves to be incident several hundred kilometers south of the HAARP array. Detection of precipitation in the vicinity of the HAARP facility is possible if the ionospheric perturbation from HF heating is mitigated by radiating a constant average HF power.

7.2 Suggestions for Future Work

An overarching goal of the HAARP wave injection program is to understand the conditions and mechanisms that lead to wave amplification. In addition to continuing wave injection experiments in their present form to build a statistical data base, special targeted investigations are also recommended. In the work presented here and in the Siple Station experiments coherent waves were used to probe the magnetosphere and trigger amplification. It is possible to take advantage of the flexibility of the HAARP facility to investigate the coherence limits of the wave particle interaction that drives non-linear growth. Incoherent 'noise' packets of varying bandwidths can be modulated and transmitted at ELF/VLF frequencies that are observed to yield amplification. The amplification of such signals, which likely depends on the input bandwidth, should provide greater insight into the evolution of the hot plasma distribution during the wave-particle interaction.

Since the availability of and coupling into magnetospheric ducts has been shown to be a key factor, it is feasible to attempt to use the HAARP array to generate ducts. Creating ducts on demand has the potential to greatly increase the utility of the HAARP facility in magnetospheric probing. Although the use of an HF heating facility to create a duct is seen as being theoretically feasible, finding convincing evidence of a HAARP created duct will be difficult and likely will need to be addressed with long term statistics.

A concerted effort should be made to match fine features of observations with output of numerical models using realistic inputs. In particular the dynamics of observed amplitude and phase of whistler mode echoes should be reproduced numerically to infer the possible hot plasma distribution and its evolution. The GIB model [*Gibby et al.*, 2008; *Gibby*, 2008] and VHS code [*Nunn*, 1993] are both well suited to such a study since both models are not computationally expensive and allow for trial and error repetitive runs on practically feasible time scales. The specifics of the hot plasma distribution remain one of the key unknowns in studies of the magnetosphere and using detailed observations to derive accurate parameters for existing models can shed much light on the issue.

Appendix A

Derivation of the Wave Update

This appendix provides a detailed derivation of the wave evolution equation for whistler mode waves in the presence of a resonant current. The discussion is largely reproduced from *Gibby* [2008] which follows the derivation provided by *Nunn* [1974], which was modified for the MKS system and clarified by *Omura and Matsumoto* [1982].

The derivation begins by linearizing the parameters of interest. For example, the total magnetic field in the plasma $\widetilde{\mathbf{B}}$ is divided into two components, a static component $\mathbf{B}_0$ and a small varying component $\widetilde{\mathbf{B}}_{\mathrm{w}}$ due to the action of the whistler mode wave. The total electric field and electron velocities are similarly decomposed,

$$\begin{aligned} \widetilde{\mathbf{B}} &= \mathbf{B}_0 + \widetilde{\mathbf{B}}_{\mathrm{w}} & \mathbf{B}_0 &>> \widetilde{\mathbf{B}}_{\mathrm{w}} \\ \widetilde{\mathbf{E}} &= \mathbf{E}_0 + \widetilde{\mathbf{E}}_{\mathrm{w}} & \mathbf{E}_0 &\simeq 0 \\ \widetilde{\mathbf{v}} &= \mathbf{v}_0 + \widetilde{\mathbf{v}}_{\mathrm{w}} & \mathbf{v}_0 &\simeq 0 \end{aligned} \tag{A.1}$$

where additional assumptions have been noted. Specifically, the wave magnetic field is small compared to the static magnetic field, the plasma is not influenced by any static electric fields, and there is no bulk motion of the electrons.

Starting with the Lorentz force, applying the linearized quantities with the assumptions from Equation (A.1) yields,

$$\begin{aligned} m_{\mathrm{e}}\frac{d\widetilde{\mathbf{v}}}{dt} &= -q\left(\widetilde{\mathbf{E}} + \widetilde{\mathbf{v}} \times \widetilde{\mathbf{B}}\right) \\ \frac{d\widetilde{\mathbf{v}}_{\mathrm{w}}}{dt} &= -\frac{q}{m_{\mathrm{e}}}\widetilde{\mathbf{E}}_{\mathrm{w}} - \frac{q}{m_{\mathrm{e}}}\left(\widetilde{\mathbf{v}}_{\mathrm{w}} \times \mathbf{B}_0\right) \end{aligned} \tag{A.2}$$

where m_{e} is the rest mass of the electron and q is the fundamental charge.

The z direction is defined to be along the static magnetic field. That is, $\mathbf{B}_0 = B_0\hat{\boldsymbol{z}}$, where $\hat{\boldsymbol{z}}$ is the unit vector in the z direction. Since the direction of wave propagation is only in that direction, $\mathbf{k} = k\hat{\boldsymbol{z}}$. Similarly, the variation in the wave quantities is only transverse to the static magnetic field, allowing Equation (A.2) to be reduced to two dimensions transverse to $\hat{\boldsymbol{z}}$. Assuming that time varying quantities can be expressed in the form $e^{-i\omega t}$, and using the definition of the gyrofrequency, $\omega_{\mathrm{c}} = qB_0/m_{\mathrm{e}}$, Equation (A.2) becomes

$$\begin{bmatrix} -i\omega & \omega_{\mathrm{c}} \\ -\omega_{\mathrm{c}} & -i\omega \end{bmatrix} \widetilde{\mathbf{v}}_{\mathrm{w}} = -\frac{q}{m_{\mathrm{e}}}\widetilde{\mathbf{E}}_{\mathrm{w}} \tag{A.3}$$

in a rectangular coordinate system.

The current carried by the cold electrons, $\widetilde{\mathbf{J}}_{\mathrm{c}}$, and the conductivity tensor $\overleftrightarrow{\boldsymbol{\sigma}}$ are defined by

$$\widetilde{\mathbf{J}}_{\mathrm{c}} = -n_{\mathrm{c}}q\widetilde{\mathbf{v}}_{\mathrm{w}} = \overleftrightarrow{\boldsymbol{\sigma}}\widetilde{\mathbf{E}}_{\mathrm{w}} \tag{A.4}$$

where n_{c} is the number density of the cold electrons. By inspection of Equation (A.3), the conductvity tensor is

$$\overleftrightarrow{\boldsymbol{\sigma}} = \omega_{\mathrm{p}}^2\epsilon_0 \begin{bmatrix} \dfrac{-i\omega}{\omega_{\mathrm{c}}^2 - \omega^2} & \dfrac{-\omega_{\mathrm{c}}}{\omega_{\mathrm{c}}^2 - \omega^2} \\ \dfrac{\omega_{\mathrm{c}}}{\omega_{\mathrm{c}}^2 - \omega^2} & \dfrac{-i\omega}{\omega_{\mathrm{c}}^2 - \omega^2} \end{bmatrix} \tag{A.5}$$

where the plasma frequency ω_{p} is defined by

$$\omega_{\mathrm{p}}^2 = \frac{n_{\mathrm{c}} q^2}{m_{\mathrm{e}} \epsilon_0}.$$

If we now recall Faraday's law and Ampere's law, where the displacement current is neglected due to the slow-wave nature of the medium,

$$i\frac{\partial \widetilde{\mathbf{E}}_{\mathrm{w}}}{\partial z} = -\frac{\partial \widetilde{\mathbf{B}}_{\mathrm{w}}}{\partial t} \tag{A.6}$$

$$i\frac{\partial \widetilde{\mathbf{B}}_{\mathrm{w}}}{\partial z} = \mu_0 \left(\widetilde{\mathbf{J}}_{\mathrm{c}} + \widetilde{\mathbf{J}}_{\mathrm{R}}\right) \tag{A.7}$$

where the current has been divided into a term representing the current carried by the whistler mode wave in the cold electrons $\widetilde{\mathbf{J}}_{\mathrm{c}}$ and the resonant current created by the interaction with the near-resonant electrons J_{R}.

From Equation (A.2) and Equation (A.4), an expression for the cold current in terms of the wave electric field can be obtained,

$$\frac{\partial \widetilde{\mathbf{J}}_{\mathrm{c}}}{\partial t} + i\omega_c \widetilde{\mathbf{J}}_{\mathrm{c}} = \omega_{\mathrm{p}}^2 \epsilon_0 \widetilde{\mathbf{E}}_{\mathrm{w}} \tag{A.8}$$

Combining Equation (A.6), Equation (A.7) and Equation (A.8) to eliminate $\widetilde{\mathbf{E}}_{\mathrm{w}}$ and $\widetilde{\mathbf{J}}_{\mathrm{c}}$, and assuming that the variation of the inhomogeneous medium is small on the scales of a wavelength, i.e.

$$\left|\frac{\partial \omega_{\mathrm{c}}}{\partial z}\right| \ll k\left(\omega_{\mathrm{c}} - \omega\right)$$

$$\left|\frac{\partial \omega_{\mathrm{p}}}{\partial z}\right| \ll k\omega_{\mathrm{p}}^2$$

yields

$$\left[\frac{\partial}{\partial z}\left(\frac{\partial}{\partial t} + i\omega_{\mathrm{c}}\right)\frac{\partial}{\partial z} - \frac{\omega_{\mathrm{p}}^2}{c^2}\frac{\partial}{\partial t}\right]\widetilde{\mathbf{B}}_{\mathrm{w}} = -i\mu_0\left(\frac{\partial}{\partial t} + i\omega_{\mathrm{c}}\right)\frac{\partial}{\partial z}\widetilde{\mathbf{J}}_{\mathrm{R}} \tag{A.9}$$

The wave magnetic field and the resonant current are then exressed as

$$\widetilde{\mathbf{B}}_{\mathrm{w}} = B_{\mathrm{w}} e^{i\left(\phi - \omega t + \int_{z_0}^{z} k dz'\right)}$$

$$\widetilde{\mathbf{J}}_{\mathrm{R}} = J_{\mathrm{R}} e^{i\left(\psi + \phi - \omega t + \int_{z_0}^{z} k dz'\right)}$$

where ϕ is the phase variation of the wave field with the rapid phase variation due to the temporal varation of the wave ω and the spatial variation of the wave k removed. That is, ϕ represents the additional phase accumulated due to the instability. The term ψ represents the phase of the current relative to the wave phase, or the angle between the current vector and the wave magnetic field vector. Expanding the right side and left sides of Equation (A.9) yields

$$\begin{aligned} -i\mu_0 \left(\frac{\partial}{\partial t} + i\omega_c\right) \frac{\partial}{\partial z} \widetilde{\mathbf{J}}_{\mathrm{R}} = -i\mu_0 J_{\mathrm{R}} e^{i\left(\psi + \phi - \omega t + \int_{z_0}^{z} k dz'\right)} \cdot \\ \left\{ -\left(\omega_{\mathrm{c}} - \omega + \frac{\partial \phi}{\partial t} + \frac{\partial \psi}{\partial t}\right)\left(k + \frac{\partial \phi}{\partial z} + \frac{\partial \psi}{\partial z}\right) + \frac{1}{J_{\mathrm{R}}} \frac{\partial^2 J_{\mathrm{R}}}{\partial t \partial z} \right. \\ + i\left[\left(\frac{\partial^2 \phi}{\partial t \partial z} + \frac{\partial^2 \psi}{\partial t \partial z}\right) + \frac{1}{J_{\mathrm{R}}} \frac{\partial J_{\mathrm{R}}}{\partial t}\left(k + \frac{\partial \phi}{\partial z} + \frac{\partial \psi}{\partial z}\right) \right. \\ \left. \left. + \frac{1}{J_{\mathrm{R}}} \frac{\partial J_{\mathrm{R}}}{\partial z}\left(\omega_{\mathrm{c}} - \omega + \frac{\partial \phi}{\partial t} + \frac{\partial \psi}{\partial t}\right)\right]\right\} \end{aligned} \tag{A.10}$$

and

$$\begin{aligned}
&\left[\frac{\partial}{\partial z}\left(\frac{\partial}{\partial t}+i\omega_{\mathrm{c}}\right)\frac{\partial}{\partial z}-\frac{\omega_{\mathrm{p}}^2}{c^2}\frac{\partial}{\partial t}\right]\widetilde{\mathbf{B}}_{\mathrm{w}}=e^{i\left(\phi-\omega t+\int_{z_0}^{z}k\,dz'\right)}\\
&\quad\Bigg(-\frac{\partial B_{\mathrm{w}}}{\partial t}\left[\left(k+\frac{\partial\phi}{\partial z}\right)^2+\frac{\omega_{\mathrm{p}}^2}{c^2}\right]-2\frac{\partial B_{\mathrm{w}}}{\partial z}\left(\omega_{\mathrm{c}}-\omega+\frac{\partial\phi}{\partial t}\right)\left(k+\frac{\partial\phi}{\partial z}\right)\\
&\qquad+B_{\mathrm{w}}\left[-2\left(k+\frac{\partial\phi}{\partial z}\right)\frac{\partial^2\phi}{\partial t\partial z}-\left(\omega_{\mathrm{c}}-\omega+\frac{\partial\phi}{\partial t}\right)\frac{\partial^2\phi}{\partial z^2}\right]\\
&\qquad-2\frac{\partial B_{\mathrm{w}}}{\partial t}\frac{\partial^2\phi}{\partial z^2}-2\frac{\partial B_{\mathrm{w}}}{\partial z}\frac{\partial^2\phi}{\partial t\partial z}+\frac{\partial^3 B_{\mathrm{w}}}{\partial t\partial z^2}\\
&\qquad+i\Bigg\{B_{\mathrm{w}}\left[-\left(k+\frac{\partial\phi}{\partial z}\right)^2\left(\omega_{\mathrm{c}}-\omega+\frac{\partial\phi}{\partial t}\right)+\frac{\omega_{\mathrm{p}}^2}{c^2}\left(-\omega+\frac{\partial\phi}{\partial t}\right)-\frac{\partial^3\phi}{\partial t\partial z^2}\right]\\
&\qquad\quad+2\left(k+\frac{\partial\phi}{\partial z}\right)\frac{\partial^2 B_{\mathrm{w}}}{\partial t\partial z}+\left(\omega_{\mathrm{c}}-\omega+\frac{\partial\phi}{\partial t}\right)\frac{\partial^2 B_{\mathrm{w}}}{\partial z^2}\Bigg\}\Bigg)
\end{aligned}\tag{A.11}$$

respectively. Combining Equation (A.10) and Equation (A.11), cancelling the phase

varation term and expanding the $J_{\mathrm{R}}e^{i\psi}$ term,

$$
\begin{aligned}
&-\frac{\partial B_{\mathrm{w}}}{\partial t}\left[\left(k+\frac{\partial\phi}{\partial z}\right)^2+\frac{\omega_{\mathrm{p}}^2}{c^2}\right]-2\frac{\partial B_{\mathrm{w}}}{\partial z}\left(\omega_{\mathrm{c}}-\omega+\frac{\partial\phi}{\partial t}\right)\left(k+\frac{\partial\phi}{\partial z}\right)\\
&+B_{\mathrm{w}}\left[-2\left(k+\frac{\partial\phi}{\partial z}\right)\frac{\partial^2\phi}{\partial t\partial z}-\left(\omega_{\mathrm{c}}-\omega+\frac{\partial\phi}{\partial t}\right)\frac{\partial^2\phi}{\partial z^2}\right]\\
&\qquad-2\frac{\partial B_{\mathrm{w}}}{\partial t}\frac{\partial^2\phi}{\partial z^2}-2\frac{\partial B_{\mathrm{w}}}{\partial z}\frac{\partial^2\phi}{\partial t\partial z}+\frac{\partial^3 B_{\mathrm{w}}}{\partial t\partial z^2}\\
&+i\Bigg\{B_{\mathrm{w}}\left[-\left(k+\frac{\partial\phi}{\partial z}\right)^2\left(\omega_{\mathrm{c}}-\omega+\frac{\partial\phi}{\partial t}\right)-\frac{\omega_{\mathrm{p}}^2}{c^2}\left(-\omega+\frac{\partial\phi}{\partial t}\right)-\frac{\partial^3\phi}{\partial t\partial z^2}\right]\\
&\qquad+2\left(k+\frac{\partial\phi}{\partial z}\right)\frac{\partial^2 B_{\mathrm{w}}}{\partial t\partial z}+\left(\omega_{\mathrm{c}}-\omega+\frac{\partial\phi}{\partial t}\right)\frac{\partial^2 B_{\mathrm{w}}}{\partial z^2}\Bigg\}\\
&\qquad=\mu_0 J_{\mathrm{R}}\left(\sin\psi-i\cos\psi\right)\cdot\\
&\qquad\quad\Bigg\{-\left(\omega_{\mathrm{c}}-\omega+\frac{\partial\phi}{\partial t}+\frac{\partial\psi}{\partial t}\right)\left(k+\frac{\partial\phi}{\partial z}+\frac{\partial\psi}{\partial z}\right)+\frac{1}{J_{\mathrm{R}}}\frac{\partial^2 J_{\mathrm{R}}}{\partial t\partial z}\\
&\qquad\qquad+i\Bigg[\left(\frac{\partial^2\phi}{\partial t\partial z}+\frac{\partial^2\psi}{\partial t\partial z}\right)+\frac{1}{J_{\mathrm{R}}}\frac{\partial J_{\mathrm{R}}}{\partial t}\left(k+\frac{\partial\phi}{\partial z}+\frac{\partial\psi}{\partial z}\right)\\
&\qquad\qquad\quad+\frac{1}{J_{\mathrm{R}}}\frac{\partial J_{\mathrm{R}}}{\partial z}\left(\omega_{\mathrm{c}}-\omega+\frac{\partial\phi}{\partial t}+\frac{\partial\psi}{\partial t}\right)\Bigg]\Bigg\}\\
&\qquad=\mu_0 J_{\mathrm{R}}\Bigg(\sin\psi\left[-\left(\omega_{\mathrm{c}}-\omega+\frac{\partial\phi}{\partial t}+\frac{\partial\psi}{\partial t}\right)\left(k+\frac{\partial\phi}{\partial z}+\frac{\partial\psi}{\partial z}\right)+\frac{1}{J_{\mathrm{R}}}\frac{\partial^2 J_{\mathrm{R}}}{\partial t\partial z}\right]\\
&\qquad\qquad+\cos\psi\Bigg[\left(\frac{\partial^2\phi}{\partial t\partial z}+\frac{\partial^2\psi}{\partial t\partial z}\right)+\frac{1}{J_{\mathrm{R}}}\frac{\partial J_{\mathrm{R}}}{\partial t}\left(k+\frac{\partial\phi}{\partial z}+\frac{\partial\psi}{\partial z}\right)\\
&\qquad\qquad\quad+\frac{1}{J_{\mathrm{R}}}\frac{\partial J_{\mathrm{R}}}{\partial z}\left(\omega_{\mathrm{c}}-\omega+\frac{\partial\phi}{\partial t}+\frac{\partial\psi}{\partial t}\right)\Bigg]\\
&\qquad\quad+i\Bigg\{\cos\psi\left[\left(\omega_{\mathrm{c}}-\omega+\frac{\partial\phi}{\partial t}+\frac{\partial\psi}{\partial t}\right)\left(k+\frac{\partial\phi}{\partial z}+\frac{\partial\psi}{\partial z}\right)-\frac{1}{J_{\mathrm{R}}}\frac{\partial^2 J_{\mathrm{R}}}{\partial t\partial z}\right]\\
&\qquad\qquad\sin\psi\Bigg[\left(\frac{\partial^2\phi}{\partial t\partial z}+\frac{\partial^2\psi}{\partial t\partial z}\right)+\frac{1}{J_{\mathrm{R}}}\frac{\partial J_{\mathrm{R}}}{\partial t}\left(k+\frac{\partial\phi}{\partial z}+\frac{\partial\psi}{\partial z}\right)\\
&\qquad\qquad\quad+\frac{1}{J_{\mathrm{R}}}\frac{\partial J_{\mathrm{R}}}{\partial z}\left(\omega_{\mathrm{c}}-\omega+\frac{\partial\phi}{\partial t}+\frac{\partial\psi}{\partial t}\right)\Bigg]\Bigg\}\Bigg)
\end{aligned}
\tag{A.12}
$$

Taking the real part of Equation (A.12),

$$
\begin{aligned}
&-\frac{\partial B_{\mathrm{w}}}{\partial t}\left[\left(k+\frac{\partial\phi}{\partial z}\right)^2+\frac{\omega_{\mathrm{p}}^2}{c^2}\right]-2\frac{\partial B_{\mathrm{w}}}{\partial z}\left(\omega_{\mathrm{c}}-\omega+\frac{\partial\phi}{\partial t}\right)\left(k+\frac{\partial\phi}{\partial z}\right)\\
&+B_{\mathrm{w}}\left[-2\left(k+\frac{\partial\phi}{\partial z}\right)\frac{\partial^2\phi}{\partial t\partial z}-\left(\omega_{\mathrm{c}}-\omega+\frac{\partial\phi}{\partial t}\right)\frac{\partial^2\phi}{\partial z^2}\right]\\
&\quad-2\frac{\partial B_{\mathrm{w}}}{\partial t}\frac{\partial^2\phi}{\partial z^2}-2\frac{\partial B_{\mathrm{w}}}{\partial z}\frac{\partial^2\phi}{\partial t\partial z}+\frac{\partial^3 B_{\mathrm{w}}}{\partial t\partial z^2}\\
&\quad=\mu_0 J_{\mathrm{R}}\Bigg\{\sin\psi\left[-\left(\omega_{\mathrm{c}}-\omega+\frac{\partial\phi}{\partial t}+\frac{\partial\psi}{\partial t}\right)\left(k+\frac{\partial\phi}{\partial z}+\frac{\partial\psi}{\partial z}\right)+\frac{1}{J_{\mathrm{R}}}\frac{\partial^2 J_{\mathrm{R}}}{\partial t\partial z}\right]\\
&\qquad+\cos\psi\Bigg[\left(\frac{\partial^2\phi}{\partial t\partial z}+\frac{\partial^2\psi}{\partial t\partial z}\right)+\frac{1}{J_{\mathrm{R}}}\frac{\partial J_{\mathrm{R}}}{\partial t}\left(k+\frac{\partial\phi}{\partial z}+\frac{\partial\psi}{\partial z}\right)\\
&\qquad\quad+\frac{1}{J_{\mathrm{R}}}\frac{\partial J_{\mathrm{R}}}{\partial z}\left(\omega_{\mathrm{c}}-\omega+\frac{\partial\phi}{\partial t}+\frac{\partial\psi}{\partial t}\right)\Bigg]\Bigg\}
\end{aligned}
\tag{A.13}
$$

At this point in the derivation, *Nunn* [1974] assumes that the wave is monochromatic. More explicitly, *Omura and Matsumoto* [1982] assume that the first order derivatives of J_{R} and ψ are negligible as well as all second and third order derivatives and the first order derivitives of ϕ on the right side of Equation (A.13), which gives

$$
\begin{aligned}
-\frac{\partial B_{\mathrm{w}}}{\partial t}\left(k^2+\frac{\omega_{\mathrm{p}}^2}{c^2}\right)-2k\left(\omega_{\mathrm{c}}-\omega\right)\frac{\partial B_{\mathrm{w}}}{\partial z}&=-\frac{\mu_0}{2}J_{\mathrm{R}}\sin\psi\left[2k\left(\omega_{\mathrm{c}}-\omega\right)\right]\\
\frac{\partial B_{\mathrm{w}}}{\partial t}+\frac{2k\left(\omega_{\mathrm{c}}-\omega\right)}{k^2+\frac{\omega_{\mathrm{p}}^2}{c^2}}\frac{\partial B_{\mathrm{w}}}{\partial z}&=-\frac{\mu_0}{2}J_{\mathrm{E}}\frac{2k\left(\omega_{\mathrm{c}}-\omega\right)}{k^2+\frac{\omega_{\mathrm{p}}^2}{c^2}}\\
\frac{\partial B_{\mathrm{w}}}{\partial t}+v_{\mathrm{g}}\frac{\partial B_{\mathrm{w}}}{\partial z}&=-\frac{\mu_0}{2}J_{\mathrm{E}}v_{\mathrm{g}}
\end{aligned}
\tag{A.14}
$$

where $J_{\mathrm{E}}=-J_{\mathrm{R}}\sin\psi$ is the component of the resonant current in the direction of the wave electric field, and v_{g} is the wave group velocity. Returning to Equation (A.12)

and taking the imaginary part,

$$\begin{aligned}
&B_{\mathrm{w}}\Bigg[-\left(k+\frac{\partial\phi}{\partial z}\right)^2\left(\omega_{\mathrm{c}}-\omega+\frac{\partial\phi}{\partial t}\right)-\frac{\omega_{\mathrm{p}}^2}{c^2}\left(-\omega+\frac{\partial\phi}{\partial t}\right)-\frac{\partial^3\phi}{\partial t\partial z^2}\Bigg]\\
&\quad+2\left(k+\frac{\partial\phi}{\partial z}\right)\frac{\partial^2 B_{\mathrm{w}}}{\partial t\partial z}+\left(\omega_{\mathrm{c}}-\omega+\frac{\partial\phi}{\partial t}\right)\frac{\partial^2 B_{\mathrm{w}}}{\partial z^2}\\
&\quad=\mu_0 J_{\mathrm{R}}\Bigg\{\cos\psi\left[\left(\omega_{\mathrm{c}}-\omega+\frac{\partial\phi}{\partial t}+\frac{\partial\psi}{\partial t}\right)\left(k+\frac{\partial\phi}{\partial z}+\frac{\partial\psi}{\partial z}\right)-\frac{1}{J_{\mathrm{R}}}\frac{\partial^2 J_{\mathrm{R}}}{\partial t\partial z}\right]\\
&\qquad+\sin\psi\Bigg[\left(\frac{\partial^2\phi}{\partial t\partial z}+\frac{\partial^2\psi}{\partial t\partial z}\right)+\frac{1}{J_{\mathrm{R}}}\frac{\partial J_{\mathrm{R}}}{\partial t}\left(k+\frac{\partial\phi}{\partial z}+\frac{\partial\psi}{\partial z}\right)\\
&\qquad\quad+\frac{1}{J_{\mathrm{R}}}\frac{\partial J_{\mathrm{R}}}{\partial z}\left(\omega_{\mathrm{c}}-\omega+\frac{\partial\phi}{\partial t}+\frac{\partial\psi}{\partial t}\right)\Bigg]\Bigg\}
\end{aligned}\tag{A.15}$$

expanding the first term,

$$\begin{aligned}
&B_{\mathrm{w}}\Bigg[\left(k^2+\frac{\omega_{\mathrm{p}}^2}{c^2}\right)\omega-\left(k^2+\frac{\omega_{\mathrm{p}}^2}{c^2}\right)\frac{\partial\phi}{\partial t}-k^2\omega_{\mathrm{c}}-2k\left(\omega_{\mathrm{c}}-\omega\right)\frac{\partial\phi}{\partial z}\\
&\qquad-2k\frac{\partial\phi}{\partial z}\frac{\partial\phi}{\partial t}-\left(\frac{\partial\phi}{\partial z}\right)^2\left(\omega_{\mathrm{c}}-\omega+\frac{\partial\phi}{\partial t}\right)-\frac{\partial^3\phi}{\partial t\partial z^2}\Bigg]\\
&\quad+2\left(k+\frac{\partial\phi}{\partial z}\right)\frac{\partial^2 B_{\mathrm{w}}}{\partial t\partial z}+\left(\omega_{\mathrm{c}}-\omega+\frac{\partial\phi}{\partial t}\right)\frac{\partial^2 B_{\mathrm{w}}}{\partial z^2}\\
&\quad=\mu_0 J_{\mathrm{R}}\Bigg\{\cos\psi\left[\left(\omega_{\mathrm{c}}-\omega+\frac{\partial\phi}{\partial t}+\frac{\partial\psi}{\partial t}\right)\left(k+\frac{\partial\phi}{\partial z}+\frac{\partial\psi}{\partial z}\right)-\frac{1}{J_{\mathrm{R}}}\frac{\partial^2 J_{\mathrm{R}}}{\partial t\partial z}\right]\\
&\qquad+\sin\psi\Bigg[\left(\frac{\partial^2\phi}{\partial t\partial z}+\frac{\partial^2\psi}{\partial t\partial z}\right)+\frac{1}{J_{\mathrm{R}}}\frac{\partial J_{\mathrm{R}}}{\partial t}\left(k+\frac{\partial\phi}{\partial z}+\frac{\partial\psi}{\partial z}\right)\\
&\qquad\quad+\frac{1}{J_{\mathrm{R}}}\frac{\partial J_{\mathrm{R}}}{\partial z}\left(\omega_{\mathrm{c}}-\omega+\frac{\partial\phi}{\partial t}+\frac{\partial\psi}{\partial t}\right)\Bigg]\Bigg\}
\end{aligned}\tag{A.16}$$

and applying the "monochromatic" assumption

$$\begin{aligned}
\omega-\frac{\partial\phi}{\partial t}-k\frac{k\omega_{\mathrm{c}}}{k^2+\frac{\omega_{\mathrm{p}}^2}{c^2}}-\frac{2k\left(\omega_{\mathrm{c}}-\omega\right)}{k^2+\frac{\omega_{\mathrm{p}}^2}{c^2}}\frac{\partial\phi}{\partial z}&=\frac{\mu_0}{2}\frac{J_{\mathrm{R}}\cos\psi}{B_{\mathrm{w}}}\frac{2k\left(\omega_{\mathrm{c}}-\omega\right)}{k^2+\frac{\omega_{\mathrm{p}}^2}{c^2}}\\
\omega-kv_{\mathrm{p}}-\frac{\partial\phi}{\partial t}-v_{\mathrm{g}}\frac{\partial\phi}{\partial z}&=\frac{\mu_0}{2}\frac{J_{\mathrm{R}}\cos\psi}{B_{\mathrm{w}}}v_{\mathrm{g}}\\
\frac{\partial\phi}{\partial t}+v_{\mathrm{g}}\frac{\partial\phi}{\partial z}&=-\frac{\mu_0}{2}\frac{J_{\mathrm{B}}}{B_{\mathrm{w}}}v_{\mathrm{g}}
\end{aligned}\tag{A.17}$$

where $J_{\mathrm{B}} = J_{\mathrm{R}} \cos\psi$ is the component of the resonant current in the direction of the wave magnetic field, and $v_{\mathrm{p}} = \omega/k$ is the wave phase velocity. Together, Equation (A.14) and Equation (A.17) describe the influence of a resonant current on the evolution of a parallel propagating, monochromatic, whistler mode wave.

Bibliography

Andrews, M. K., F. B. Knox, and T. N. R. (1978), Magnetopsheric electric fields and protonospheric coupling fluxes inferred from simultaneous phase and group path measurements on whistler mode signals, *Planet. Space Sci.*, *26*, 171–183.

Angerami, J. J. (1970), Whistler duct properties deduced from VLF observations made with the OGO 3 satellite near the magnetic equator, *J. Geophys. Res.*, *75*, 6115.

Angerami, J. J., and J. O. Thomas (1964), Studies of planetary atmospheres, *J. Geophys. Res.*, *69*, 4537–4560.

Bailey, V. A., and D. F. Martyn (1934), Interaction of radio waves, *Nature*, *133*, 218.

Barr, R., and P. Stubbe (1991), ELF radiation from the Tromsø "super heater" facility, *Geophys. Res. Lett.*, *18*, 1035–1038.

Barr, R., M. T. Rietveld, H. Kopka, P. Stubbe, and E. Nielsen (1985), Extra-low-frequency radiation from the polar electrojet antenna, *Nature*, *317*, 155–157.

Baumjohann, W. (1983), Ionospheric and field-aligned current systems in the auroral zone: a concise review, *Adv. Space. Res.*, *10*, 55–62.

Bell, T. F., and U. S. Inan (1981), Transient nonlinear pitch angle scattering of energetic electrons by coherent VLF wave packets in the magnetosphere, *J. Geophys. Res.*, *86*, 9047.

Bell, T. F., and H. D. Ngo (1988), Electrostatic waves simulated by coherent VLF signals propagating in and near the inner radiation belt, *J. Geophys. Res.*, *93*, 2599–2618.

Bell, T. F., and H. D. Ngo (1990), Electrostatic lower hybrid waves excited by electromagnetic whistler mode waves scattering from planar magnetic-field-aligned plasma density irregularities, *J. Geophys. Res.*, *95*, 149–172.

Bell, T. F., U. S. Inan, I. Kimura, H. Matsumoto, T. Mukai, and K. Hashimoto (1983), EXOS-B/Siple Station VLF wave-particle interaction experiments: 2. Transmitter signals and associated emissions, *J. Geophys. Res.*, *88*, 295.

Bell, T. F., U. S. Inan, M. T. Danielson, and S. A. Cummer (1995), VLF signatures of ionospheric heating by HIPAS, *Radio. Sci.*, *30*, 1855–1867.

Bell, T. F., U. S. Inan, R. A. Helliwell, and J. D. Scudder (2000), Simultaneous triggered VLF emissions and energetic electron distributions observed on POLAR with PWI and HYDRA, *Geophys. Res. Lett.*, *27*, 165.

Bell, T. F., U. S. Inan, J. Bortnik, and J. D. Scudder (2002), The Landau damping of magnetospherically reflected whistlers within the plasmasphere, *Geophys. Res. Lett.*, *29*, 1733.

Bortnik, J., U. S. Inan, and T. F. Bell (2006), Temporal signatures of radiation belt electron precipitation induced by lightning-generated MR whistler waves: 1. Methodology, *J. Geophys. Res.*, *111*, A02,204.

Budden, K. G. (1988), *The Propagation of Radio Waves: The Theory of Radio Waves of Low Power in the Ionosphere and Magnetosphere*, Cambridge University Press.

Calvert, W., and J. M. Warnock (1969), Ionospheric irregularities observed by topside sounders, *Proc. IEEE*, *57*, 1019.

Carlson, C. R., R. A. Helliwell, and U. S. Inan (1990), Space-time evolution of whistler mode wave growth in the magnetosphere, *J. Geophys. Res.*, *95*, 15,073.

Carpenter, D. L. (1963), Whistler evidence of a 'knee' in the magnetospheric ionization density profile, *J. Geophys. Res.*, *68*, 1675.

Carpenter, D. L., and R. R. Anderson (1992), An ISEE/Whistler model of equatorial electron density in the magnetosphere, *J. Geophys. Res.*, *97*, 1097.

Carpenter, D. L., and Z. T. Bao (1983), Occurence properties of ducted whistler-mode signals from the new VLF transmitter at Siple Station, Antarctica, *J. Geophys. Res.*, *88*, 7051.

Carpenter, D. L., and T. R. Miller (1976), Ducted magnetospheric propagation of signals from the Siple, Antarctica VLF transmitter, *J. Geophys. Res.*, *81*, 2692.

Carpenter, D. L., and T. R. Miller (1983), Rare ground-based observations of Siple VLF transmitter signals outside the plasmapause, *J. Geophys. Res.*, *88*, 10,227.

Carpenter, D. L., and D. M. Šulić (1988), Ducted whistler propagation outside the plasmapause, *J. Geophys. Res.*, *A9*, 9731–9742.

Carpenter, D. L., M. Galand, T. F. Bell, V. S. Sonwalkar, U. S. Inan, J. LaBelle, A. J. Smith, T. D. G. Clark, and T. J. Rosenberg (1997), Quasiperiodic 560 s fluctuations of VLF signals propagating in the Earth-ionosphere waveguide: A result of pulsating auroral particle precipitation?, *J. Geophys. Res.*, *102*, 347–361.

Clark, D. H., and W. J. Raitt (1976), The global morphology of irregularities in the top-side ionopshere as measured by the total ion current probe on ESRO-4, *Planet. Space Sci.*, *24*, 873.

Cohen, M. B., , U. S. Inan, and M. A. Golkowski (2008a), Geometric modulation: A more effective method of steerable ELF/VLF wave generation with continuous HF heating of the lower ionosphere, *Geophys. Res. Lett.*, *35*, L12,101.

Cohen, M. B., M. Gołkowski, and U. S. Inan (2008b), Orientation of the HAARP ELF ionospheric dipole and the auroral electrojet, *Geophys. Res. Lett.*, *35*, L02,806.

Cohen, M. B., U. S. Inan, and E. Paschal (2009), Sensitive broadband ELF/VLF reception with the AWESOME instrument, *IEEE Trans. Geos. Rem. Sens.*, *TBD*, (manuscript in preparation).

Dingle, B., and D. L. Carpenter (1981), Electron precipitation induced by VLF noise bursts at the plasmapause and detected at conjugate ground stations, *J. Geophys. Res.*, *86*, 4597.

Djuth, F. T., B. W. Reinisch, D. F. Kitrosser, J. H. Elder, A. L. Snyder, and G. S. Sales (2006), Imaging HF-induced large-scale irregularities above HAARP, *Geophys. Res. Lett.*, *33*, L04,107.

Dowden, R. L., A. D. McKay, L. E. S. Amon, H. C. Koons, and M. H. Dazey (1978), Linear and nonlinear amplification in the magnetosphere during a 6.6-kHz transmission, *J. Geophys. Res.*, *83*, 169.

Dyson, P. L. (1969), Direct measurements of the size and amplitude of irregularities in the topside ionosphere, *J. Geophys. Res.*, *74*, 6291.

Dysthe, K. B. (1971), Some studies of triggered whistler emissions, *J. Geophys. Res.*, *76*, 6915.

Ferraro, A. J., H. S. Lee, R. Allshouse, K. Carrol, A. A. Tomko, F. J. Kelly, and R. G. Joiner (1982), VLF/ELF radiation from the ionospheric dynamo current system, modulated by powerful HF signals, *J. Atmos. Terr. Phys.*, *44*, 1113–1122.

Ferraro, A. J., H. S. Lee, R. Allshouse, K. Carrol, R. Lunnen, and T. Collins (1984), Characteristics of ionospheric ELF radiation generated by HF heating, *J. Atmos. Terr. Phys.*, *46*, 855–865.

Forbes, J. M. (1981), The equatorial electrojet, *Rev. of Geophys. Space Phys.*, *19*, 469–504.

Getmantsev, C. G., N. A. Zuikov, D. S. Kotik, N. A. Mironenko, V. O. Mityakov, Y. A. Rapoport, V. Y. Sazanov, V. Y. Trakhtengerts, and V. Y. Eidman (1974),

Combination frequencies in the interaction between high-power short-wave radiation and ionsopheric plasma, *JETP*, *20*, 101–102.

Gibby, A. R. (2008), Saturation effects in VLF triggered emissions, Ph.D. thesis, Stanford University.

Gibby, A. R., U. S. Inan, and T. F. Bell (2008), Saturation effects in the VLF triggered emission process, *J. Geophys. Res.*, *113*, A11,215.

Gołkowski, M., and U. S. Inan (2008), Multistation observations of ELF/VLF whistler mode chorus, *J. Geophys. Res.*, *113*, A08,210.

Gołkowski, M., U. S. Inan, A. R. Gibby, and M. B. Cohen (2008), Magnetospheric amplification and emission triggering by ELF/VLF waves injected by the 3.6 MW HAARP ionospheric heater, *J. Geophys. Res.*, *113*, A10,201, doi:10.1029/2008JA013,157.

Gross, S. H., and D. B. Muldrew (1984), Uniformly spaced field-aligned ionization ducts, *J. Geophys. Res.*, *89*, 8986.

Gurnett, D. A., and A. Bhattacharjee (2005), *Introduction to Plasma Physics*, Cambridge University Press.

Helliwell, R. A. (1965), *Whistlers and Related Ionospheric Phenomena*, Stanford University Press.

Helliwell, R. A. (1970), A new program of magnetospheric research in Antarctica, NSF Proposal, Stanford Proposal No. RL 10-71.

Helliwell, R. A. (1988), VLF wave stimulation experiments in the magnetosphere from Siple Station, Antarctica, *Rev. Geophys.*, *26*, 551.

Helliwell, R. A., and T. L. Crystal (1973), A feedback model of cyclotron interaction between whistler-mode waves and energetic electrons in the magnetosphere, *J. Geophys. Res.*, *78*, 7357.

Helliwell, R. A., and J. P. Katsufrakis (1974), VLF wave injection into the magnetosphere from Siple Station, Antarctica, *J. Geophys. Res.*, *79*, 2511.

Helliwell, R. A., and J. P. Katsufrakis (1978), Controlled wave-particle interaction experiments, in *Upper Atmospere Research in Antarctica*, edited by L. J. Lanzerotti and C. G. Park, p. 100, Antarctic Research Service.

Helliwell, R. A., J. P. Katsufrakis, M. Trimpi, and N. Brice (1964), Artificially stimulated very-low-frequency radiation from the ionosphere, *J. Geophys. Res.*, *69*, 2391.

Helliwell, R. A., D. L. Carpenter, and T. R. Miller (1980a), Power threshold for growth of coherent VLF signals in the magnetosphere, *J. Geophys. Res.*, *85*, 3360.

Helliwell, R. A., S. B. Mende, J. H. Doolittle, W. C. Armstrong, and D. L. Carpenter (1980b), Correlations between (lambda)4278 optical emissions and VLF wave events observed at L$\sim$4 in the Antarctic, *J. Geophys. Res.*, *85*, 3376–3386.

Hui, C. H., and C. E. Seyler (1992), Electron acceleration by Alfven waves in the magnetosphere, *J. Geophys. Res.*, *97*, 3953–3963.

Imhof, W. L., J. B. Reagan, H. D. Voss, E. E. Gaines, D. W. Datlowe, J. Mobilia, R. A. Helliwell, U. S. Inan, and J. P. Katsufrakis (1983a), Direct observation of radiation belt electron precipitation by the controlled injection of VLF signals from a ground-based transmitter, *Geophys. Res. Lett.*, *10*, 361.

Imhof, W. L., J. B. Reagan, H. D. Voss, E. E. Gaines, D. W. Datlowe, J. Mobilia, R. A. Helliwell, U. S. Inan, and J. P. Katsufrakis (1983b), The modulated precipitation of radiation belt electrons by controlled signals from VLF transmitters, *Geophys. Res. Lett.*, *10*, 615.

Inan, U. S. (1977), Non-linear gyroresonant interactions of energetic particles and coherent VLF waves in the magnetosphere, Ph.D. thesis, Stanford University.

Inan, U. S. (1990), VLF heating of the lower ionosphere, *Geophys. Res. Lett.*, *17*, 729–732.

Inan, U. S., and T. F. Bell (1977), The plasmapause as a VLF wave guide, *J. Geophys. Res.*, *82*, 28192827.

Inan, U. S., and A. S. Inan (2000), *Electromagnetic Waves*, Prentice Hall.

Inan, U. S., T. F. Bell, J. Bortnik, and J. M. Albert (2003), Controlled precipitation of radiation belt electrons, *J. Geophys. Res.*, *108*, 1186.

Inan, U. S., D. Piddyachiy, W. B. Peter, J. A. Sauvaud, and M. Parrot (2007a), DEMETER satellite observations of lightning-induced electron precipitation, *Geophys. Res. Lett.*, *34*, L02,103.

Inan, U. S., et al. (2004), Multi-hop whistler-mode ELF/VLF signals and triggered emissions excited by the HAARP HF heater, *Geophys. Res. Lett.*, *31*, L24,805.

Inan, U. S., et al. (2007b), Subionospheric VLF observations of transmitter-induced precipitation of inner radiation belt electrons, *Geophys. Res. Lett.*, *34*, L02,106.

James, H., R. L. Dowden, M. T. Rietveld, P. Stubbe, and H. Kopka (1984), Simultaneous observations of ELF waves from an artificially modulated auroral electrojet in space and on the ground, *J. Geophys. Res.*, *89*, 1655–1666.

James, H., U. S. Inan, and M. T. Rietveld (1990), Observations on the DE-1 spacecraft of ELF/VLF waves generated by an ionospheric heater, *J. Geophys. Res.*, *95*, 12,187–12,195.

Karpman, V. I., and D. R. Shklyar (1972), Non-linear damping of potential monochromatic waves in an inhomogeneous plasma, *Soviet Phys. JETP*, *35*, 500.

Kennel, C. F., and H. E. Petschek (1966), Limit on stably trapped particle fluxes, *J. Geophys. Res.*, *71*, 1.

Kimura, I., A. Wong, B. Chouinard, M. McCarrick, and T. Okada (1991), Satellite and ground observations of HIPAS VLF modulation, *Geophys. Res. Lett.*, *18*, 309–312.

Lehtinen, N. G., and U. S. Inan (2008), Radiation of ELF/VLF waves by harmonically varying currents into a stratified ionosphere with application to radiation by a modulated electrojet, *J. Geophys. Res.*, *113*, A06,301, doi:10.1029/2007JA012,911.

Lyons, L. R., and R. M. Thorne (1970), The magnetospheric reflection of whistlers, *Planet. Space Sci.*, *18*, 1753.

Lyons, L. R., R. M. Thorne, and C. K. Kennel (1972), Pitch angle diffusion of radiation belt electrons within the plasmasphere, *J. Geophys. Res.*, *77*, 3455.

Matsumoto, H., and I. Kimura (1971), Linear and nonlinear instabilities and VLF emissions in the magnetosphere, *Planet. Sp. Sci.*, *19*, 567.

Milikh, G. M., K. Papadopoulos, M. McCarrick, and J. Preston (1999), ELF emission generated by the HAARP HF-heater using varying frequency and polarization, *Izvestiya Vysshikh Uchebnykh Zavedenii, Radiofizika*, *42*, 728–735.

Moore, R. C. (2007), ELF/VLF wave generation by modulated HF heating of the auroral electrojet, Ph.D. thesis, Stanford University.

Moore, R. C., U. S. Inan, T. F. Bell, and E. J. Kennedy (2007), ELF waves generated by modulated HF heating of the auroral electrojet and observed at a ground distance of $\sim$ 4400 km, *J. Geophys. Res.*, *112*, A05,309.

Nunn, D. (1974), A self-consistent theory of triggered VLF emissions, *Planet. Sp. Sci.*, *22*, 349.

Nunn, D. (1990), The numerical simulation of VLF nonlinear wave-particle interactions in collision-free plasmas using the Vlasov Hybrid Simulation technique, *Comp. Phys. Comm.*, *60*, 1.

Nunn, D. (1993), A novel technique for the numerical simulation of hot collision-free plasma; Vlasov Hybrid Simulation, *J. Comp. Phys.*, *108*, 180.

Nunn, D., Y. Omura, H. Matsumoto, I. Nagano, and S. Yagitani (1997), The numerical simulation of VLF chorus and discrete emissions observed on the Geotail satellite using a Vlasov code, *J. Geophys. Res.*, *102*, 27,083.

Nunn, D., A. G. Demenkov, V. Y. Trakhtengerts, and M. J. Rycroft (2003), VLF emission triggering by a highly anisotropic energetic electron plasma, *Ann. Geophys.*, *21*, 481.

Nunn, D., M. J. Rycroft, and V. Y. Trakhtengerts (2005), A parametric study of the numerical simulations of triggered VLF emissions, *Ann. Geophys.*, *23*, 1.

O'Brien, T. P., K. R. Lorentzen, I. R. Mann, N. P. Meredith, J. B. Blake, J. F. Fennell, M. D. Looper, D. K. Milling, and R. R. Anderson (2003), Energization of relativistic electrons in the presence of ULF power and MeV microbursts: evidence for dual ULF and VLF acceleration, *J. Geophys. Res.*, *108*, 1329.

Omura, Y., and H. Matsumoto (1982), Computer simulations of basic processes of coherent whistler mode wave-particle interactions in the magnetosphere, *J. Geophys. Res.*, *87*, 4435.

Omura, Y., and D. Summers (2006), Dynamics of high-energy electrons interacting with whistler mode chorus emissions in the magnetosphere, *J. Geophys. Res.*, *111*, A09,222.

Omura, Y., D. Nunn, H. Matsumoto, and M. J. Rycroft (1991), A review of observational, theoretical and numerical studies of VLF triggered emissions, *J. Atmos. Terr. Phys.*, *53*, 351.

Omura, Y., Y. Katoh, and D. Summers (2008), Theory and simulation of the generation of whistler-mode chorus, *J. Geophys. Res.*, *113*, A04,223, doi:10.1029/2007JA012,622.

Park, C. G. (1972), Methods of determining electron concentrations in the magnetosphere from nose whistlers, Stanford Electronics Laboratories Technical Report No. 3454-1.

Parrot, M. (2006), Special issue: First results of the DEMETER micro-satellite, *Planet. Space. Sci.*, *54*, 411–558.

Paschal, E. W., and R. A. Helliwell (1984), Phase measurement of whistler mode signals from the Siple VLF transmitter, *J. Geophys. Res.*, *89*, 1667.

Pasko, V. P., and U. S. Inan (1994), Recovery signatures of lightning-associated VLF perturbations as a measure of the lower ionosphere, *J. Geophys. Res.*, *99*, 17,523–17,537.

Peter, W. B., and U. S. Inan (2007), A quantitative comparison of lightning-induced electron precipitation and VLF signal perturbations, *J. Geophys. Res.*, *112*, A12,212.

Piddyachiy, D., U. S. Inan, and T. F. Bell (2008), DEMETER observations of ELF signals generated by the HAARP HF heater, *Geophys. Res. Lett.*, *113*, A10,308, doi:10.1029/2008JA013,208.

Platino, M., U. S. Inan, T. F. Bell, J. S. Pickett, E. J. Kennedy, J. G. Trotignon, J. L. Rauch, and P. Canu (2004), Cluster observations of ELF/VLF signals generated by modulated heating of the lower ionosphere with the HAARP HF transmitter, *Ann. Geophys.*, *22*, 2643.

Platino, M., U. S. Inan, T. F. Bell, M. Parrot, and E. J. Kennedy (2006), DEMETER observations of ELF waves injected with the HAARP HF transmitter, *Geophys. Res. Lett.*, *33*, L16,101.

Raghuram, R., R. L. Smith, and T. F. Bell (1974), VLF Antarctic antenna: impedance and efficiency, *IEEE Trans. on Ant. and Prop.*, *AP-22*, 334.

Ratcliffe, J. A. (1959), *The Magneto-ionoc Theory and its Applications*, Stanford University Press.

Rietveld, M. T., H. Kopka, E. Nielsen, P. Stubbe, and R. L. Dowden (1983), Ionospheric electric pulsations: A comparison between VLF results from an ionospheric heating experiment and STARE, *J. Geophys. Res.*, *88*, 2140–2146.

Rietveld, M. T., H.-P. Mauelshagen, P. Stubbe, H. Kopka, and E. Nielsen (1987), The characteristics of ionospheric heating-produced ELF/VLF waves over 32 hours, *J. Geophys. Res.*, *92*, 8707–8722.

Rosenberg, T. J. (1981), Balloon measurements from Siple Station during the 1980-1981 magnetospheric physics campaign, *Antarctic J.*, *XVI*, 204.

Rosenberg, T. J., J. C. Siren, D. L. Mathews, K. Marthinsen, J. A. Holtet, A. Egeland, D. L. Carpenter, and R. A. Helliwell (1981), Conjugacy of electron microbursts and VLF chorus, *J. Geophys. Res.*, *86*, 5819–5832.

Roux, A., and R. Pellat (1978), A theory of triggered emissions, *J. Geophys. Res.*, *83*, 1433.

Rycroft, M. J., S. Israelsson, and C. Price (2000), The global atmospheric electric circuit, solar activity and climate change, *J. Atmos. Terr. Phys.*, *62*, 1563–1576.

Sazhin, S. S., H. Hayakawa, and K. Bullough (1992), Whistler diagnostics of magnetospheric parameters: a review, *Ann. Geophys.*, *10*, 293.

Sonwalkar, V. S., and J. Harikumar (2000), An explanation of ground observations of auroral hiss: role of density depletions and meter-scale irregularities, *J. Geophys. Res.*, *105*, 18,867–18,883.

Stiles, G. S., and R. A. Helliwell (1975), Frequency-time behavior of artificially stimulated VLF emissions, *J. Geophys. Res.*, *80*, 608.

Storey, L. R. O. (1953), An investigation of whistling atmospherics, *Phil. Trans. of the Roy. Soc. of London*, *246*, 113–141.

Strangeways, H. J., M. J. Rycroft, and M. J. Jarvis (1982), Multi-station VLF direction-finding measurements in eastern Canada, *J. Atmos. Terr. Res.*, *44*, 509–522.

Streltsov, A. V. (2007), Spectral properties of high-density ducts, *J. Geophys. Res.*, *112*, A12,218, doi:10.1029/2007JA012,710.

Streltsov, A. V., M. Lampe, W. Manheimer, G. Ganguli, and G. Joyce (2006), Whistler propagation in inhomogeneous plasma, *J. Geophys. Res.*, *111*, A03,216, doi:10.1029/2005JA011,357.

Stubbe, P. H., H. Kopka, and R. L. Dowden (1977), Generation of ELF and VLF waves by polar electrojet modulation: Experimental results, *J. Geophys. Res.*, *86*, 9073–9078.

Stubbe, P. H., H. Kopka, , M. T. Rietveld, and R. L. Dowden (1982), ELF and VLF generation by modulated heating of the current carrying ionosphere, *J. Atmos. Terr. Phys.*, *44*, 1123–1135.

Tascione, T. F. (1994), *Introduction to the Space Environment*, Krieger Publishing Company.

Villaseñor, J., A. Y. Wong, B. Song, J. Pau, M. McCarrick, and D. Sentman (1996), Comparison of ELF/VLF generation modes in the ionosphere by the HIPAS heater array, *Radio Sci.*, *31*, 211–226.

Walt, M. (1994), *Introduction to Geomagnetically Trapped Radiation*, Cambridge University Press.